

https://dspace.org/

One-dimensional compression behaviour of non-plastic soils

Owolabi, AbideenToba

2018
https://hdl.handle.net/10539/26761

Downloaded from a DSpace repository. https://dspace.org/

ONE-DIMENSIONAL COMPRESSION BEHAVIOUR OF NON-PLASTIC SOILS

Abideen Toba Owolabi

A dissertation submitted to the Faculty of Engineering and the Built Environment, University of the Witwatersrand, Johannesburg, in fulfilment of the requirements for the degree of Master of Science in Engineering.

Supervisor: Dr Luis Alberto Torres Cruz

Co-supervisor: Dr Nico Vermeulen

Examiners: Dr Irvin Luker and Prof Peter Day

Johannesburg, 2018

Candidate Declaration

I declare that this dissertation is my own unaided work. It is being submitted to the Degree of Master of science to the University of the Witwatersrand, Johannesburg. It has not been submitted before for any degree or examination to any other University.

……..

(Signature of the Candidate)

……day of …… year ……

Abstract

The one-dimensional (1-D) compression behaviour of sands at stress levels that are high enough to induce significant particle breakage can be represented by a limiting compression curve (LCC) in the compression plane, i.e. void ratio (e) versus vertical effective stress (σ'_v). Results from previous studies have shown that the LCC reflects the combined effects of particle size distribution (PSD), particle shape, and mineralogy. Additionally, previous studies have reported that the mean particle size (D_{50}) also has an effect on the LCC. The current study focused on the effect that the broadness of the PSD and particle shape have on the LCC. To achieve this, variations in mineralogy were reduced by considering only quartzitic sands, and the PSDs had varying broadness but a constant D_{50}. Eleven soil types were tested, with particle shapes that varied from commercially manufactured spherical beads to angular filter sand. The results confirm the findings from previous studies regarding the way in which PSD and particle shape affect the LCC. Correlations are presented which allow for initial assessments of the LCC of quartzitic sands based on particle shape, PSD, and limit void ratios. The results also show that, when the LCC is modelled in a doubly logarithmic compression plane, there is a well-defined direct and linear correlation between its slope (ρ_c) and the reference vertical effective stress at a unit void ratio (σ'_r). Further testing is recommended to determine whether this correlation is affected by variations in D_{50}.

Dedication

To the geotechnical engineering community

Acknowledgements

All adoration and glorification is due to Almighty God, the Lord of the universe. I thank Him for keeping me healthy and giving me sound mind throughout the course of this program.

I am grateful to my supervisors in respect of Dr Luis Alberto Torres-Cruz and Dr Nico Vermeulen for their patient guidance at every stage of this study, from beginning to the end. I am also grateful for the assistance of Dr Mike Otieno, Dr Charles Macrobert, Mrs Tumelo Lamola, Mr Edward Pretorius, Mr Samuel Mabote, Mr Jason Mader and Miss Mamonaheng Rapapa.

Finally, my earnest appreciation goes to my family and friends for their unending support in every capacity. To them, I am highly indebted and words alone cannot describe my gratitude. May God continue to be with you in all your endeavours.

Table of Contents

List of Figures ix

List of Tables xiv

List of Symbols xv

1 GENERAL INTRODUCTION 1

1.1 Background and Motivation 1

1.2 Research Objective and Dissertation Outline 4

1.3 Figure 5

2 LITERATURE REVIEW 6

2.1 Introduction 6

2.2 The Limiting Compression Curve (LCC) Concept 6

2.3 1-D Confined Compression Test Loading Methods and Equipment 8

2.4 Representation of the LCC 10

2.5 Factors Affecting the LCC 11

2.5.1 Effect of PSD on the LCC 11

2.5.2 Effect of particle shape on the LCC 12

2.5.3 Effect of mineralogy on the LCC 13

2.6 Concluding remarks 13

2.7 Figures and Tables 15

3 METHODS AND MATERIALS 21

3.1 Introduction 21

3.2 1-D Confined Compression Testing Equipment 21

3.3 Justification for the Selected Loading Method 23

3.4 Selected Soil Types 24

3.5 Correlations amongst Index Properties 25

3.6 Sample Preparation and Experimental Procedure 26

3.7 Experimental Data Presentation, Processing and Calculations 29

3.7.1 Void ratio calculation 29

3.7.2 1-D confined compression data processing and presentation 30

3.7.3 Particle crushing measurement 32

3.8 Summary 32

3.9 Figures and Tables 33

4 EXPERIMENTAL RESULTS 45

4.1 Introduction 45

4.2 1-D Confined Compression Curves 45

4.3 The Limiting Compression Curves 47

4.3.1 Relationship between the LCC and compressibility 49

4.4 Particle Crushing 50

4.5 Compression Mould Lateral Deformations 51

4.6 Figures and Tables 51

5 CORRELATION BETWEEN THE LCC PARAMETERS AND PSD, PARTICLE SHAPE AND LIMIT VOID RATIOS 74

5.1 Introduction 74

5.2 Correlation between the LCC parameters and PSD 74

5.3 Correlation between the LCC parameters and Particle shape 75

5.4 Correlation between the LCC parameters and the e_{max} and e_{min} 76

5.5 Figures 76

6 CONCLUSION AND RECOMMENDATIONS 80

6.1 Conclusion 80

6.2 Recommendations for Future studies 81

7 REFERENCES 83

8 APPENDICES 88

8.1 Appendix A 1-D Compression Curves 88

8.2 Appendix B LCC Determination Plots 92

8.3 Appendix C Post-compression Sieve Analysis Results 96

List of Figures

Fig. 1.1 Conceptual representation of the LCC [adopted from Uygar and Doven (2006)]. 5

Fig. 2.1 PSD curves of the sands investigated by Hendron (1963)……15

Fig. 2.2 Conceptual representation of the LCC for cohesionless soils (Pestana and Whittle, 1995)..... 15

Fig. 2.3 Normal compression curve of silica sand in e-log$\sigma'v$ space (McDowell, 2005) as adopted from McDowell (2002). 16

Fig. 2.4 A replot of Figure 2.3 in log$e$-log$\sigma'v$ space (McDowell, 2005)..... 16

Fig. 2.5 PSD curves of Dog's bay sand. From narrowest to broadest gradation; D1,D2, D3 and D4, and CD (critical grading) (Altuhafi and Coop, 2011)..... 16

Fig. 2.6 1-D compression curves of Dog's bay sand. From narrowest to broadest gradation; D1, D2, D3 and D4 (Altuhafi and Coop, 2011). 17

Fig. 2.7 A plot of median particle size against reference vertical effective stress; UOS, uniform Ottawa sand; GQ, ground quartz [tested by Roberts and De Souza (1958) and Roberts (1964)]. 17

Fig. 2.8 1-D confined compression tests results of Cavarretta et al. (2010). 'As supplied' refers to the spherical glass ballotine particles. 18

Fig. 3.1 Compression mould placed in the compression machine and with the three displacement transducers in place…….33

Fig. 3.2 1-D confined compression testing equipment data acquisition system... 34

Fig. 3.3 Schematic diagram of the compression mould vessel (all dimensions are in mm). 34

Fig. 3.4 PSD curves of the samples used for preliminary study. 35

Fig. 3.5 Compression curves of the samples used for preliminary study; DL; discrete loading compression machine; CL; continuous loading compression machine; UG, uniformly graded PSD; WG, widely graded PSD. 35

Fig. 3.6 Continuous rate of stress loading compression machine. 36

Fig. 3.7 Discrete loading compression machine. 37

Fig. 3.8 PSD curves of the soil types tested. 37

Fig. 3.9 Microscope images showing the particle shape of the four different sources of granular materials tested. 38

Fig. 3.10 Krumbein and Sloss (1963) Particle shape determination chart. 38

Fig. 3.11 Relation between e_{max} and e_{min} of the selected soil types. 39

Fig. 3.12 Relationship between e_{max} and PSD. 39

Fig. 3.13 Relationship between e_{min} and PSD. 39

Fig. 3.14 Relationship between e_{max} and particle roundness. 40

Fig. 3.15 Relationship between e_{min} and particle roundness. 40

Fig. 3.16 Compression mould lateral expansion measured from two horizontal LVDTs. 40

Fig. 3.17 Telescopic gauge used to measure the final height of the specimens, H_f. 41

Fig. 3.18 Illustration of the approach used in defining the 1-D compression curve obtained herein; (a) initial data points (b) refined 35 data points. 42

Fig. 3.19 LCC determination for the angular, broad PSD soil type. 43

Fig. 3.20 Hardin (1985) particle breakage measurement parameters. 43

Fig. 4.1 Typical 1-D confined compression curves of the tested soil types in: (a) semi-logarithmic space; (b) double-logarithmic space; (c) natural space……..52

Fig. 4.2 AI soil type 1-D compression curves. 53

Fig. 4.3 SI soil type 1-D compression curves. 53

Fig. 4.4 RI soil type 1-D compression curves. 54

Fig. 4.5 BI soil type 1-D compression curves. 54

Fig. 4.6 Effect of initial relative density on compressibility for the AI soil type. 55

Fig. 4.7 Effect of initial relative density on compressibility for the SI soil type.. 55

Fig. 4.8 Effect of initial relative density on compressibility for the RI soil type. 56

Fig. 4.9 Effect of initial relative density on compressibility for the BI soil type. 56

Fig. 4.10 Effect of PSD on compressibility for the angular soil types. 57

Fig. 4.11 Effect of PSD on compressibility for the sub-angular soil types..... 58

Fig. 4.12 Effect of PSD on compressibility for the rounded soil types. 59

Fig. 4.13 Effect of PSD on compressibility for the beads soil types. 60

Fig. 4.14 Effect of particle shapes on compressibility. 61

Fig. 4.15 LCC determination for the AI soil type. 62

Fig. 4.16 LCC determination for the SI soil type..... 62

Fig. 4.17 LCC determination for the RI soil type. 63

Fig. 4.18 LCC determination for the BI soil type. 63

Fig. 4.19 Limiting compression curves of the angular soil types. 64

Fig. 4.20 Limiting compression curves of the sub-angular soil types. 64

Fig. 4.21 Limiting compression curves of the rounded soil types. 65

Fig. 4.22 Limiting compression curves of the beads soil types. 65

Fig. 4.23 Relationship between the LCC parameters..... 66

Fig. 4.24 Relationship between the LCC and compressibility. 66

Fig. 4.25 Pre and post-compression PSD curves of the AI soil type. 67

Fig. 4.26 Pre and post-compression PSD curves of the SI soil type. 67

Fig. 4.27 Pre and post-compression PSD curves of the RI soil type. 68

Fig. 4.28 Pre and post-compression PSD curves of the BI soil type. 68

Fig. 4.29 Effect of PSD on particle breakage. 69

Fig. 4.30 Effect of particles roundness on particle breakage. 69

Fig. 5.1 Relationship between ρc and C_u……...76

Fig. 5.2 Relationship between σ′r and C_u. 77

Fig. 5.3 Relationship between ρc and particle roundness. 77

Fig. 5.4 Relationship between σ′r and particle roundness. 77

Fig. 5.5 Relationship between ρc and emax. 78

Fig. 5.6 Relationship between ρc and emin..... 78

Fig. 5.7 Relationship between σ′r and emax. 78

Fig. 5.8 Relationship between σ′r and emin..... 79

Fig. A.1 Angular broad soil type 1-D compression curves……88

Fig. A.2 Angular narrow soil type 1-D compression curves. 88

Fig. A.3 Sub-angular broad soil type 1-D compression curves. 89

Fig. A.4 Sub-angular narrow soil type 1-D compression curves. 89

Fig. A.5 Rounded narrow soil type 1-D compression curves. 90

Fig. A.6 Beads broad soil type 1-D compression curves. 90

Fig. A.7 Beads narrow soil type 1-D compression curves. 91

Fig. B.1 LCC determination for the AB soil type……..92

Fig. B.2 LCC determination for the AN soil type. 92

Fig. B.3 LCC determination for the SB soil type. 93

Fig. B.4 LCC determination for the SN soil type. 93

Fig. B.5 LCC determination for the RN soil type. 94

Fig. B.6 LCC determination for the BB soil type. 94

Fig. B.7 LCC determination for the BN soil type. 95

Fig. C.1 Pre and post-compression PSD curves of the AB soil type.……96

Fig. C.2 Pre and post-compression PSD curves of the AN soil type. 96

Fig. C.3 Pre and post-compression PSD curves of the SB soil type. 97

Fig. C.4 Pre and post-compression PSD curves of the SN soil type. 97

Fig. C.5 Pre and post-compression PSD curves of the RN soil type. 98

Fig. C.6 Pre and post-compression PSD curves of the BB soil type. 98

Fig. C.7 Pre and post-compression PSD curves of the BN soil type. 99

List of Tables

Table 2.1 Moulds description and methods of load application. 19

Table 2.2 Summary of the results of 1-DCC tests performed by Roberts and De Souza (1958) and Roberts (1964) [adopted from Pestana and Whittle (1995)].... 20

Table 3.1 Fundamental index properties of the selected soil types……...44

Table 3.2 XRF major chemical composition analysis results. 44

Table 4.1 1-D confined compression testing program summary……...70

Table 4.2 The LCC and particle breakage characteristics of the tested soil types. 73

List of Symbols

a_v	coefficient of compressibility
B_p	potential breakage
B_r	relative breakage
B_t	total breakage
C_u	uniformity coefficient
D_r	relative density
D_{50}	median particle size (mm)
E	modulus of elasticity
e	void ratio
e_o	void ratio of the LCC at σ'_o
e_{max}	maximum void ratio
e_{min}	minimum void ratio
G_s	specific gravity
H_f	final height of specimen
H_s	equivalent height of specimen
K_o	coefficient of earth pressure
M_s	mass of specimen
NCL	normal compression line
P'	mean normal effective stress
R	particles roundness
S	particles sphericity
v	specific volume
V_s	volume of solids
V_T	total volume
V_v	volume of void
λ	LCC slope in $e - \log\sigma'_v$ space
ρ_c	LCC slope in $\log e - \log\sigma'_v$ space
ρ_w	water density
σ'_o	arbitrary chosen effective stress
σ'_r	reference vertical effective stress at a void ratio of 1.0
σ'_v	vertical effective stress
$\sigma'_{v@LCC}$	vertical effective stress at which LCC is attained
ΔH	change in height of specimen

1 GENERAL INTRODUCTION

1.1 Background and Motivation

Compressibility measures the degree to which a soil mass decreases in volume in response to an applied external load. It is widely considered during design of geotechnical engineering structures to estimate the settlement of soils under structural load. (Tiwari and Ajmera, 2012, Mohammadzadeh et al., 2014, Singh and Noor, 2012).

Owing to the particulate nature of soils, the usual assumption is that the compressibility of the individual grains is negligible when compared to the compressibility of the mineral skeleton as a whole. Thus, in general for soils, volumetric compression is achieved through particle rearrangement into a tighter packing arrangement or fabric. In granular soils, particle rearrangement into a more compact configuration is achieved through particle reorientation, sliding, rolling and particle breakage if the applied stresses are sufficiently high (Mesri and Vardhanabhuti, 2009, Shipton and Coop, 2012, Uygar and Doven, 2006).

At high stress levels, sands, as non-cohesive granular soils, may be more compressible than cohesive soils, such as clays and silts (Roberts and De Souza, 1958). Even if the compressibility of sands is lower compared with that of clays and silts, the fact that it occurs suddenly as a result of particle crushing may cause catastrophic damage to structures in the early stages of construction (Uygar and Doven, 2006). For this reason, several studies over the past decades (e.g. Terzaghi and Peck, 1948, Vesic and Clough, 1968, Hagerty et al., 1993, Leung et al., 1997, Minh and Cheng, 2013, Roberts and De Souza, 1958) have examined the

compressibility of sands at high pressures with the sole aim of having a better understanding of their mechanical behaviour.

The term high pressure varies from one engineering field to another. In soil mechanics and geotechnical engineering, any pressure exceeding the capacity of a conventional oedometric or triaxial apparatus (about 1-2 MPa) is often referred to as high pressure (e.g. Vesic and Clough, 1968).

The knowledge of mechanical behaviour of soils under high pressure is important for effective design and performance monitoring of large geotechnical engineering structures such as large dams, high waste-rock fills, deep foundations and tunnels which may subject the supporting soils to high stresses beyond those frequently encounter in day-to-day geotechnical engineering problems (e.g. Yamamuro et al., 1996, Vesic and Clough, 1968).

Laboratory information on the compressibility of soils is usually obtained from either oedometer tests or isotropic compression tests. In the oedometer test, also known as one-dimensional (1-D) confined compression test, the soil specimen is subjected to pressure along its vertical axis, while strain in the horizontal direction is reduced to a negligible magnitude. During isotropic compression, the soil specimen is subjected to an equal all-around hydrostatic pressure and is free to strain vertically and laterally (Lambe and Whitman, 1969, Mesri and Vardhanabhuti, 2009).

The results of 1-D confined compression (1-DCC) tests, and isotropic tests are usually presented in plots of void ratio (e) against the logarithm of vertical effective stress (σ'_v) and mean normal effective stress (p'), respectively. These plots are known as a compression curve in the compression plane. For sands, there

is a certain stress level at which the compression curve exhibits maximum curvature. This stress level is referred to as the '*breakdown stress'* or '*critical pressure*' (Vesic and Clough, 1968, Roberts and De Souza, 1958). It is generally accepted that the breakdown stress signifies the onset of major particle crushing and beyond this stress level, the effect of the initial void ratio of the specimen disappears. (Vesic and Clough, 1968, Roberts, 1969). Thus, at sufficiently high stress levels particle crushing becomes the main factor responsible for sand compression. Furthermore, the compression curves of specimens of the same sand compressed from different initial densities tend to converge into a single curve at high stress levels (Fig. 1.1). This unique compression curve is known as the limiting compression curve (LCC) (K_o-LCC when obtained from 1-DCC tests or H-LCC when obtained from isotropic compression tests) (e.g. Pestana and Whittle, 1995).

The stress level that corresponds to the breakdown stress (Fig. 1.1), and consequently where the LCC is attained, is not unique to all sands. Instead it varies from one sand to another and mainly depends on the initial density, particle size (as represented by median particle size, D_{50}), particle size distribution (PSD), particle shape, and particle hardness (mineralogy) (e.g. Coop and Lee, 1993, Roberts, 1964, Yamamuro et al., 1996). Normally, clean quartz sands reach their LCC at stress levels between 10-100 MPa, while other sands with weak particles such as carbonate sands may reach the LCC at much lower stresses between 1-3 MPa (Shipton and Coop, 2012).

Previous studies on high pressure 1-D compression behaviour of non-plastic sands have shown that the LCC reflects the combined effects of PSD and particle

shape (e.g. Altuhafi and Coop, 2011, Cavarretta et al., 2010, Pestana and Whittle, 1995). They have also given an indication of the exclusive effect of particle shape on the LCC, while such effect has not been clearly defined for the PSD. Attempts made by previous investigators to examine the effect of PSD on the LCC, although insightful, did not successfully isolate the effect of D_{50} which in turn makes it impossible to determine whether the resulting changes in LCC are due to changes in shape of the PSD curve or due to changes in D_{50}. Conversely, in this work different PSDs are considered but care is taken to keep the D_{50} constant.

1.2 Research Objective and Dissertation Outline

The general objective of this study is to investigate how particle shape and PSD affect the LCC of quartzitic sands for a constant D_{50}. The progression towards this objective is described in the remainder of the dissertation as follows.

In chapter 2, a review of existing literature on 1-D mechanical response of clean sands is presented. This review covers the two most commonly used mathematical models for representing the LCC and the experimental methods for conducting 1-DCC tests. The effects of PSD, particle shape and mineralogy on the LCC are also presented.

In chapter 3, the materials and methods used in this study are described. This description includes: the 1-DCC testing equipment and loading method, the selected soil types, sample preparation, testing procedure and calculations.

In chapter 4, the results of 1-DCC tests and post-compression sieve analyses are presented, whereas Chapter 5 explores how variations in PSD and particle shape affect the LCC. Correlations between the LCC and the limit void ratios

(e_{max} and e_{min}) are also explored in this chapter, while the final chapter of this dissertation presents a summary of this study, its conclusions and recommendations for future studies.

1.3 Figure

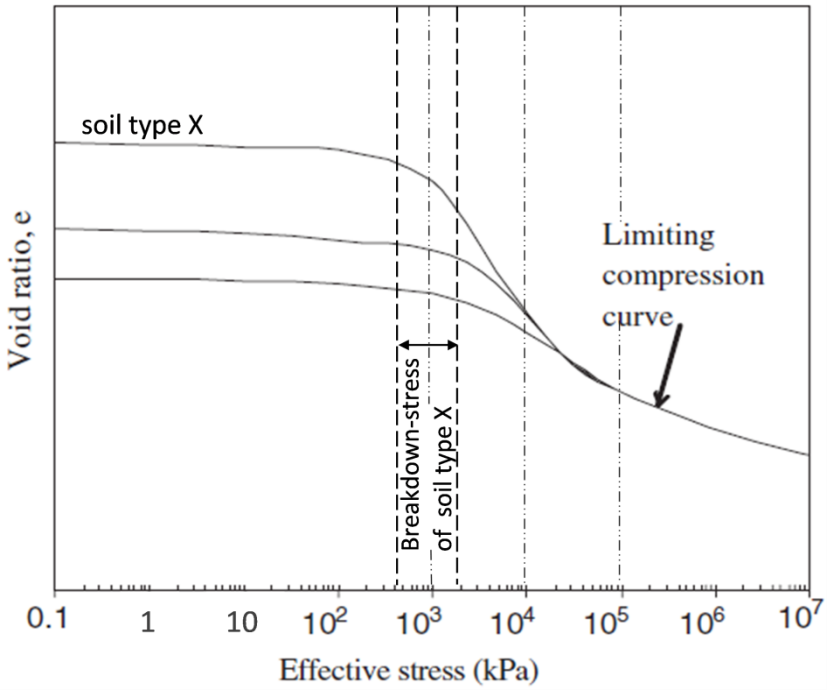


Fig. 1.1 Conceptual representation of the LCC [adopted from Uygar and Doven (2006)].

2 LITERATURE REVIEW

2.1 Introduction

This chapter reviews previous studies on high pressure 1-D compression behaviour of sand which are pertinent to this study; presents the two mathematical models commonly used for representation of the LCC; and examines the effects of PSD, particle shape and mineralogy on the LCC that have been reported on the literature.

2.2 The Limiting Compression Curve (LCC) Concept

In modern soil mechanics and geotechnical engineering, the first study on high pressure 1-D compression behaviour of sands was reported by Terzaghi and Peck (1948). The 1-DCC tests were conducted on sands, sand-mica mixtures and soft Detroit clay to pressures up to 196 MPa. Within the pressure range of about 10 – 100 MPa they observed that the compressibility of the sands is as high as that of the soft clay and attributed this to particle crushing.

Roberts and De Souza (1958), presented comprehensive reports of a series of high pressure 1-DCC tests conducted on Boston blue clay, Venezuelan clay, and well-rounded and very angular quartz sands. The samples were subjected to pressures up to 137 MPa. In agreement with Terzaghi and Peck (1948), they reported that, under high pressure, sand may be more compressible than clay due to particle breakage. The pressure at which the particle crushing becomes apparent was referred to by Roberts and De Souza (1958) as the '*critical pressure'* or the '*break-point*'. They also found that the critical pressure depends on the PSD,

particle shape and initial density of the sample. Namely, they found that the critical pressure was negatively correlated to D_{50} and particle angularity, but positively correlated to the initial density.

Hendron (1963), performed a series of 1-DCC tests on four different quartz sands (Minnesota sand, Pennsylvania sand, Sangamon river sand and Wabash river sand) up to a maximum pressure of approximately 23 MPa. The four sands were selected because of their dissimilarity with respect to PSD and particle shape characteristics. The PSD curves of the sands are shown in Fig. 2.1. In terms of their particle shape, Minnesota sand is rounded, Pennsylvania sand is angular, Sangamon river sand is sub-angular, and Wabash river sand is sub-angular to sub-rounded. The sands were tested at different initial relative densities and it was found that the initial relative density is the most important factor that affects the compressibility of sand at low stress levels where particle crushing is insignificant. However, as the pressure increases to the high pressure range, the effect of initial relative density on the compressibility gradually diminishes. Consequentially, for the Pennsylvania sand, the compression curves of the samples merged into a single curve, i.e. the limiting compression curve (LCC), at a stress level above 14 MPa. Although the other three sands did not reach the LCC, Hendron commented: "*All sands will eventually manifest the same type of behaviour as Pennsylvania sand if high enough pressures are reached*".

After the Hendron (1963) study, many authors in the literature who have studied the compression behaviour of sands (e.g. Vesic and Clough, 1968, Hagerty et al., 1993, Coop and Lee, 1993, Pestana and Whittle, 1995, Yamamuro et al., 1996) have also reported that, when specimens are compressed to a

sufficiently high stress level, the compression curves converge into a single curve that is independent of the initial formation densities. This unique compression curve (Fig. 1.1) has been termed the LCC.

2.3 1-D Confined Compression Test Loading Methods and Equipment

Generally, there are two types of loading methods: stress-controlled and strain-controlled. Both loading methods are used in 1-DCC tests. For instance, ASTM D2435 and ASTM D4186 describe procedures for stress-controlled and strain-controlled 1-DCC tests, respectively. According to the standard, in the stress-controlled 1-DCC test, the sample is subjected to constant discrete load changes (increments and decrements) for a time period of 24 hours (or multiples thereof), or until the completion of primary consolidation of the sample. Conversely, in a strain-controlled 1-DCC test, the sample is compressed axially at a specific rate of strain or deformation which is generally kept constant throughout the test.

It is important to mention that both stress-controlled and strain-controlled 1-DCC tests described in the ASTM standard are primarily devised for estimating the consolidation properties of saturated cohesive soils. However, because of the ever increasing demand for determining the 1-D compression behaviour of cohesionless soils, in both dry and saturated states, and under both low stress levels (where particle breakage is insignificant) and high stress levels (where particle breakage is significant) for theoretical and practical purposes, investigators over the years (e.g. Hendron, 1963, Hagerty et al., 1993, Salazar, 2013) have been using either of these tests for estimating compression properties

of sands with or without modification. For instance, Hagerty et al. (1993) and (Liesker, 2014) among other investigators used a loading method that may be referred to as a modified stress-controlled loading method. In this modified 1-DCC test, the specimen is subjected to an axial compression stress that increases at a constant rate.

Given the lack of standards applicable to 1-DCC tests on sands, significant variability amongst the procedures and testing equipment reported in the literature is evident. Nonetheless, any 1-DCC testing equipment must contain essentially two parts: a loading frame for applying the desirable loadings either stress-controlled or strain-controlled, and a consolidometer or compression mould for confining (housing) the specimen which must be strong enough to withstand the high pressures without any significant lateral expansion.

A brief description of moulds and methods of load application used in a number of previous studies on high pressure 1-DCC conducted on sands are presented in Table 2.1, together with the standards specified in ASTM D2435 and ASTM D4186. It can be seen from the table that both types of loading methods have been used; that the maximum applied stress and dimensions of the moulds vary; and that all the moulds are made of steel (or its alloy) which is inert with sands. Furthermore, given the relatively high elasticity modulus of steel ($E \approx 200$ GPa) its use is likely to also contribute to limiting lateral deformations of the moulds, as opposed to other metals such as copper ($E \approx 117$ GPa) and brass ($E \approx 125$ GPa).

2.4 Representation of the LCC

In characterising the LCC of a soil, it is imperative that one decides on a mathematical model to be adopted for its idealization. There are two widely used models for representing the LCC and the choice of which to use depends largely on the preference of the investigator.

The first model, proposed by Schofield and Wroth (1968), assumes that the LCC of any soil, cohesive or cohesionless, can be approximated by a straight line when the void ratio (or its proxy, the specific volume (v)) is plotted against the logarithm of the effective stress. This model can be written as:

$$e = e_o - \lambda \cdot \log\left(\sigma'/\sigma'_o\right) \tag{2.1}$$

where e_o is the void ratio corresponding to an arbitrary chosen effective stress (σ'_o), λ is the slope of the LCC and σ' is the applied effective stress which could be a vertical effective stress (σ'_v) for 1-DCC tests or a mean normal effective stress (P') for isotropic compression tests.

The second widely used model, suggested by Pestana and Whittle (1995), assumes that the LCC of cohesionless soils, exclusively, can be approximated by a straight line when the logarithm of the void ratio (or its proxy, the specific volume (v)) is plotted against the logarithm of the effective stress (Fig. 2.2). This model can be written as:

$$\log(e) = -\rho_c \cdot \log(\sigma'/\sigma'_r) \tag{2.2}$$

where ρ_c is the slope of the LCC and σ'_r a reference effective stress at a unit void ratio. See Equation 2.1 for the definition of σ'.

McDowell (2005), provided a physical justification for the Pestana and Whittle (1995) model. He shows that the linearity of the LCC of sands in the log$e$-logσ'_v space is consistent with the theory of fractal crushing. The theory assumes that the reduction in the volume of sand sample subjected to 1-DCC when a particle breaks is proportional to the volume of that particle. He also presented a result of a 1-DCC test conducted on a sample of silica sand in semi and double logarithmic void ratio-effective stress spaces (Fig. 2.3 and Fig. 2.4) from which it is apparent that the LCC is best linearized in log$e$-logσ'_v space.

2.5 Factors Affecting the LCC

2.5.1 Effect of PSD on the LCC

In order to examine the effect of initial PSD and density on the compression behaviour of non-plastic soils, Altuhafi and Coop (2011) carried out a series of 1-DCC tests on three sands (Dog's Bay sand, Leighton Buzzard sand and Glacial basalt sand) of different mineralogies and PSDs. The PSD curves and the LCCs, termed the normal compression lines (NCLs) by Altuhafi and Coop (2011), of Dog's Bay sand mixtures are shown in Fig. 2.5 and Fig. 2.6, respectively. It can be seen from these figures that the LCC became less steep as the PSD went from uniformly graded to well graded. Additionally, for the most broadly graded (D4), the LCC did not emerge. In view of this, they concluded that the convergence of the compression curves to a unique LCC is a result of particle crushing which is more pronounced in uniformly graded specimens. Conversely, they suggested that the insignificant amount of particle crushing, and consequently non-convergent

compression behaviour, observed in the well-graded specimens may be because the PSD is broader than the terminal grading of the sample, which is labelled (CD) in Fig. 2.5. Terminal grading generally refers to the grading at which the PSD of a given granular material (under compression) can no longer evolve due to particle crushing (e.g. Altuhafi and Coop, 2011).

It is worth noting that particle crushing, and terminal grading depend on applied stress (e.g. McDowell, 2002, Coop et al., 2004). Therefore it is possible that the well-graded samples could still reach a unique LCC at much higher stress levels. However, the trend observed in the Dog's bay sand (steep LCC for narrow gradation) was also observed in the other sands tested by Altuhafi and Coop (2011).

Additionally, the results of 1-DCC tests conducted by Roberts and De Souza (1958) and Roberts (1964), summarized by Pestana and Whittle (1995), indicate that variation in D_{50} has significant effect on the LCC (Table 2.2 and Fig. 2.7). This effect is evident on the reference vertical effective stress (σ'_r) as shown in Fig. 2.7. In the figure, D_{50} is plotted against σ'_r for the samples of uniform Ottawa sand and ground quartz having the same C_u (C_u = 1.5). It can be seen from the figure that σ'_r decreases with increase in D_{50} for each of the sands.

2.5.2 Effect of particle shape on the LCC

The influence of particle shape on the LCC can be seen from the results of 1-DCC tests conducted by Cavarretta et al. (2010). The tests were performed on spherical (smooth and etched), and crushed glass ballotini of the same particle sizes range (1.0 – 1.4 mm). Their results (Fig. 2.8) show that soils with rounded

particles (smooth or etched) attain the LCC with a steeper gradient, and at a higher stress level than soils with angular particles. This observed trend is consistent with the results of 1-DCC tests conducted by Roberts and De Souza (1958) and Roberts (1964), as earlier presented in Table 2.2 and Fig. 2.7, where rounded quartz sand having higher values of ρ_c and σ'_r than the angular one of the same PSD (D_{50} = 0.6 mm and C_u = 1.5). The results of Cavarretta et al. (2010) also show that surface roughness does not have significant effect on high pressure 1-D compression behaviour of sands, as the compression curves of the spherical (smooth) and etched soil types merged into a unique LCC.

2.5.3 Effect of mineralogy on the LCC

Mineralogy affects the stress level at which the LCC is attained (Shipton and Coop, 2012) as well as the parameters that define the LCC in Equation 2.1 and 2.2. The effect of mineralogy on LCC parameters can be seen in Table 2.2 where sands of different mineralogies (quartz, feldspar and dolomite) with the same particle shape (angular) and PSD (D_{50} = 0.6 mm and C_u = 1.5) have significantly different LCC parameters; the values of ρ_c and σ'_r for the quartz sand are 0.37 and 3.0 MPa, respectively; 0.425 and 2.7 MPa for the dolomite and; 0.39 and 3.6 MPa for the feldspar.

2.6 Concluding remarks

The literature review shows that the intrinsic properties of sand: particle shape, PSD, and mineralogy, all affect the LCC. Importantly, with regards to PSD, the

review shows that the LCC is affected by both the shape of the PSD curve (Altuhafi and Coop, 2011), and the median particle size (D_{50}) (Pestana and Whittle, 1995). In previous studies that have explored the effect of PSD on the LCC, D_{50} has almost always varied. Accordingly, it becomes difficult, if not impossible, to determine whether the resulting changes in LCC are due to variations in the shape of the PSD curve or due to changes in D_{50}.

The current work aims at contributing to our understanding of how the shape of the particles and the shape of the PSD affect the LCC. Achieving this requires removing the effect of D_{50} and mineralogy by keeping them constant for all the tested sands. The following chapter describes the extent to which constant D_{50}s and mineralogies were achieved. Additionally, the experimental procedures are described in detail.

2.7 Figures and Tables

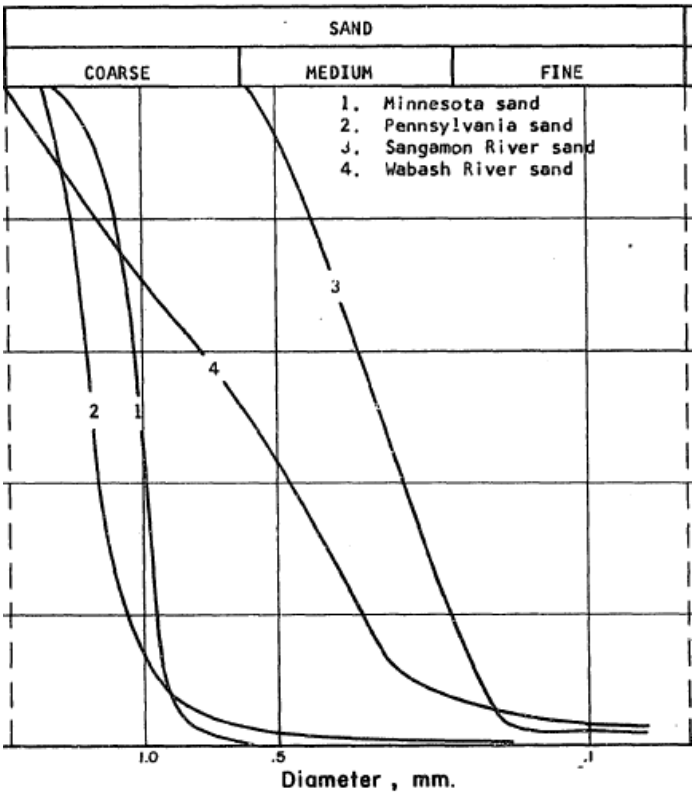


Fig. 2.1 PSD curves of the sands investigated by Hendron (1963).

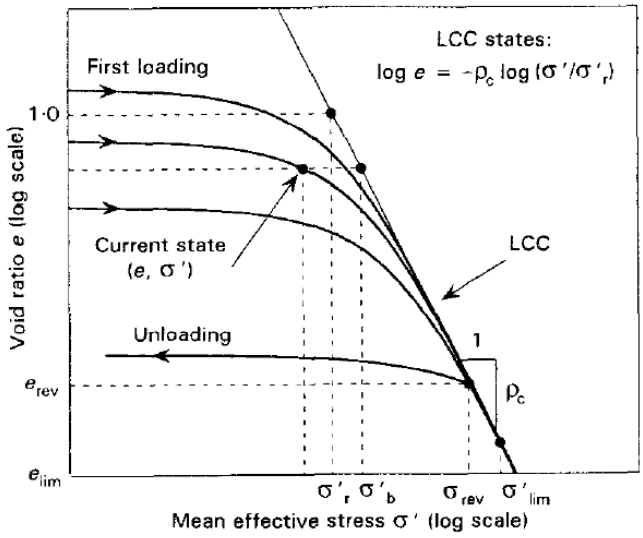


Fig. 2.2 Conceptual representation of the LCC for cohesionless soils (Pestana and Whittle, 1995).

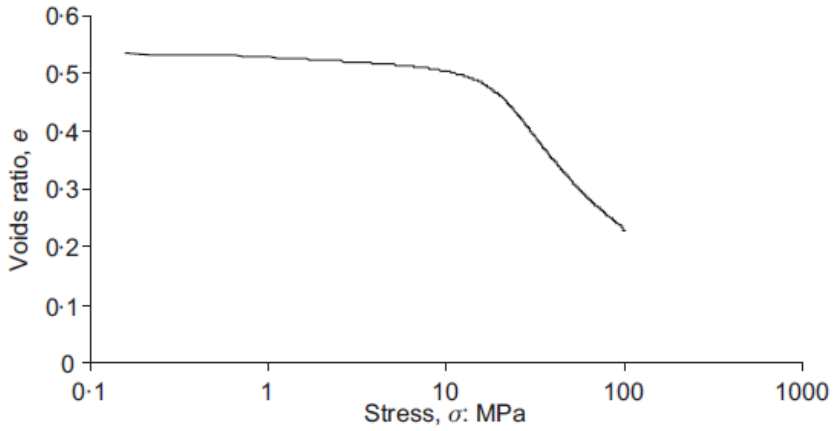


Fig. 2.3 Normal compression curve of silica sand in e-logσ'_v space (McDowell, 2005) as adopted from McDowell (2002).

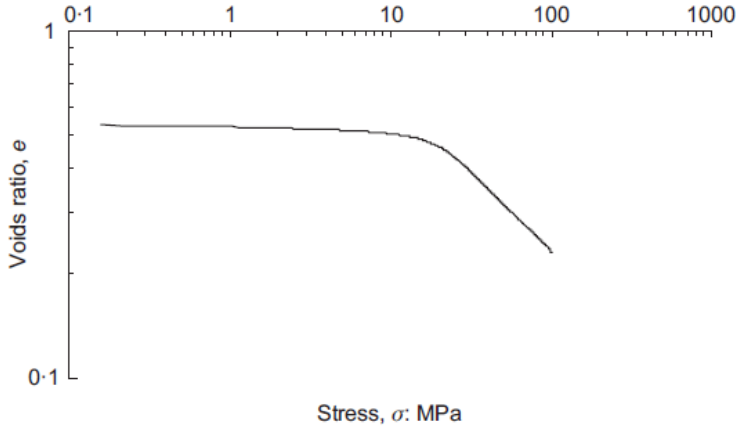


Fig. 2.4 A replot of Figure 2.3 in log$e$-logσ'_v space (McDowell, 2005).

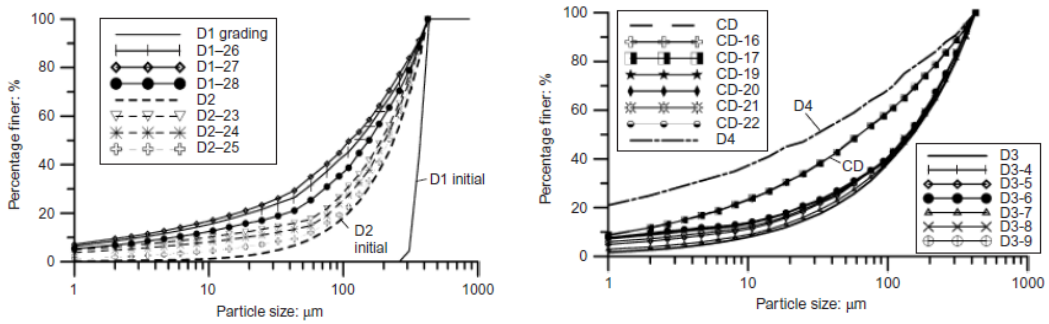


Fig. 2.5 PSD curves of Dog's bay sand. From narrowest to broadest gradation; D1,D2, D3 and D4, and CD (critical grading) (Altuhafi and Coop, 2011).

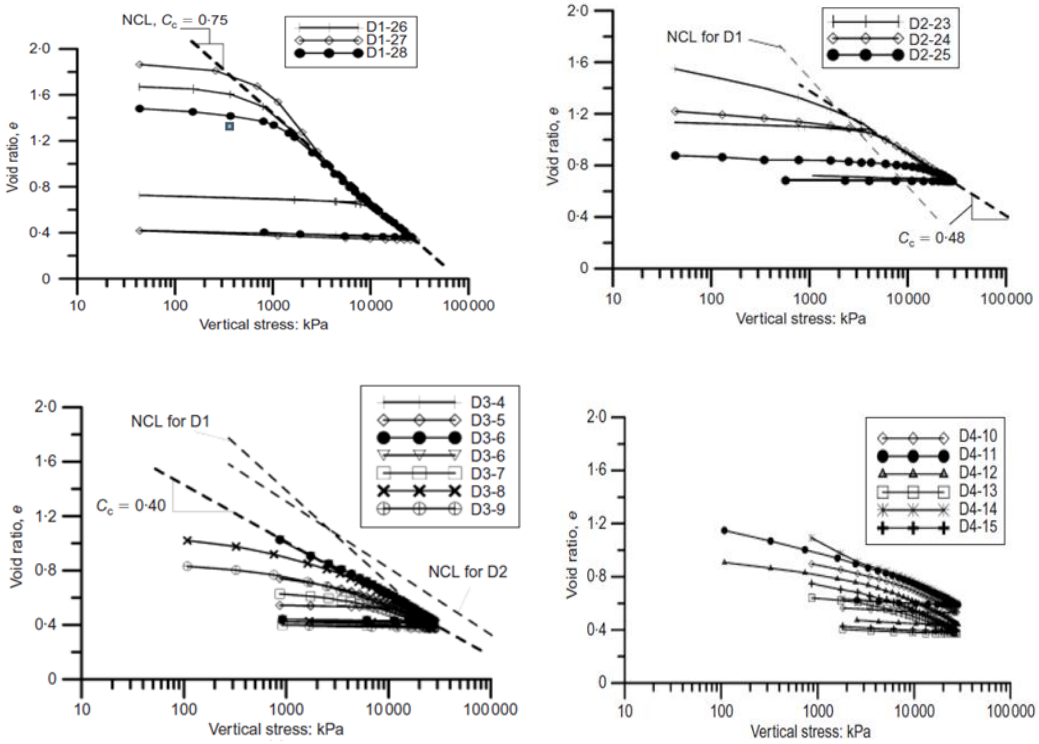


Fig. 2.6 1-D compression curves of Dog's bay sand. From narrowest to broadest gradation; D1, D2, D3 and D4 (Altuhafi and Coop, 2011).

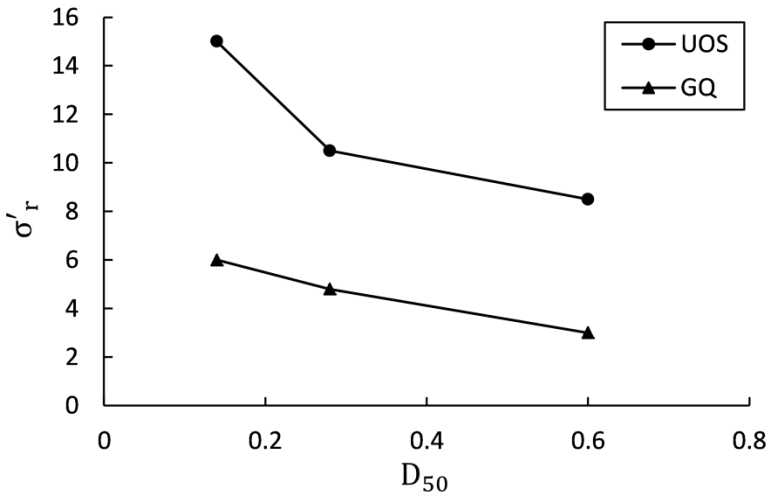


Fig. 2.7 A plot of median particle size against reference vertical effective stress; UOS, uniform Ottawa sand; GQ, ground quartz [tested by Roberts and De Souza (1958) and Roberts (1964)].

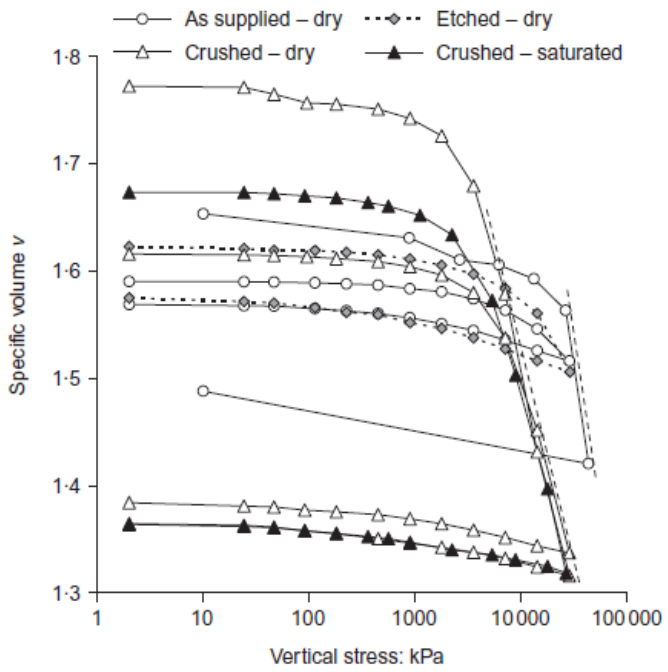


Fig. 2.8 1-D confined compression tests results of Cavarretta et al. (2010). 'As supplied' refers to the spherical glass ballotine particles.

Table 2.1 Moulds description and methods of load application.

References	Height (H) of mould cavity (mm)	Diameter (D) of mould (mm)	D/H ratio	Wall thickness (mm)	Max stress Applied (MPa)	Loading rate	Lateral deformations	Method of Load Application	Mould materials
ASTM D2435-04	12mm min	50mm min	2.5 min	n/s	n/s	As described	0.03% under max. load	Stress-controlled	non-corrosive in relation to the soil tested
ASTM D4186-06	20mm min	50mm min	2.0 min	6.4*	n/s	≯	Should be insignificant	Strain-controlled	As for ASTM D2435-04
Roberts (1964)	4.3-19.1	28.7-69.9	6.67 - 3.66	n/a	138	-	-	Stress-controlled	Hardened steel
Hendron (1963)	50.8	173	3.41	2.4	23	-	Special**	Strain-controlled	Steel
Hagerty et al. (1993)	25	47.8	1.91	66.3	689	44500 kN/min	n/a	Modified Stress-controlled	High yield strength (717 MPa) steel-Alloy
Yamamuro et al. (1996)	76.2	38.1	0.5	32	850	-	0.33%	Strain-controlled	300M VAR steel bar
Nakata et al. (2001)	10	50	5	-	100	0.01 mm/min	n/a	Strain-controlled	-
Shipton and Coop (2012)	20	38 - 50	1.9 - 2.5	-	30	-	-	Stress-controlled	-
Salazar (2013)	31.7	63.6	2.01	12.6	140	0.18 -0.64 mm/min	n/a	Strain-controlled	High-grade 4140 stainless steel alloy
Liesker (2014)	-	-	-	-	67.9	1 kN/sec	-	Modified stress-controlled	-

n/s – not specified

n/a – not available

*****not less than 6.4 mm for applied stresses up to 6 MPa.

≠ by specification of the pore-water pressure ratio

******the ring was specially made to adjust itself to maintain approximately zero lateral strain throughout the test.

Table 2.2 Summary of the results of 1-DCC tests performed by Roberts and De Souza (1958) and Roberts (1964) [adopted from Pestana and Whittle (1995)].

Soil type	**Shape**	**D_{50}**	**C_u**	**ρ_c**	**σ'_r (MPa)**
Uniform Ottawa sand	Rounded	0.60	1.5	0.450 ± 0.015	8.5 ± 1.0
		0.28			10.5 ± 1.0
		0.14			15.0 ± 1.0
Graded Ottawa sand	Rounded	0.40	2.1	0.450 ± 0.015	7.5 ± 0.5
		0.28	2.6		8.5 ± 0.5
		0.30	3.2		8.0 ± 0.5
Ground quartz	Angular	0.60	1.5	0.370 ± 0.010	3.0 ± 0.5
		0.28			4.8 ± 0.5
		0.14			6.0 ± 0.5
Ground dolomite	Angular	0.60	1.5	0.425 ± 0.015	2.7 ± 0.4
Ground feldspar	Angular	0.60	1.5	0.390 ± 0.010	3.6 ± 0.4

3 METHODS AND MATERIALS

3.1 Introduction

This chapter describes the equipment, methods and materials which include: 1-D confined compression testing equipment and loading method; tested soil types; sample preparation; experimental procedures and calculations.

3.2 1-D Confined Compression Testing Equipment

A 1-DCC testing setup was devised to load sand specimens with compressive stresses of up to 190 MPa. This setup is shown in Fig. 3.1 and Fig. 3.2. It consists of a hydraulic loading frame capable of applying constant load, through its bottom ram and a free-to-rotate upper test plate, at a rate which can vary from 10 – 1000 kN/min. The loading frame has an in-built 2000 kN capacity Emery-load cell which was connected to a data-logger in order to have simultaneous readings of load and displacement.

The specimens were confined in a compression mould fabricated from a round steel bar with a yield stress of 494 MPa. The mould is cylindrical and has a height of 80 mm and a diameter of 140 mm. One end of the mould contains a cavity which houses the specimens and which has a depth of 24 mm and a diameter of 65 mm (Fig. 3.3). These dimensions imply that the diameter to height ratio (D/H) of the mould cavity is 2.71, and that the sand specimen is surrounded by ‘wall’ that is 37.5 mm thick. The mould also has two plates with circular openings attached on its diametric opposite sides (Fig. 3.1 and Fig. 3.3). These

plates enable the positioning of two displacement transducers (LVDTs) to measure vertical displacement, and also serve as handles for the mould.

In summary, the compression mould was built to comply with the D/H ratio and materials criteria of a standard consolidometer specified in ASTM D2425–04 and ASTM D4186-06. It may also be likened to the ones described in the literature by a number of previous investigators, who have conducted high-pressure 1-DCC tests (Table 2.1). Furthermore, the wall of the mould vessel is made slightly thicker than the one used by Yamamuro et al. (1996), despite the fact that the specimens would not be subjected to stresses as high as the 850 MPa they applied. Thus the compression mould used herein is not expected to expand laterally up to 0.33% which they reported (Table 2.1) under the maximum stress under consideration (190 MPa).

The load from the compression machine is transferred to the sand specimen by means of a cap. The cap is a solid piece, made from the same material as the mould. It has a cylindrical shape, with a thickness of 24 mm and a diameter of 64.3 mm. Consequently, a clearance of approximately 0.35 mm was created between the specimen containment cavity of the mould and the top cap. The clearance was deemed adequate to allow unobstructed sliding of the top cap into the cavity during compression. The adequacy of this clearance is evident in the repeatability of the compression curves and well defined LCCs obtained in the preliminary tests described in Section 3.3, and in the results that will be presented in Chapter 4.

3.3 Justification for the Selected Loading Method

The modified stress-controlled loading method (Section 2.3) was used in this study. As shown in Table 2.1, this loading method has previously been used by Hagerty et al. (1993) and Liesker (2014). To investigate the effect of loading methods on compression behaviour of sands, preliminary 1-DCC tests were performed on samples of an angular quartz sand using the standard stress-controlled loading method (discrete increments) and the modified method (constant rate of increment). Two samples were tested (Fig. 3.4); one was widely graded and the other was uniformly graded. For both sets of tests the same compression mould (described in preceding Section) and LVDTs were used in order to isolate the loading method as the only variable.

In the modified stress-controlled 1-DCC test, the loadings were applied with the compression machine described earlier (Section 3.2) at a rate of 50 kN/min. In the standard stress-controlled 1-DCC test, the loadings were applied with a universal compression machine capable of maintaining a constant load with an accuracy of 1 kN variation in 10 minutes when high loads (above 50 kN) were applied. The sequence of load application was 2 kN (seating load), 9 kN, 20 kN, 50 kN, 100 kN, 200 kN, and 485 kN. Each load increment was allowed to act on the specimen for 5 mins, since this time was observed to be enough for the completion of primary compression of the specimens. This quick compression time is in agreement with typical behaviour of sands as reported in previous studies (e.g. Donald, 1948, Roberts and De Souza, 1958).

The results (Fig. 3.5) show that the two loading methods yield virtually identical compression curves. This observation justifies the loading method

(modified stress-controlled) used in this study, which was preferred because the continuous rate of stress loading machine is newer with greater loading capacity and easier to use compared to the discrete loading machine (see Fig. 3.6 and Fig. 3.7).

3.4 Selected Soil Types

Eleven quartzitic sands, obtained from four different sources, were selected for this study. Particle shape varied distinctly from one source to the other. All 11 sands had one of the three PSDs shown in Fig. 3.8, which are artificial gradations created in the laboratory. The main characteristic and codes of the 11 sands are summarised in Table 3.1 and their particle shapes are illustrated in Fig. 3.9. It can be seen from the table that the material from the Lowveld River could only be prepared into the narrow and intermediate gradations. This was due to the characteristics of the natural gradation of the material. From Fig. 3.8 it can also be seen that the three gradations investigated have the same D_{50} of 0.6 mm. This was done in attention to the results obtained by Pestana and Whittle (1995) which showed that variations in D_{50} affect the location of the LCC. Accordingly, with the selected PSD curves, the effect of D_{50} is eliminated thus isolating the effect of the shape on the LCC for sands from the same source.

The specific gravity (G_s) was 2.65 for the three natural sands and 2.52 for the glass beads (ASTM D854, water pycnometer method). The minimum index density tests were performed in accordance with ASTM D4254, while the maximum index density tests were conducted in accordance with the method suggested by MacRobert and Torres-Cruz (2016) for sand-silt soils. Using the

specific gravities and the index densities, the corresponding e_{min} and e_{max} of the samples were determined. The values of the e_{min} and e_{max} are given in Table 3.1.

The mineralogy of the particles was determined by X-ray diffraction and is summarised in Table 3.2. It is evident that for sands from different sources, the effect of particle shape has not been entirely isolated because, although all the sands are quartzitic, there are some variations in mineralogy that could have effects on the LCC (Shipton and Coop, 2012, Pestana and Whittle, 1995).

The particle shapes of the four different sources were characterised based on their sphericity (*S*) and roundness (*R*). This was done by observing a group of well-scattered grains that are similar in size to the D_{50} (710 – 600 μm) under an optical microscope and comparing their shape against the Krumbein and Sloss (1963) particle shape chart (see Fig. 3.9 and Fig. 3.10). This procedure was repeated three times, where 15 – 20 individual particles were carefully examined for each of the selected granular materials, and the average values are given in Table 3.1. It is important to mention that particle roughness (surface texture), which is the third parameter commonly used for particle shape description (e.g. Barrett, 1980, Sukumaran and Ashmawy, 2001, Clayton et al., 2009, Cho et al., 2006), is not considered herein because it has no effect on 1-D compression behaviour of granular soils at the LCC state as pointed out in Section 2.5.2**.**

3.5 Correlations amongst Index Properties

As a means of ensuring self-consistency of the set of index parameters calculated for each soil type, the correlations among the different index properties (Table 3.1) were explored. The relationship between e_{max} and e_{min} was

investigated by plotting their obtained values against each other in Fig. 3.11. It can be seen from the figure that there is a direct correlation between them; higher e_{max} translates into higher e_{min} and vice versa. This observed trend is in agreement with those reported by Cubrinovski and Ishihara (2002) for a wide variety of soil types. The effects of PSD and particle shape on the e_{max} and e_{min} are also examined in Fig. 3.12 through Fig. 3.15.

The obtained e_{max} and e_{min} are plotted against C_u in Fig. 3.12 and Fig. 3.13, and against particles roundness in Fig. 3.14 and Fig. 3.15. As expected (e.g. Cho et al., 2006, Biarez and Hicher, 1994, Cubrinovski and Ishihara, 2002), it can be seen from the figures that e_{max} and e_{min} are clearly a function of PSD shape and particle shapes in such a way that they increase with uniformity of the PSD and decrease with increase in the roundness of the particles.

3.6 Sample Preparation and Experimental Procedure

At least four 1-D confined compression tests were performed on each of the eleven soil types tested. All specimens were tested dry and prepared at initially loose and dense states. The specimens were prepared directly in the compression mould cavity which was in turn placed on two overlapping sheets of A3 paper laid on a horizontal surface. A known mass of the sample, usually 20 % greater than the mass anticipated to fill the mould was weighed out to prepare the specimen.

For the loose state specimens, the known mass of the sample was poured in a small handheld funnel whose 6 mm diameter outlet rested on the bottom of the compression mould cavity. The funnel was then gradually lifted in spiral manner, allowing the sample to be deposited with minimum disturbance until the mould

was full. For the dense state specimens, the mould was filled in five layers. Following the pouring of each layer, the mould was tapped horizontally with a rubber mallet until there was no further noticeable settlement. In both instances, excess material above the top surface of the specimen was carefully trimmed with a straightedge and the mould was gently cleaned with a brush. Afterwards, the mould top cap was centrally placed on the prepared specimen and the mould was then positioned in the compression machine. The sand particles that fell on the A3 paper were retrieved and weighed. The mass of the specimen, M_S, was then obtained by subtracting the mass of the remaining sample and the mass of retrieved material from the initial mass of the sample.

Upon placing the prepared specimen in the compression machine, two LVDTs were positioned to measure the vertical displacements of the specimen during compression. For at least two tests made on each of the eleven soil types, a third LVDT was introduced to measure the horizontal expansion of the mould under compression. The horizontal LVDT was held by a magnetic stand with its tip placed close to the upper edge of the compression mould (Fig. 3.1) where largest lateral expansion is expected.

It is important to point out that only one horizontal LVDT was used because of space limitation of the compression machine (Fig. 3.6) and, because ideally owing to the geometry of the mould the readings taking at a point on its circumference would be the same throughout the circumference. The proof of this claim can be seen from Fig. 3.16. In the figure, the percentage lateral expansion of the mould, taken by two horizontal LVDTs used in one of the preliminary tests conducted using the discrete increments compression machine, is plotted against

the vertical effective stress. The maximum lateral strain measured was 0.26 %. This value is greater than 0.03 % specified in ASTM D2435 (Table 2.1), but compares favourably with the radial strain of 0.33% reported by Yamamuro et al. (1996). It is noted that the radial strain measured at the circumferential edge of the mould may differ from the lateral strain experienced by the specimen within the cavity in which it is housed. However, given the experimental difficulties in measuring lateral strain inside the cavity, the radial strain computed from the LVDT readings were used herein as a proxy for the radial strain of the specimen. This approach was deemed preferable to not reporting any radial strains as often occurs in the literature (Table 2.1).

Following the positioning of the LVDTs, the testing was commenced with the load and displacement readings logged at two seconds intervals. All specimens were loaded at selected rate of 50 kN/min until the load reached about 630 kN which corresponds to a vertical compressive stress of 190 MPa on the specimens. Results from preliminary tests indicated that this stress level was sufficient for the attainment of the LCC for all the selected soil types. The loading was then stopped so as to keep the position of the loading platform constant and the final height of the specimen, H_f, was taken using a telescopic measuring gauge (Fig. 3.17) used in tandem with a digital caliper. The precision of H_f readings taken at diametric opposite points around the perimeter of the mould is 0.15 mm on average for all tested specimens.

The loading platform was then lowered without any further reading of load or displacement, the mould was removed and the compressed specimen was

retrieved for post-compression PSD analysis to determine the extent of particle crushing.

3.7 Experimental Data Presentation, Processing and Calculations

3.7.1 Void ratio calculation

The readings taken by the two vertically positioned LVDTs were averaged to calculate the void ratio, *e*, under any particular pressure during the test. The void ratio was calculated as follows;

$$e = \frac{V_V}{V_S} = \frac{V_T - V_S}{V_S} \tag{3.1}$$

where V_V is the volume of voids, V_S is the volume of solids and V_T is the total volume of the specimen. V_S was calculated as:

$$V_S = \frac{M_s}{G_s \times \rho_w} \tag{3.2}$$

M_s = mass of the specimen,

G_s = specific gravity of the specimen

ρ_w = density of water (taken as 1 g/cm^3).

Since V_S was constant throughout the test, the void ratio was determined by changes in V_T only. V_T was calculated as:

$$V_T = A \times H_s \tag{3.3}$$

A = cross sectional area of the specimen

H_s = equivalent height of specimen

$$H_s = H_f + \Delta H \tag{3.4}$$

H_f = final height of the specimen measured when the maximum load was reached.

ΔH = change in height of the specimen measured by LVDTs

3.7.2 1-D confined compression data processing and presentation

The compression data from the tests were plotted from 10 MPa to the maximum stress level attained (190 MPa). Limitations in the minimum load that can be applied with the compression machine did not allow the calculation of the compression curve of some of the specimens at stress levels below 10 MPa (i.e. sometimes the initial stress was lower than 10 MPa). Each test is defined by a code whose first two letters indicate the soil type (see Table 3.1), followed by the relative density expressed as a percentage under a compressive stress of 10 MPa. For example, AB_123 represents angular, broad PSD, 123 % relative density at 10 MPa.

For each test, the resulting compression curve was defined by over 250 data points. However, for ease of data analysis and presentation each compression curve was reduced to 35 points that corresponded to σ'_v values that were equally spaced on a logarithmic scale between 10 MPa to 190 MPa. For every reduced compression curve, the void ratio that corresponded to each of the 35 σ'_v values was linearly interpolated from the measured compression curve defined by over 250 data points. This approach is illustrated in Fig. 3.18.

Pestana and Whittle (1995), defined the LCC as the portion of the compression curve for which the effect of initial density disappears. In this study, the LCC was determined as follows. If the number of compression curves measured on a given soil type is termed n, this implies that there are *n* values of void ratio measured at each of the 35 stress levels used to define each curve. The

difference between the *n* void ratios measured at a particular level of stress is a function of the stress level. That is, the difference is large when the stress level is low which means the influence of the initial density of the samples is significant. However, the difference becomes smaller as the compression curves approach the LCC state and tend to merge into a unique curve. This is illustrated in Fig. 1.1, where three compression curves are presented (n = 3). As suggested by the vertical lines, the difference between the three void ratios (*n* = 3) is significant at a stress of 1000 kPa. This difference reduces progressively as the stress increases to 10,000 kPa and 100,000 kPa where the LCC is reached and the difference is relatively small. As suggested by the figure, the differences in void ratio remain small and approximately constant once the LCC is reached. Accordingly, in this study, the standard deviation of the void ratios measured at a particular stress level was computed by considering the n compression curves corresponding to a soil type. This standard deviation was a means of quantifying the difference between void ratios which is expected to reduce and stabilise as the compression curves reach the LCC. The standard deviation was then plotted against stress level, and it was assumed that the LCC was defined over the stress range where the standard deviation was small and stable. For instance, Fig. 3.19 shows the plot of standard deviation of void ratio versus effective stress for the angular broad PSD (AB) soil type. In this case the standard deviation of the void ratio is seen to largely stabilise at a minimum value of 0.00025 when σ'_v reaches 40 MPa. Accordingly, the σ'_v domain of the LCC was taken as σ'_v greater than 40 MPa. Furthermore, in order to define a unique LCC for each of the tested soil types, the *n* void ratios that corresponded to a unique stress level within the LCC range were

averaged. The LCC was then characterized with the compression model suggested by Pestana and Whittle (1995) (Equation 2.2).

3.7.3 Particle crushing measurement

The amount of particle crushing induced by the compression on each of the soil types was quantified using the breakage parameters proposed by Hardin (1985) (Fig. 3.20). Hardin suggested that the amount of breakage could be measured by the area between the pre and post-compression PSD curves, considering only the part above 74 μm sieve size. He devised two different quantities: the breakage potential (B_p), and the total breakage (B_t). B_p is defined as the area between the pre-compression PSD curve of the sample and a vertical at 74 μm; while B_t is defined as the area between the pre and post-compression PSD curves. He then defined the relative breakage of the sample, B_r, as the ratio of B_t to B_p. B_r has a lower limit of zero, which means no particle breakage, and a theoretical upper limit of unity which represents complete breakage of the particles to the extent that no particle remains larger than 74 μm.

3.8 Summary

In this chapter, the 1-DCC testing equipment used in this study was described. The adopted method of load application was justified. Also, the selected soil types were described and summarised in Table 3.1. Finally, the conceptual framework used for sample preparation, experimental procedure, and experimental data

presentation, processing and calculations are laid out. The following chapter will present the experimental results.

3.9 Figures and Tables

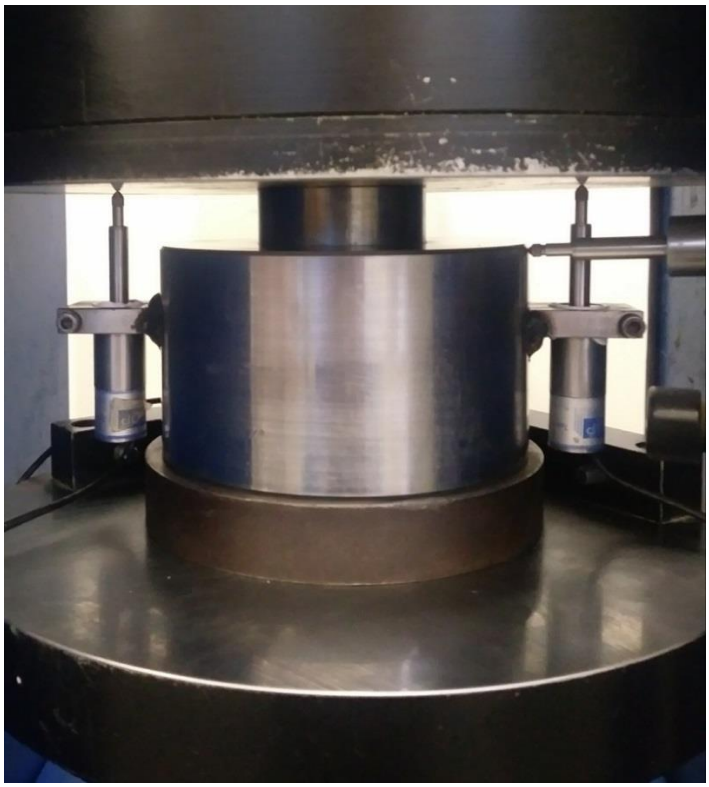


Fig. 3.1 Compression mould placed in the compression machine and with the three displacement transducers in place.



Fig. 3.2 1-D confined compression testing equipment data acquisition system.

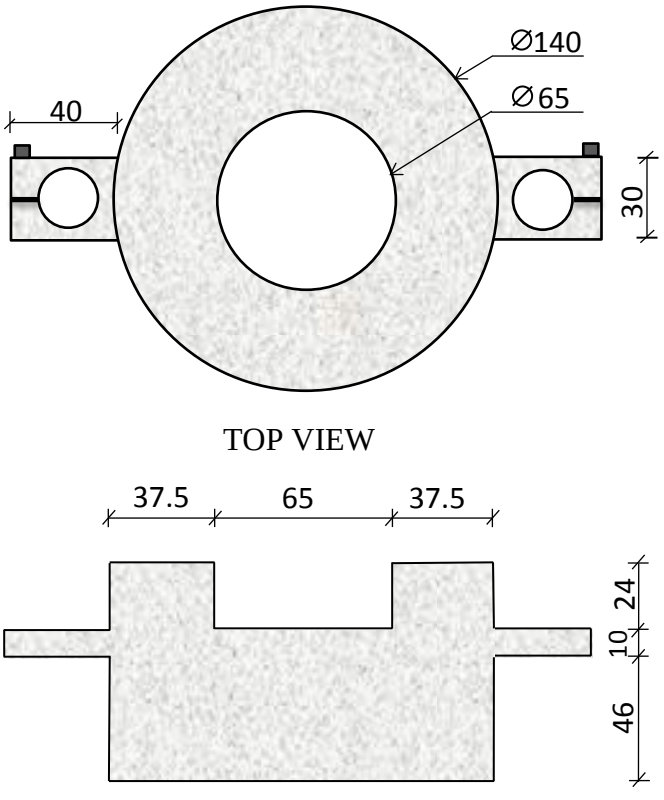


Fig. 3.3 Schematic diagram of the compression mould vessel (all dimensions are in mm).

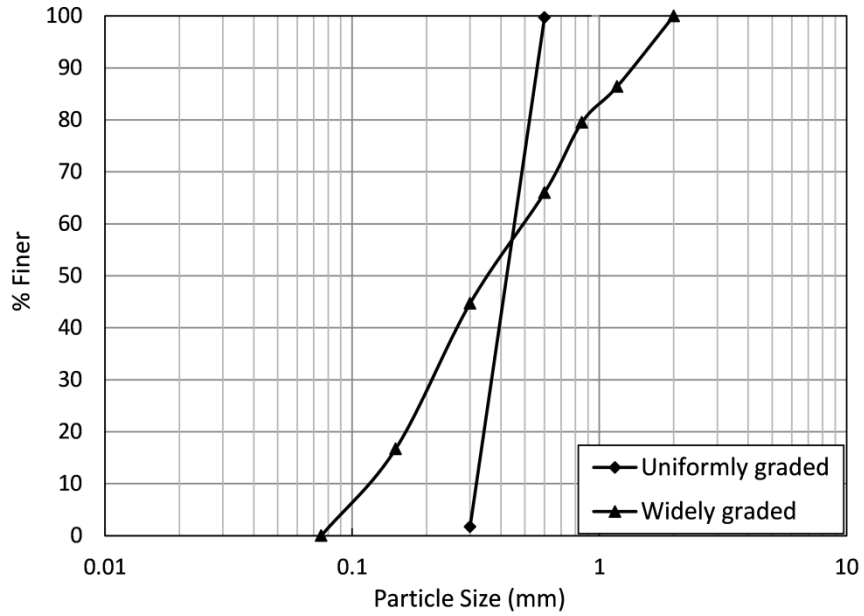


Fig. 3.4 PSD curves of the samples used for preliminary study.

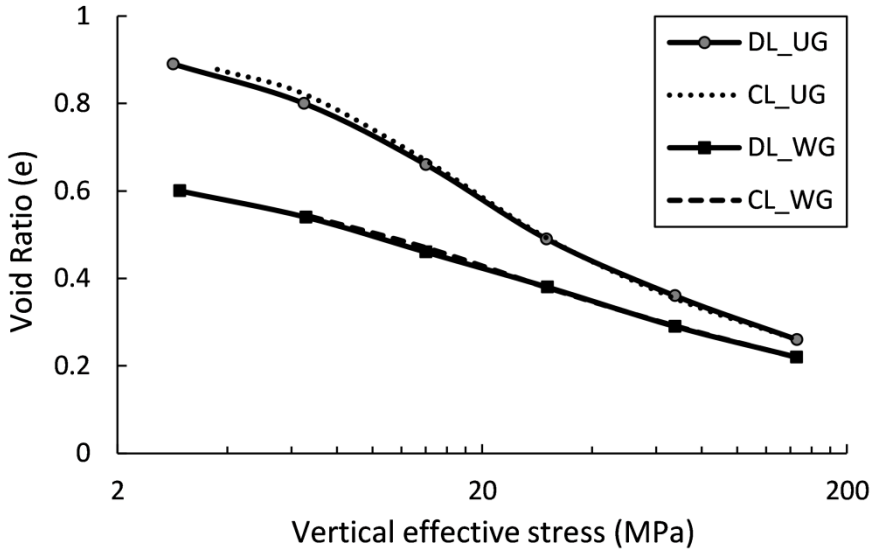


Fig. 3.5 Compression curves of the samples used for preliminary study; DL; discrete loading compression machine; CL; continuous loading compression machine; UG, uniformly graded PSD; WG, widely graded PSD.



Fig. 3.6 Continuous rate of stress loading compression machine.

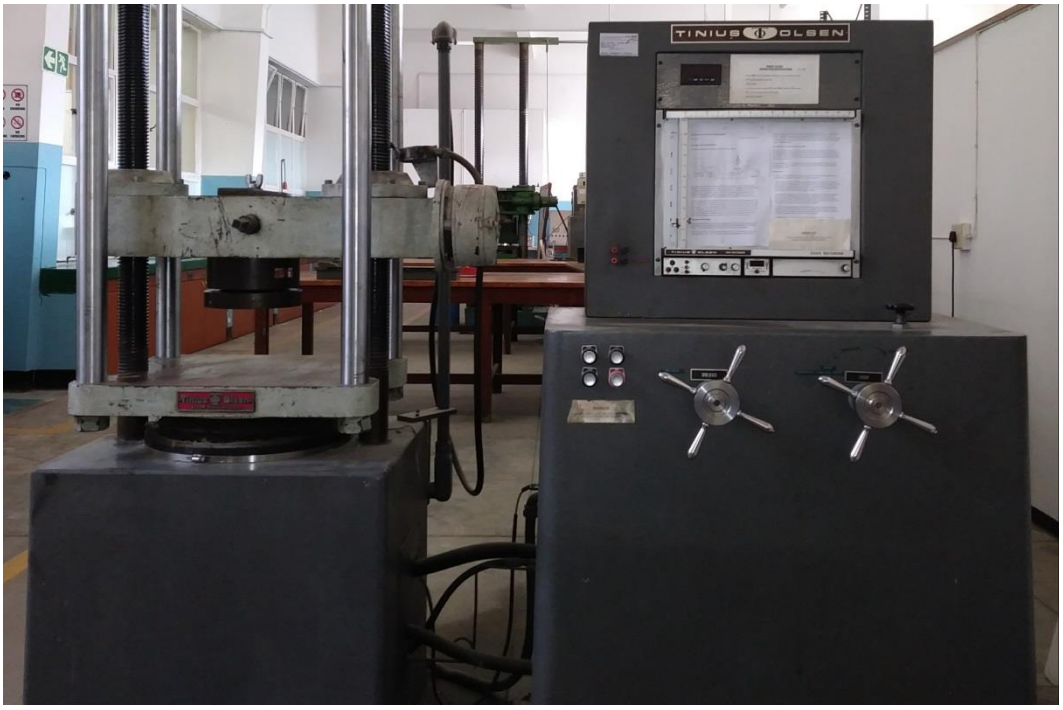


Fig. 3.7 Discrete loading compression machine.

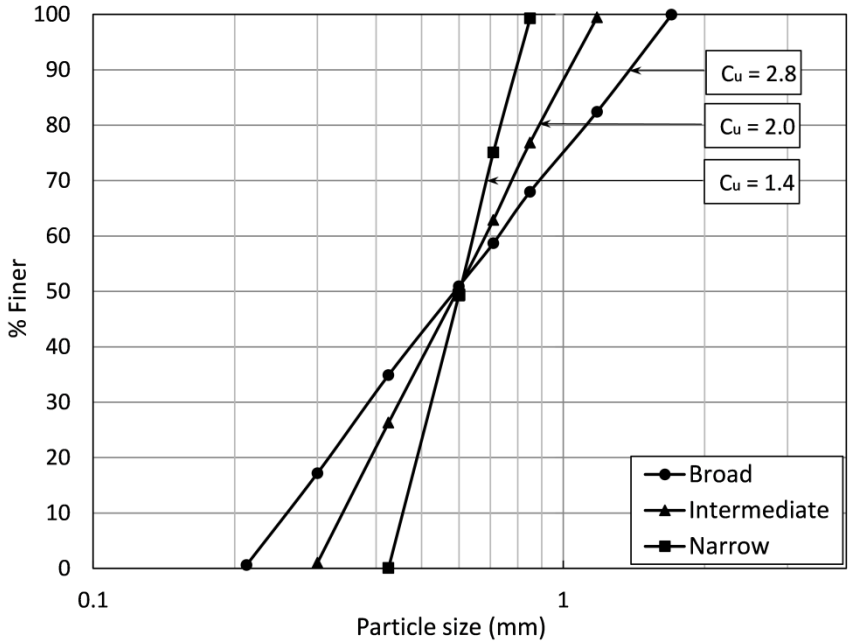
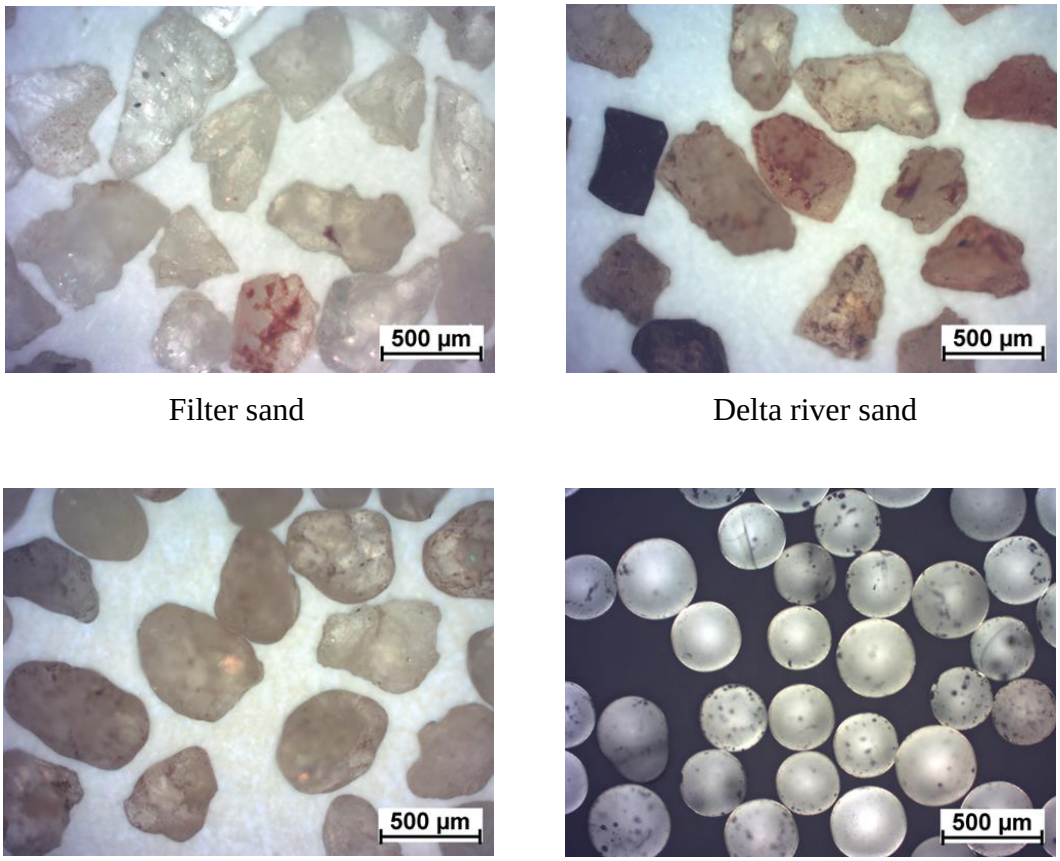


Fig. 3.8 PSD curves of the soil types tested.



Filter sand | Delta river sand

Lowveld River sand | Glass beads

Fig. 3.9 Microscope images showing the particle shape of the four different sources of granular materials tested.

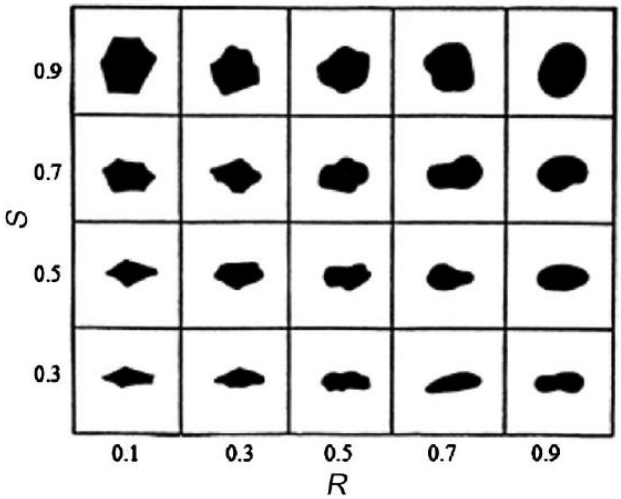


Fig. 3.10 Krumbein and Sloss (1963) Particle shape determination chart.

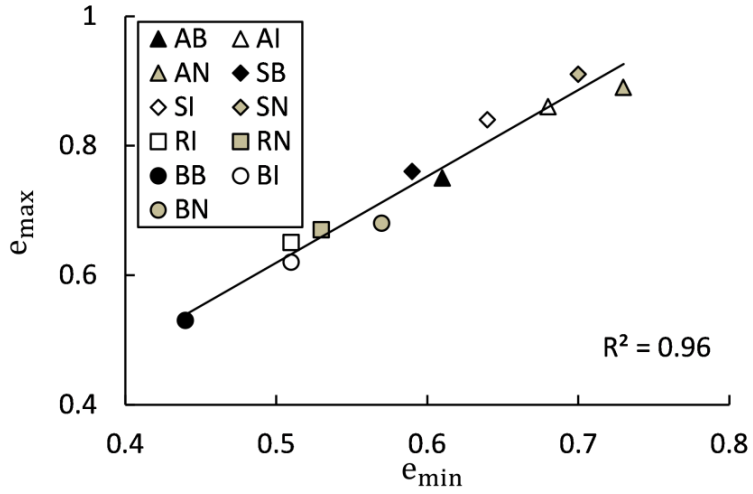


Fig. 3.11 Relation between e_{max} and e_{min} of the selected soil types.

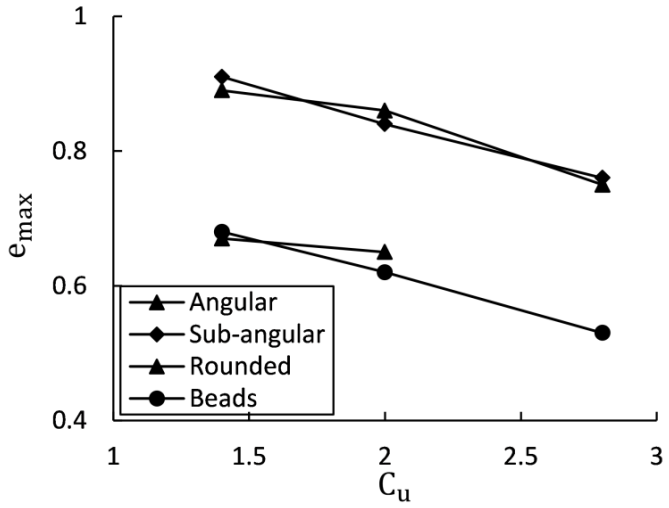


Fig. 3.12 Relationship between e_{max} and PSD.

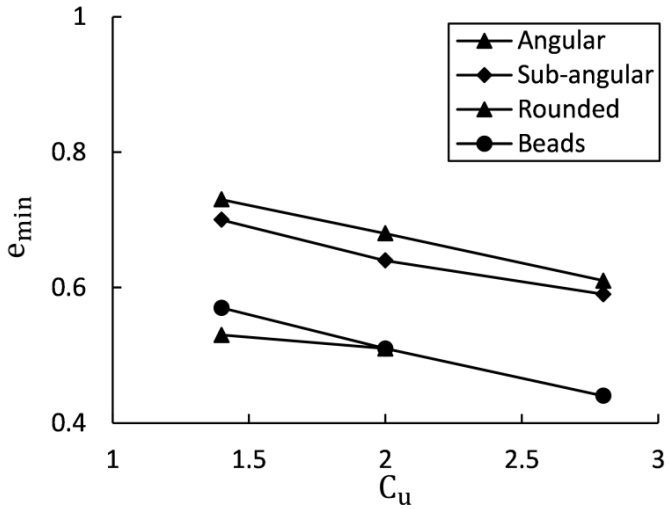


Fig. 3.13 Relationship between e_{min} and PSD.

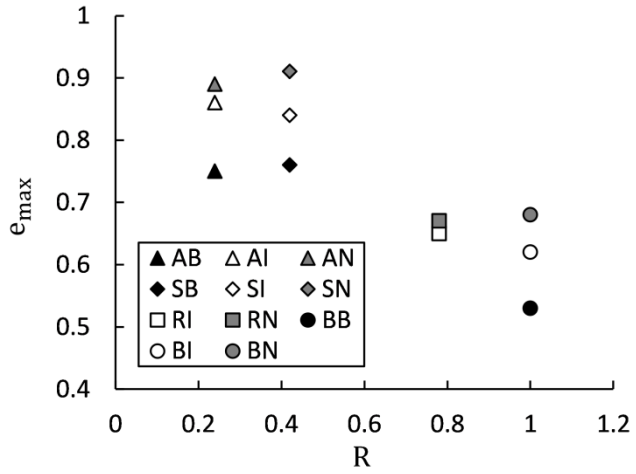


Fig. 3.14 Relationship between e_{max} and particle roundness.

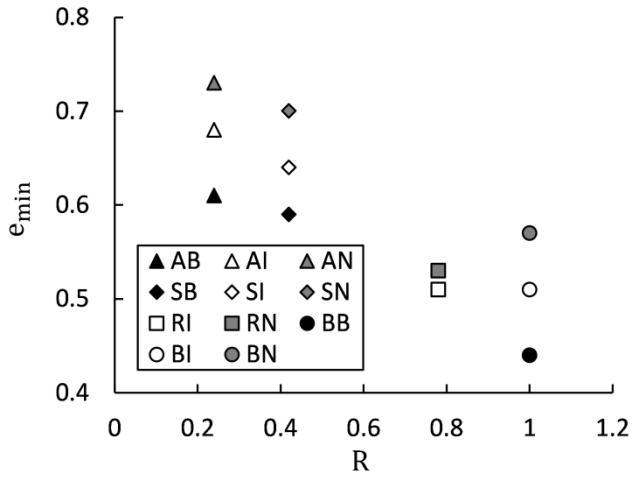


Fig. 3.15 Relationship between e_{min} and particle roundness.

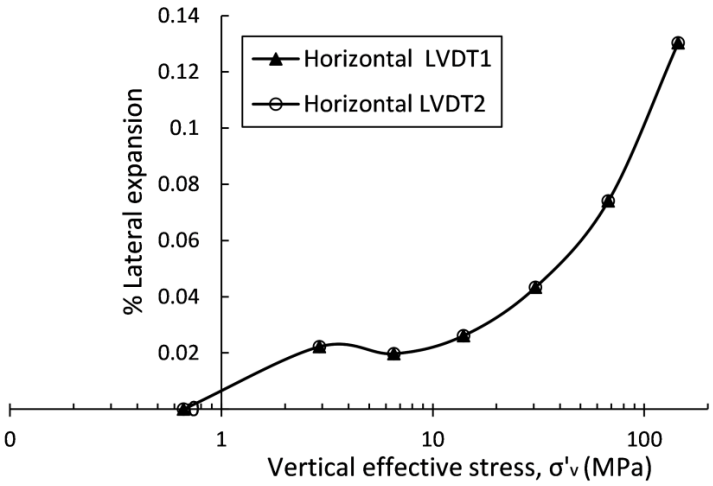
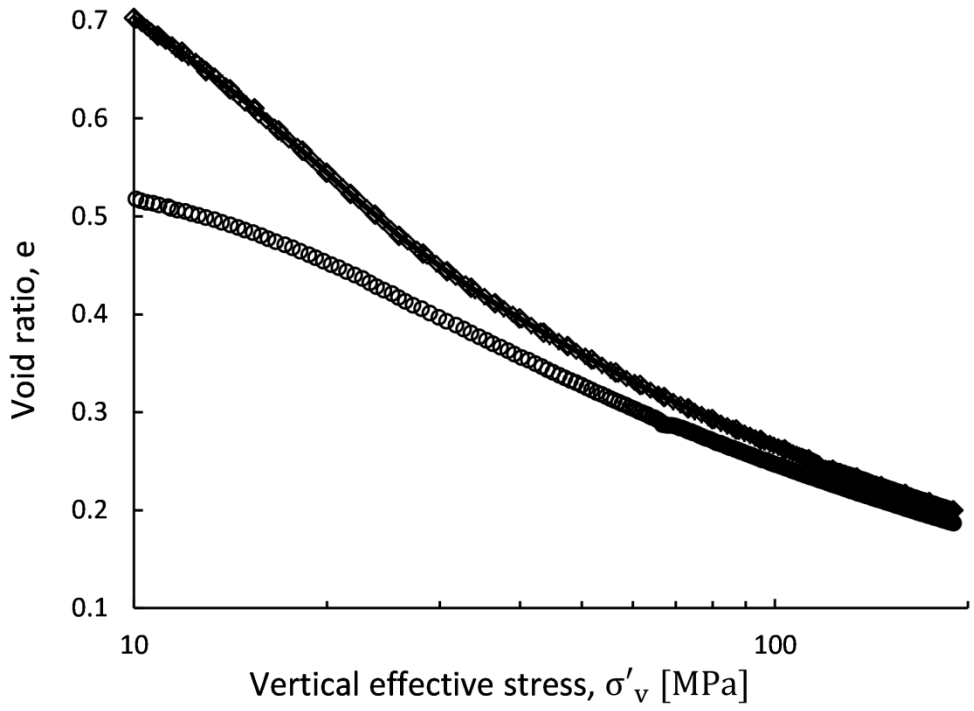


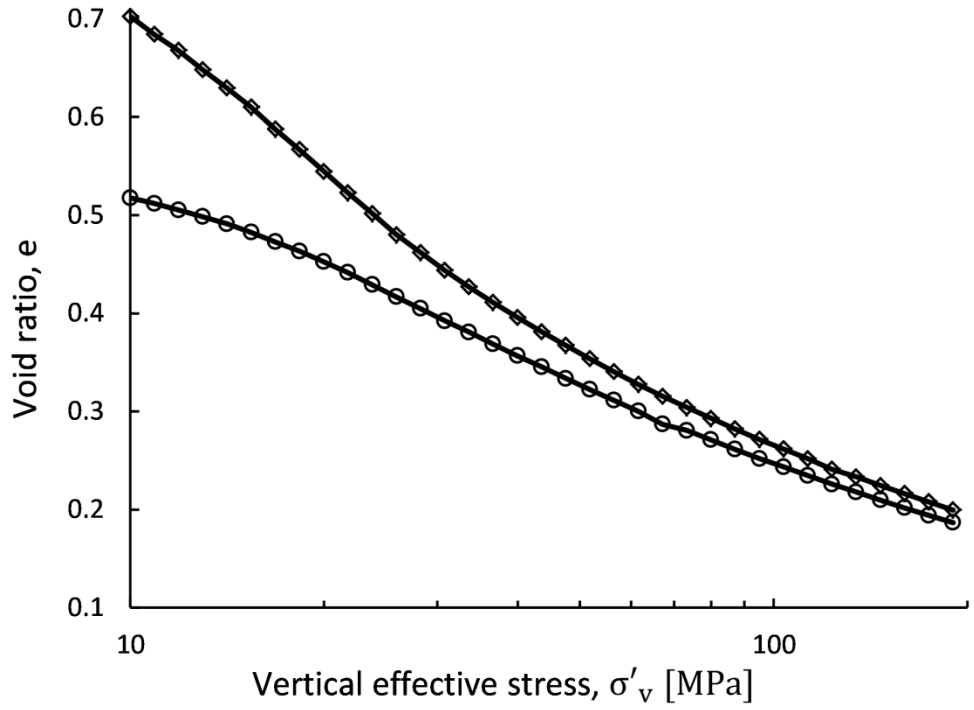
Fig. 3.16 Compression mould lateral expansion measured from two horizontal LVDTs.



Fig. 3.17 Telescopic gauge used to measure the final height of the specimens, H_f.



(a)



(b)

Fig. 3.18 Illustration of the approach used in defining the 1-D compression curve obtained herein; (a) initial data points (b) refined 35 data points.

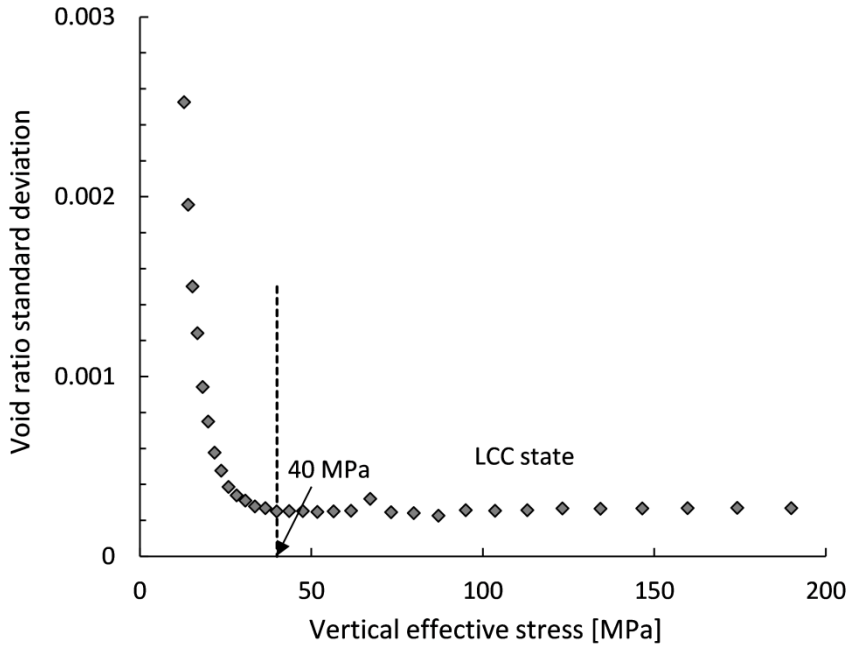


Fig. 3.19 LCC determination for the angular, broad PSD soil type.

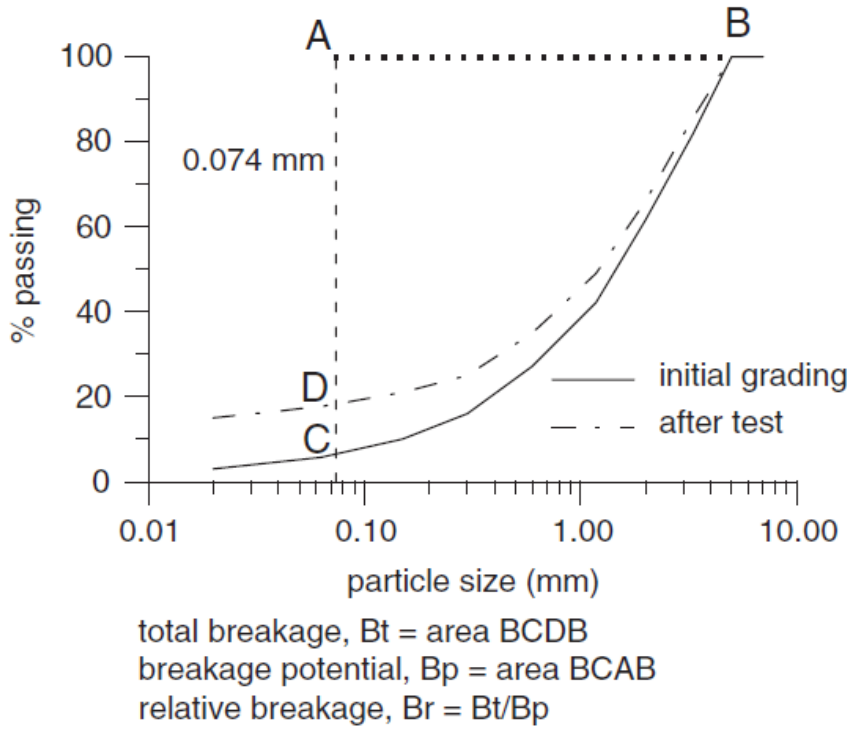


Fig. 3.20 Hardin (1985) particle breakage measurement parameters.

Table 3.1 Fundamental index properties of the selected soil types.

Soil type	D_{50} (mm)	D_{10} (mm)	D_{60} (mm)	C_u	R	S	Shape term	e_{max}	e_{min}
AB	0.6	0.265	0.73	2.8	0.24	0.58	A	0.75	0.61
AI	0.6	0.345	0.685	2.0	0.24	0.58		0.86	0.68
AN	0.6	0.465	0.65	1.4	0.24	0.58		0.89	0.73
SB	0.6	0.265	0.73	2.8	0.42	0.61	SA	0.76	0.59
SI	0.6	0.345	0.685	2.0	0.42	0.61		0.84	0.64
SN	0.6	0.465	0.65	1.4	0.42	0.61		0.91	0.70
RI	0.6	0.345	0.685	2.0	0.78	0.81	R	0.65	0.51
RN	0.6	0.465	0.65	1.4	0.78	0.81		0.67	0.53
BB	0.6	0.265	0.73	2.8	1	1	B	0.53	0.44
BI	0.6	0.345	0.685	2.0	1	1		0.62	0.51
BN	0.6	0.465	0.65	1.4	1	1		0.68	0.57

Soil type: AB, AI and AN represent angular broad, intermediate and narrow PSD; SB, SI and SN represent sub-angular broad, intermediate and narrow PSD; RI and RN represent rounded intermediate and narrow PSD; while BB, BI and BN represent beads broad, intermediate and narrow PSD, respectively.

Particles shape term: A – Angular; SA – Sub-angular; R – Rounded; B – Beads.

Table 3.2 XRF major chemical composition analysis results.

Sample	**Chemical composition (%)**		
Filter sand	SiO_2 (97.52 %)	Al_2O_3 (0.60 %)	LOI (0.57 %)
Delta river sand	SiO_2 (82.00 %)	Al_2O_3 (8.46 %)	K_2O (3.73 %)
Lowveld river sand	SiO_2 (95.99 %)	Al_2O_3 (1.29 %)	LOI (0.58 %)
Glass beads	SiO_2 (71.46 %)	Na_2O (13.74 %)	CaO (9.00 %)

4 EXPERIMENTAL RESULTS

4.1 Introduction

Fifty 1-DCC tests were performed. The main features of the tests are presented in Table 4.1 and discussed in this chapter.

4.2 1-D Confined Compression Curves

A typical result of 1-DCC tests performed on the soil types tested in this study is presented in e-logσ'_v and log$e$-logσ'_v spaces in Fig. 4.1(a) and Fig. 4.1(b), respectively. Both of these spaces are used in the technical literature as pointed out in Section 2.4. It is evident from the figure that the last part of the compression curves, where the LCC is expected to develop, is better linearized in the log$e$-logσ'_v space than it is in the conventional e-logσ'_v space. It is interesting to point out that the anticipated LCC portion of the compression curve of the beads soil type is not as linear as that of the natural sand, indicating that not all granular soils linearize equally well, even, in the log$e$-logσ'_v space.

However, in this current work the compression behaviour of the tested soil types will be characterised with the coefficient of compressibility, which has been termed a_v by precious researchers (e.g. Donald, 1948, Lambe and Whitman, 1969). The parameter a_v is numerically equal to the slope of compression curve plotted on natural space of e versus σ'_v (Fig. 4.1(c), Equation 4.1). The usual practice of multiplying a_v by 1000 has also been adopted herein to avoid inconveniently small values.

$$a_v = -(\delta e/\delta \sigma'_v) \times 1000 \quad (4.1)$$

The compression curves of all the intermediate PSD soil types tested are presented in Fig. 4.2 to Fig. 4.5 (see Appendix A for the corresponding plots of the remaining soil types). In order to investigate the effect of initial density, PSD and particle shape on the compression behaviour of the samples, the coefficients of compressibility (a_v) of representative samples of the tested soil types are plotted against the vertical effective stress in Fig. 4.6 through Fig. 4.14. It can be seen from Fig. 4.6 to Fig. 4.9 that for samples of a soil type, compressibility increases with decrease in the initial density (relative density @ 10 MPa as here used) at the early stage of the compression curves, and they later merge into a single compression curve, which signifies the emergence of the LCC state. Fig. 4.10 to Fig. 4.13 show that compressibility increases with PSD's uniformity, for samples of a given particle roundness having approximately the same initial density. These observed trends are in agreement with the typical well-known behaviour of sands (e.g. Hendron, 1963, Altuhafi et al., 2012, Nakata et al., 2001). However it can be seen from Figs 4.11 – 4.14 that above a stress level of about 110 MPa for the angular and sub-angular samples, and 135 MPa for the rounded and beads samples, the compressibility of the samples appears to be independent of PSD.

With regard to the effect of particle shape on compressibility, it can be seen from Fig. 4.14(a) that particle does not have a simple influence on compressibility of non-plastic soils, but instead the influence varies with the applied stress. The figure shows that compressibility decreases with increased particle roundness at stress region below 47 MPa with the AN soil type having the highest

compressibility. Between 47 MPa to 58 MPa the RN soil type takes the lead. The BN soil type overtakes the RN between 58 MPa to about 140 MPa. And afterwards, the effect of particle shape on compressibility diminishes as the compressibility curves of all the soil types merge into a single line. It is interesting to note that, since compressibility increases with decrease in initial density (Fig. 4.6 - Fig. 4.9), one would expect the AN and SN samples with relative density (RD) @ 10 MPa of 119 % and 100 %, respectively, to be more compressible than the RN and BN samples with RD @ 10 MPa of 121 % and 127 %, respectively. It can be seen in Fig. 4.14(a) that at $\sigma'_v < 47$ MPa, the AN and SN samples exhibit greater compressibility than the RN and BN samples. Given the greater angularity and lower RD of the AN and SN samples, this behaviour is in agreement with previously reported results (e.g. Hagerty et al., 1993, Lade et al., 1996). However, at $\sigma'_v > 140$ MPa, the compressibility of the different soil types is very similar. It is hypothesised that this similarity in compressibility is due to the extensive crushing that all samples underwent (see breakage results in Table 4.2) which results in all particles acquiring more angular shapes as the test progresses.

4.3 The Limiting Compression Curves

Fig. 4.15 to Fig. 4.18 show the plots of standard deviation of the void ratios against vertical effective stress for the intermediate PSD soil types (see Appendix B for the corresponding plots of the remaining soil types). The rationale behind this plot was given in Section 3.7.2. The stress level at which the LCC begins was defined as the stress level that corresponds to the point at which the standard

deviation of the void ratio stabilise at a relatively low value. The stress level at which each of the tested soil types reaches the LCC is given in Table 4.2. Interestingly, all the tested soil types regardless of their PSD and particle shape attained the LCC within the stress range of 10 – 100 MPa suggested by Shipton and Coop (2012) for clean quartz sands.

Having determined the stress level that marks the commencement of the LCC for each of the tested soil types, the LCC was obtained by averaging the compression curves of each soil type that fell in the LCC domain, and modelled with Equation 2.2. The resulting LCCs are presented in Fig. 4.19 - Fig. 4.22 for the angular, sub-angular, rounded and beads soil types respectively, and the obtained LCC parameters (ρ_c and σ'_r) are given in Table 4.2.

As in the case of the e_{max} and e_{min}, it would be helpful to know the relationship between the two LCC parameters. Although, unlike the e_{max} and e_{min}, ρ_c and σ'_r are obtained from the same test. To examine this, the two parameters are plotted against each other for all the soil types tested in Fig. 4.23. The figure shows that there is a strong (R^2 = 0.995) positive linear correlation between ρ_c and σ'_r. The equation of the relation is given in Equation (4.2). However, it is unclear whether the observed strong correlation is affected by variation in D_{50} and particle hardness (mineralogy) since these parameters were kept constant in the present study. This needs future investigation.

$$\sigma'_r = 35.82\ (\text{MPa})\rho_c - 10.74\ (\text{MPa}) \tag{4.2}$$

4.3.1 Relationship between the LCC and compressibility

Given the strong correlation between ρ_c and σ'_r, and in order to quantify the compressibility of the soil types at the LCC state, the relationship between the LCC and the coefficient of compressibility (a_v) is expressed as follows:

Recall that;

$$\log(e) = -\rho_c \cdot \log(\sigma'/\sigma'_r) \text{ (Equation 2.2)}$$

This can be rewritten as;

$$\log(e) = \rho_c \cdot \log(\sigma'_r/\sigma') \quad (4.3)$$

$$e = (\sigma'_r/\sigma')^{\rho_c} = {\sigma'_r}^{\rho_c} . \sigma'^{-\rho_c} \quad (4.4)$$

Differentiate Equation 4.4 with respect to σ'

$$de/d\sigma' = -\rho_c . {\sigma'_r}^{\rho_c} . \sigma'^{-\rho_c-1} \quad (4.5)$$

Substitute $35.82\ (\text{MPa})\rho_c - 10.74(\text{MPa})$ for σ'_r (Equation 4.2) in Equation 4.5

$$de/d\sigma' = -\rho_c(35.82\ \rho_c - 10.74)^{\rho_c} . \sigma'^{-\rho_c-1} \quad (4.6)$$

Therefore;

$$-de/d\sigma' = \rho_c(35.82\ \rho_c - 10.74)^{\rho_c} . \sigma'^{-\rho_c-1} = a_v \text{ (Equation 4.1)} \quad (4.7)$$

Equation 4.7 is plotted against the logarithm of vertical effective stress for four values of ρ_c that span the range of measured values reported in Table 4.2. That is from 0.4 to about 0.7. As it is for the a_v, it is evident from the figure that, considering the correlation between ρ_c and σ'_r of the soil types (Fig. 4.23 and

Equation 4.2), higher ρ_c (i.e. steeper LCC) translates into a higher compressibility at the LCC state. This result indicates that there is a direct correlation between ρ_c and the coefficient of compressibility a_v at the LCC state.

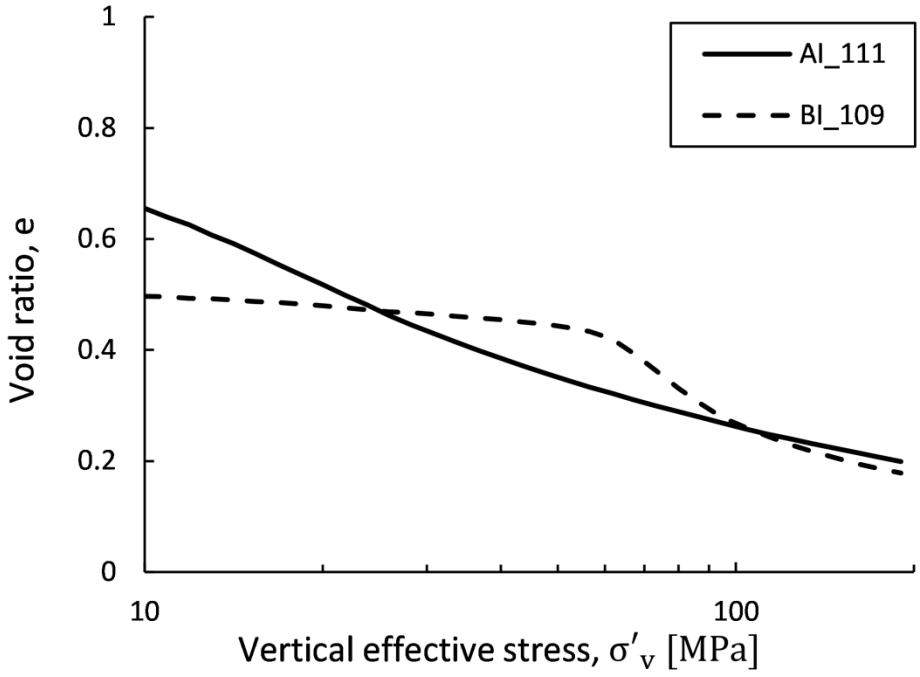
4.4 Particle Crushing

Fig. 4.25 - Fig. 4.28 show the post-compression sieve analysis results for one loose and one dense specimen for each of the intermediate PSD soil types tested (see appendix C for the corresponding plots for the other soil types). The average value of amount of particle crushing induced by compression on the specimens of each of the soil types, as quantified using Hardin (1985) breakage parameters (Fig. 3.20), are presented in Table 4.2. It can be seen from the table and from Fig. 4.29 and Fig. 4.30 that, in agreement with the typical behaviour of sand, generally, particle breakage increases with PSD uniformity and angularity of the samples' particle shape. The reason for this behaviour, according to Lade et al. (1996) is that, in uniformly graded samples, contact stress between the particles is higher due to the small number of particles surrounding each particle (low coordinate number) compared to the well-graded samples. In the well-graded samples, larger particles are cushioned by large numbers of neighbouring finer particles, thereby reducing the contact stress acting on the particle, which in turn reduces breakage. Also in the angular particle samples, contact stress tends to concentrate along the narrow dimension of the particles, thus crushing them more easily compared to the less angular particles.

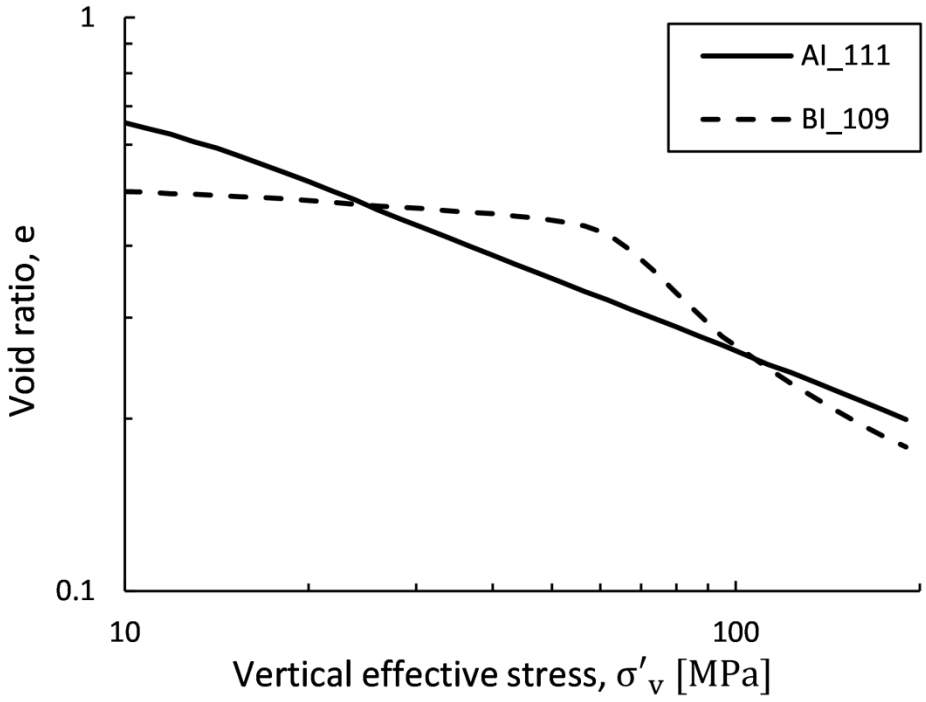
4.5 Compression Mould Lateral Deformations

The maximum lateral expansion of the mould under the maximum applied pressure (190 MPa), as it can be seen from Table 4.1, is 0.022 mm. This is equal to 0.07 % when expressed as a percentage of the original diameter of the mould. This expansion is greater than the limit of 0.03 % specified in ASTM D2435, but it is less than 0.33 % reported by Yamamuro et al. (1996) in their study. The fact that the measured lateral strains are of the same order of magnitude than those specified by ASTM D2435 for lower stress levels, and that they compare favourably to the lateral strains reported by Yamamuro et al. (1996), suggests that the compression mould performed adequately.

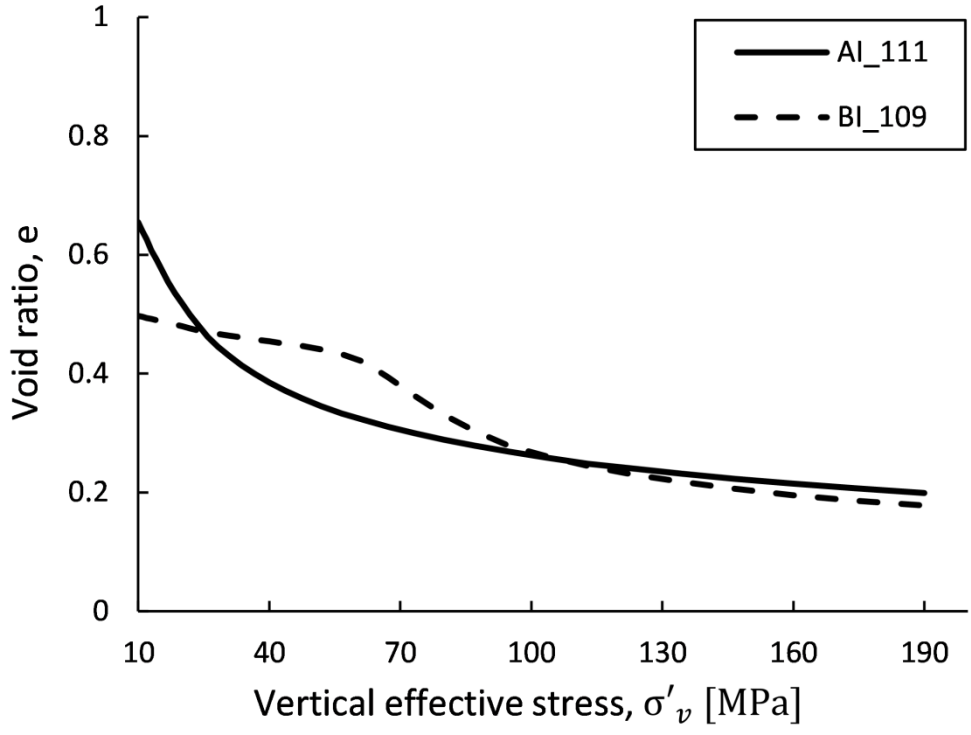
4.6 Figures and Tables



(a)



(b)



(c)

Fig. 4.1 Typical 1-D confined compression curves of the tested soil types in: (a) semi-logarithmic space; (b) double-logarithmic space; (c) natural space.

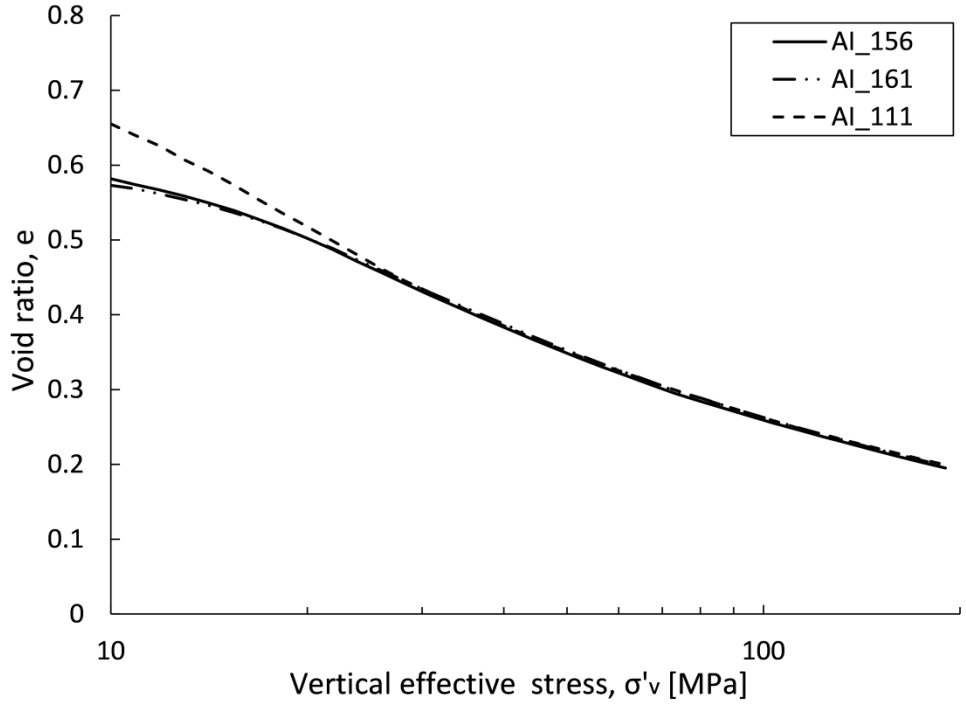


Fig. 4.2 AI soil type 1-D compression curves.

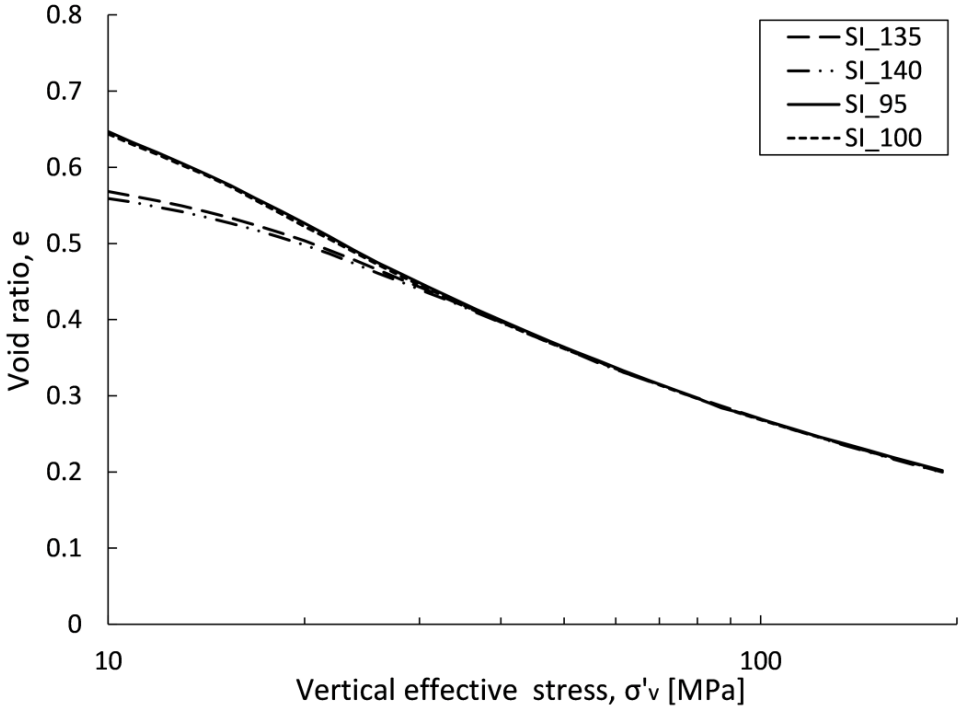


Fig. 4.3 SI soil type 1-D compression curves.

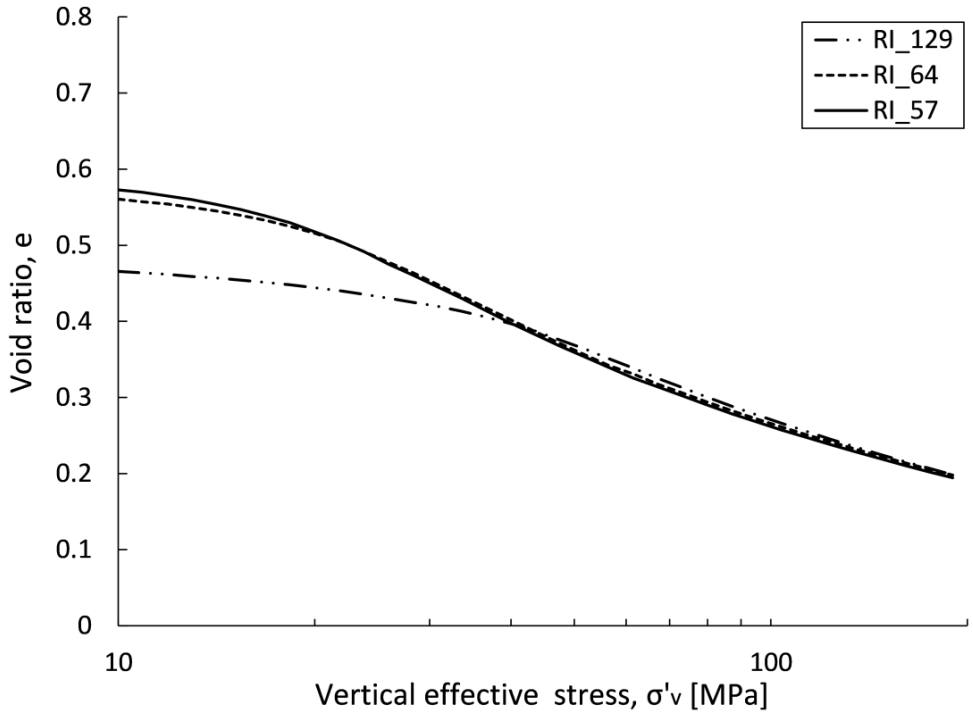


Fig. 4.4 RI soil type 1-D compression curves.

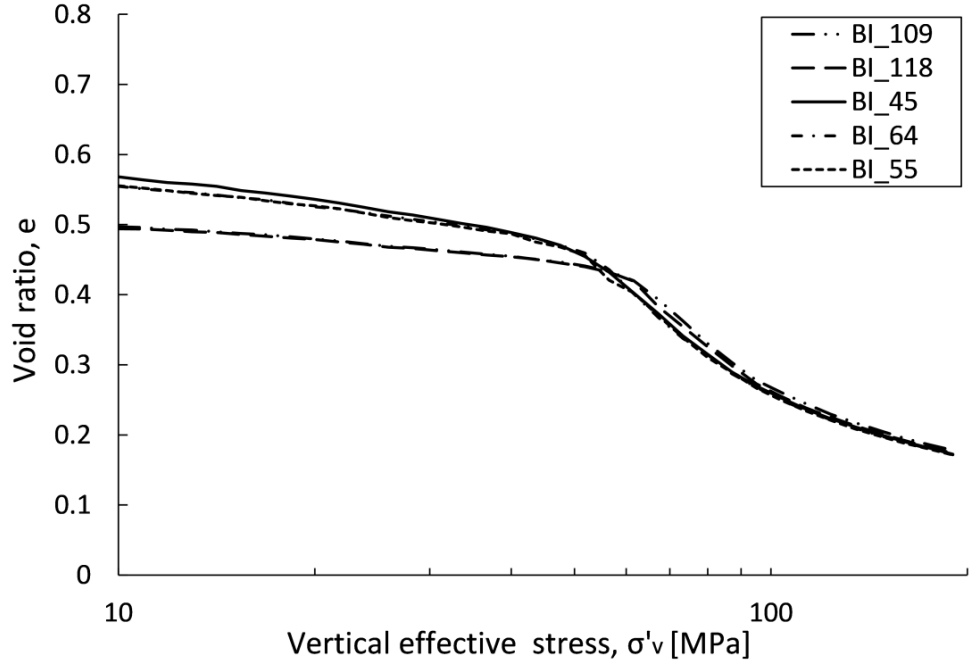


Fig. 4.5 BI soil type 1-D compression curves.

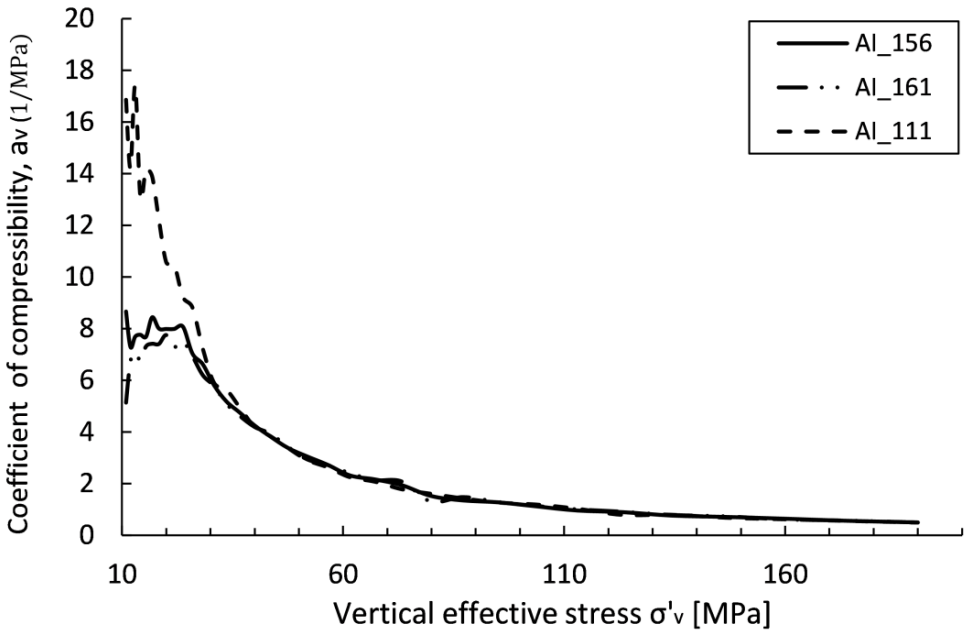


Fig. 4.6 Effect of initial relative density on compressibility for the AI soil type.

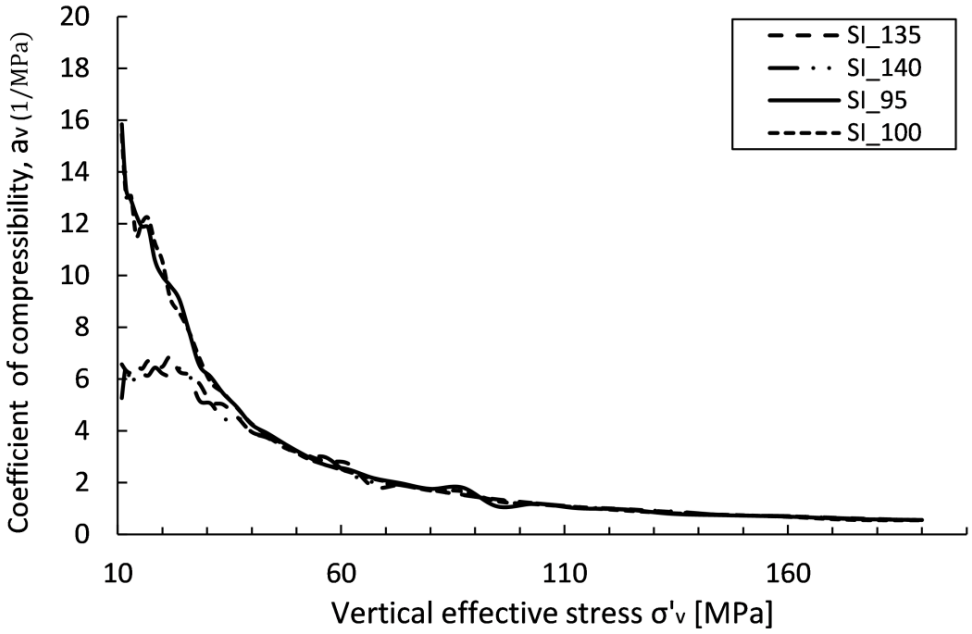


Fig. 4.7 Effect of initial relative density on compressibility for the SI soil type.

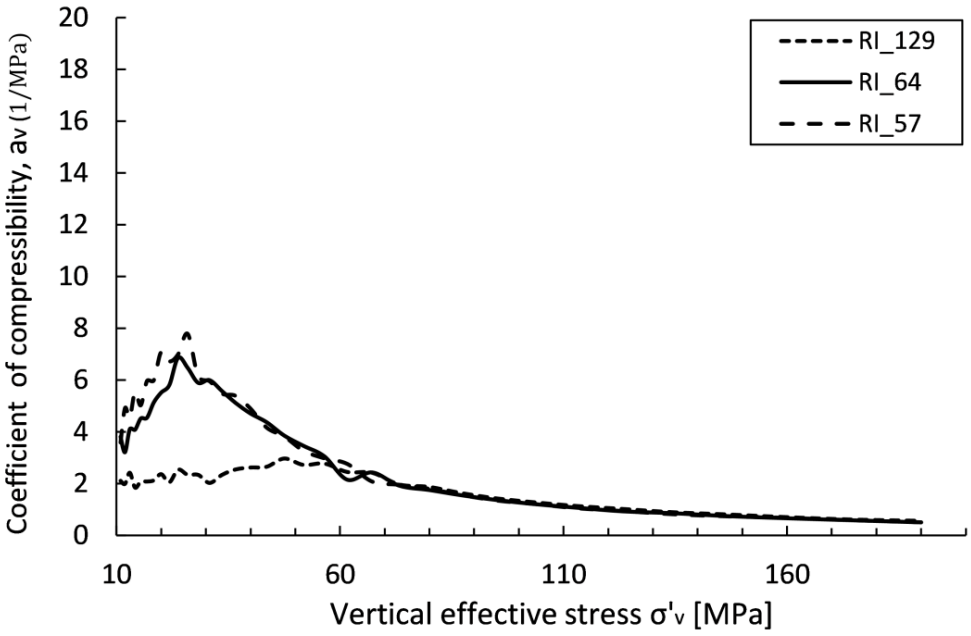


Fig. 4.8 Effect of initial relative density on compressibility for the RI soil type.

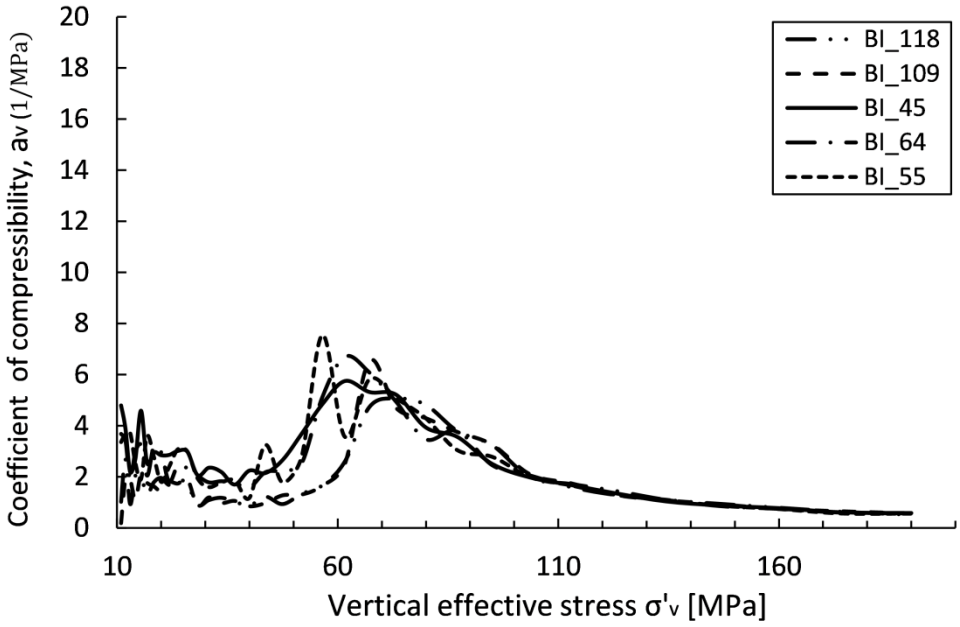
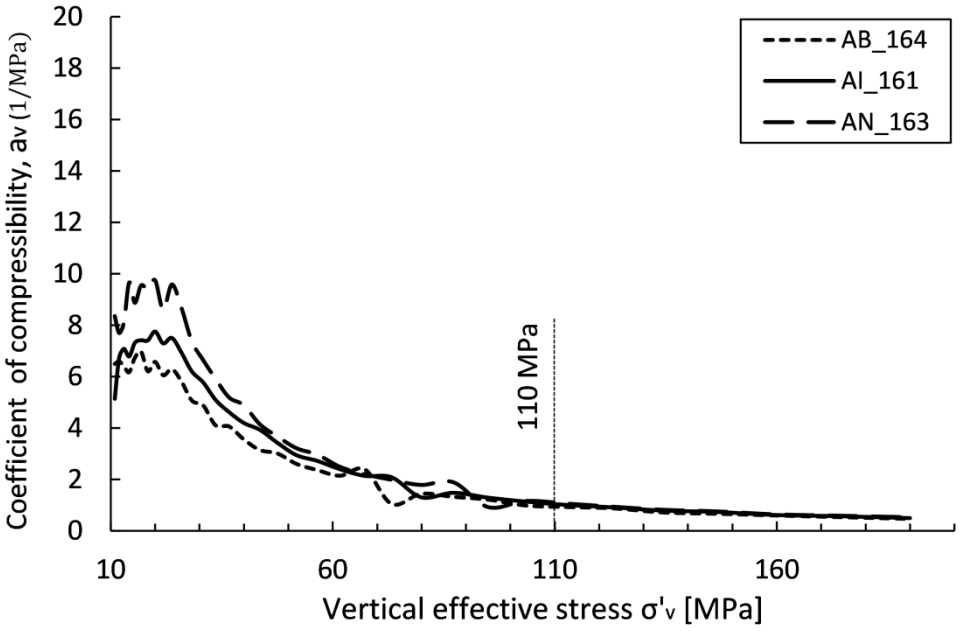
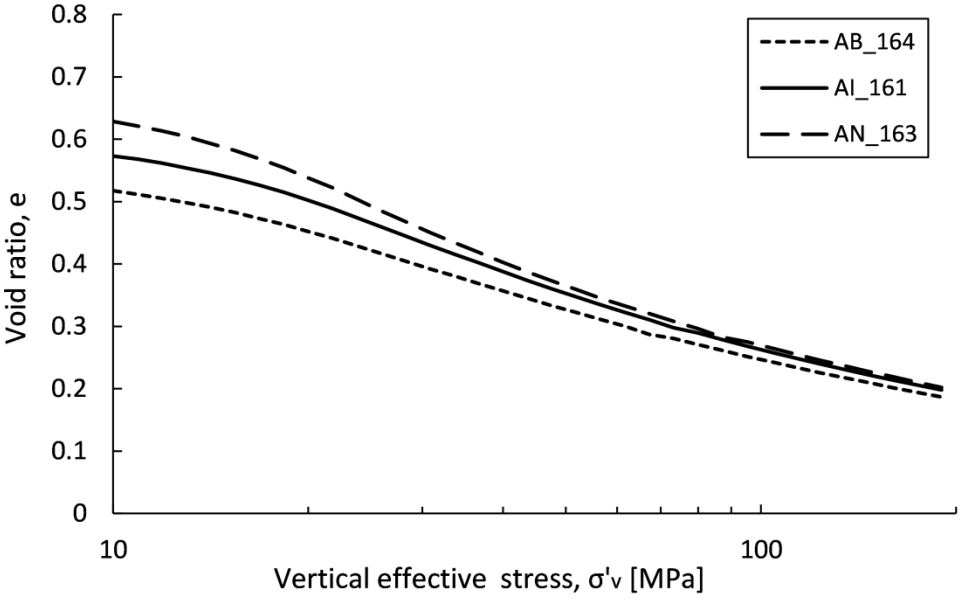


Fig. 4.9 Effect of initial relative density on compressibility for the BI soil type.

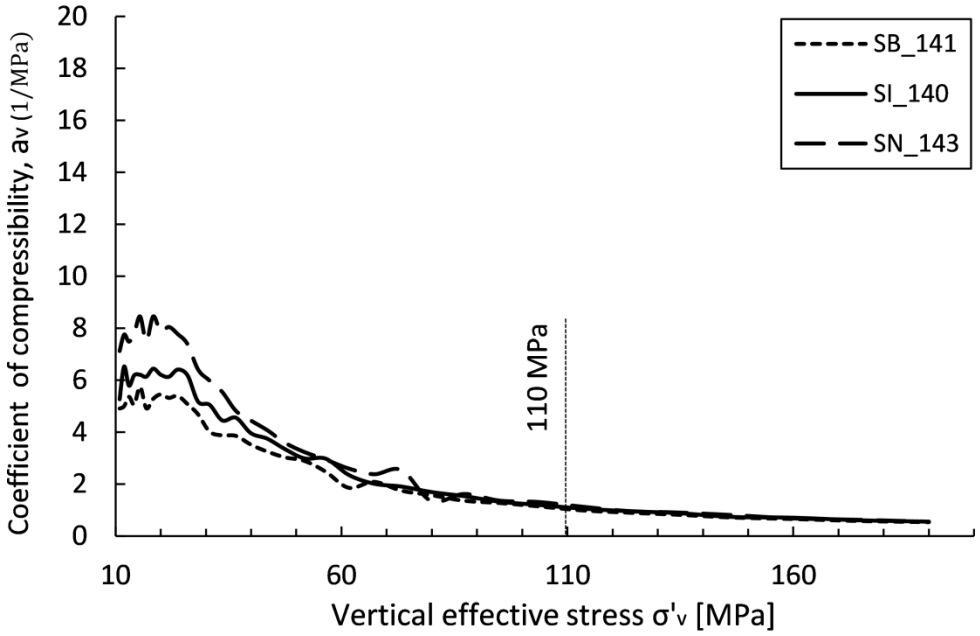


(a)

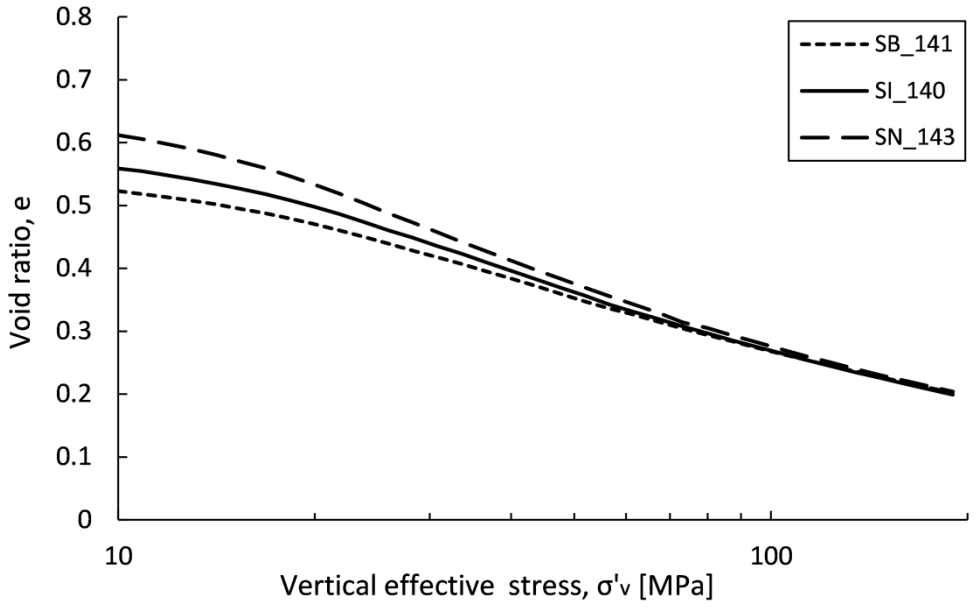


(b)

Fig. 4.10 Effect of PSD on compressibility for the angular soil types.

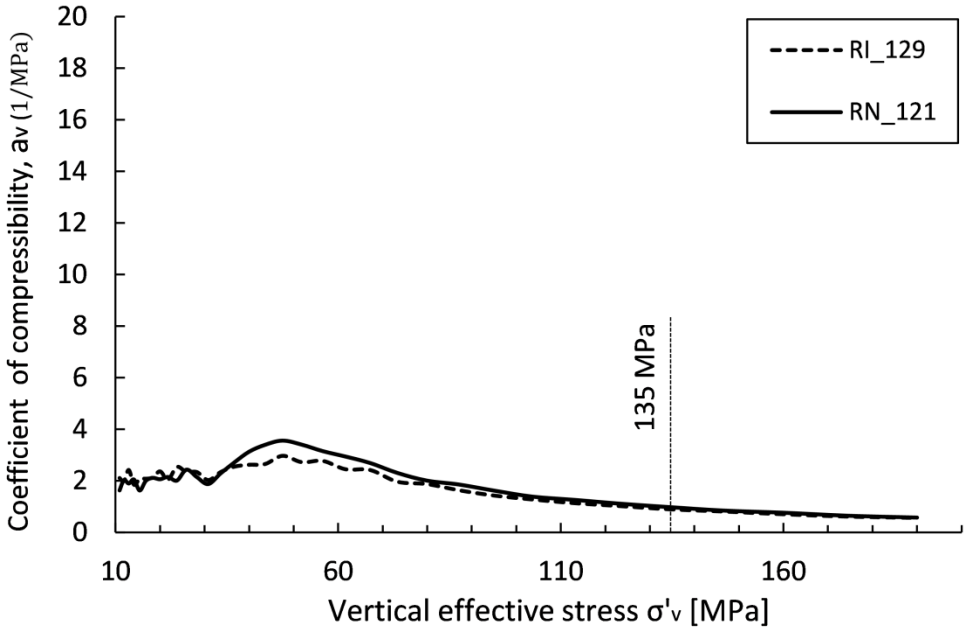


(a)

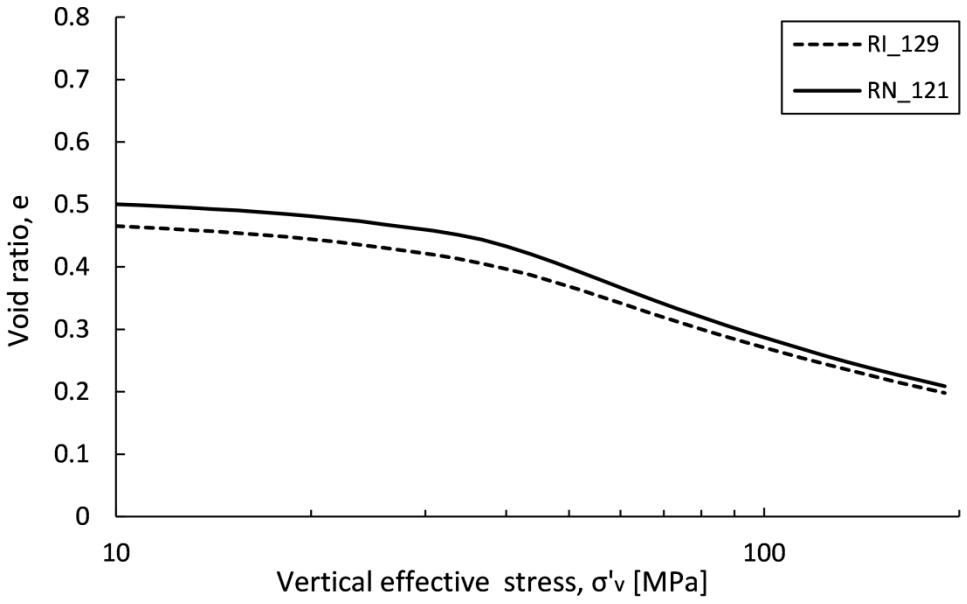


(b)

Fig. 4.11 Effect of PSD on compressibility for the sub-angular soil types.

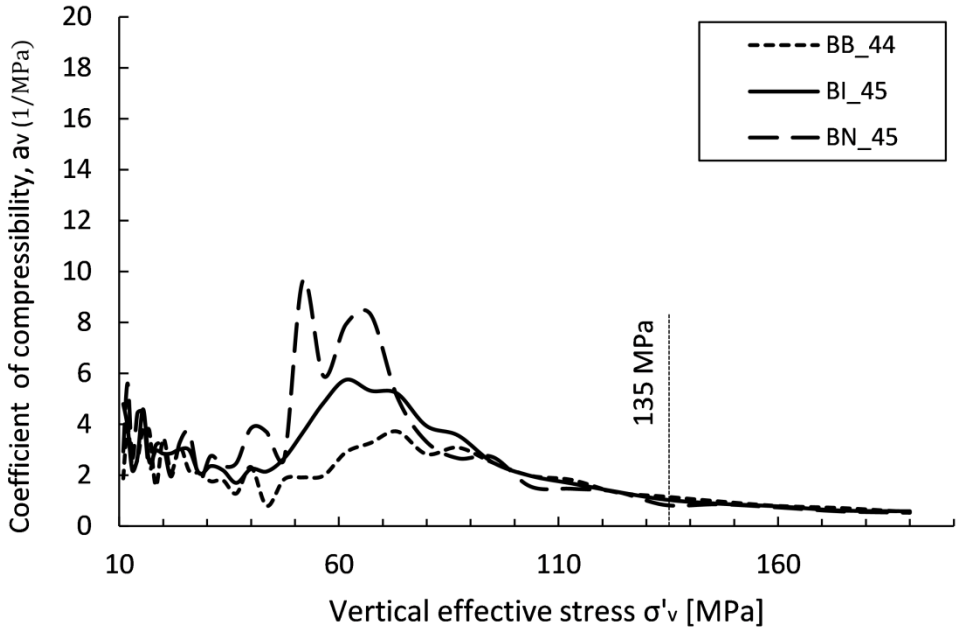


(a)

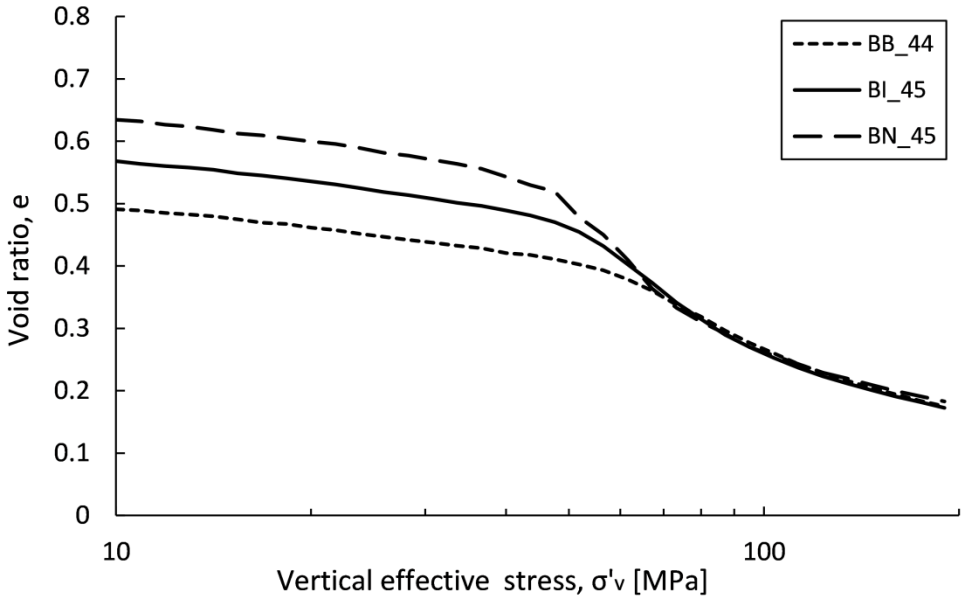


(b)

Fig. 4.12 Effect of PSD on compressibility for the rounded soil types.

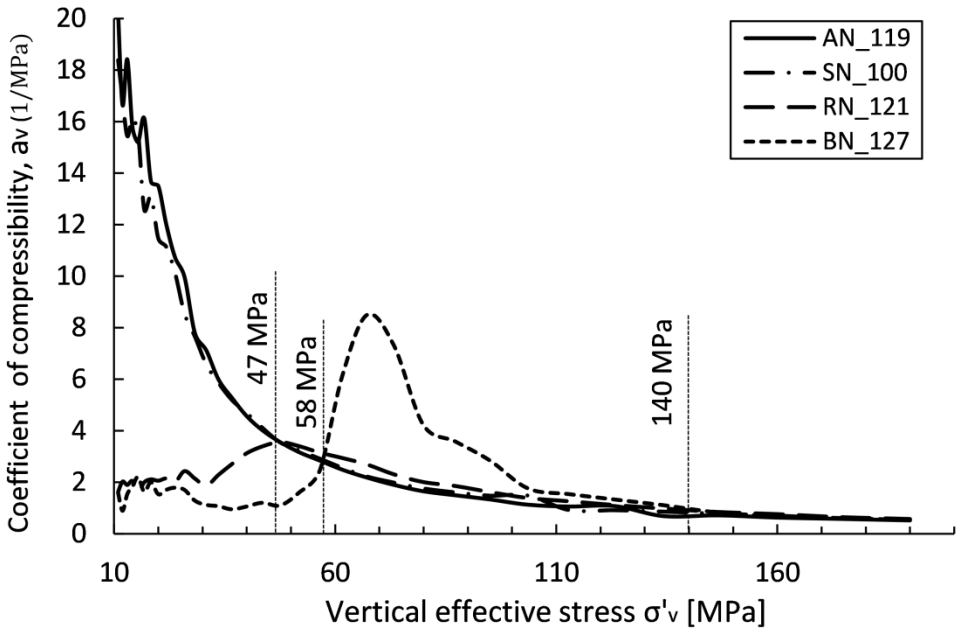


(a)

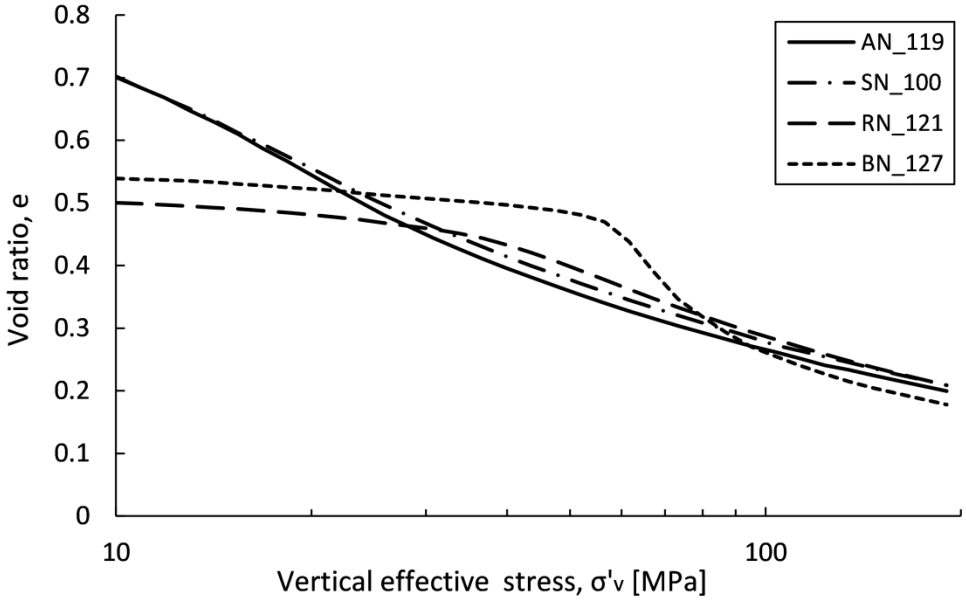


(b)

Fig. 4.13 Effect of PSD on compressibility for the beads soil types.



(a)



(b)

Fig. 4.14 Effect of particle shapes on compressibility.

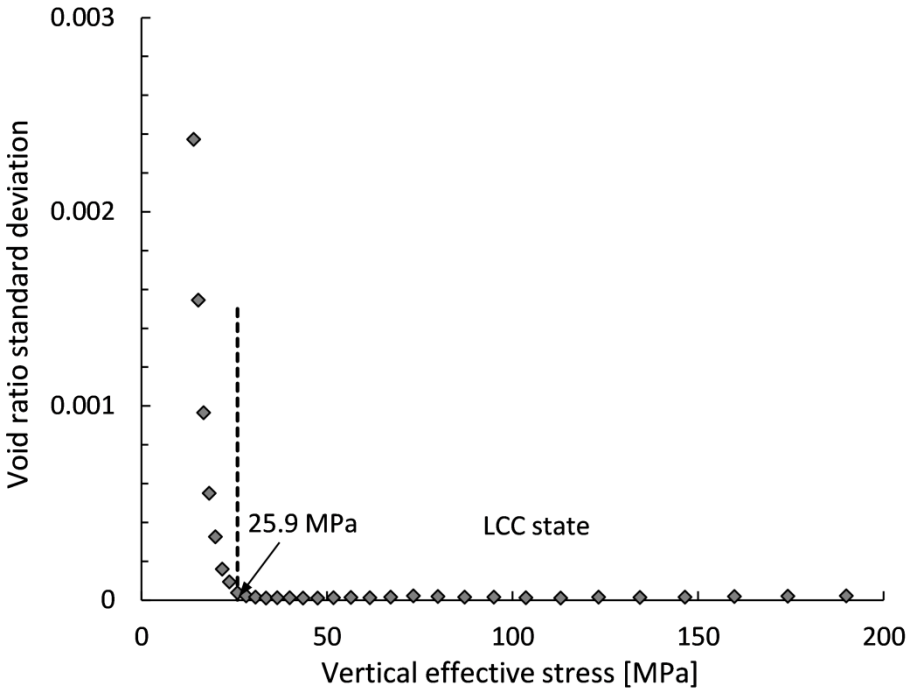


Fig. 4.15 LCC determination for the AI soil type.

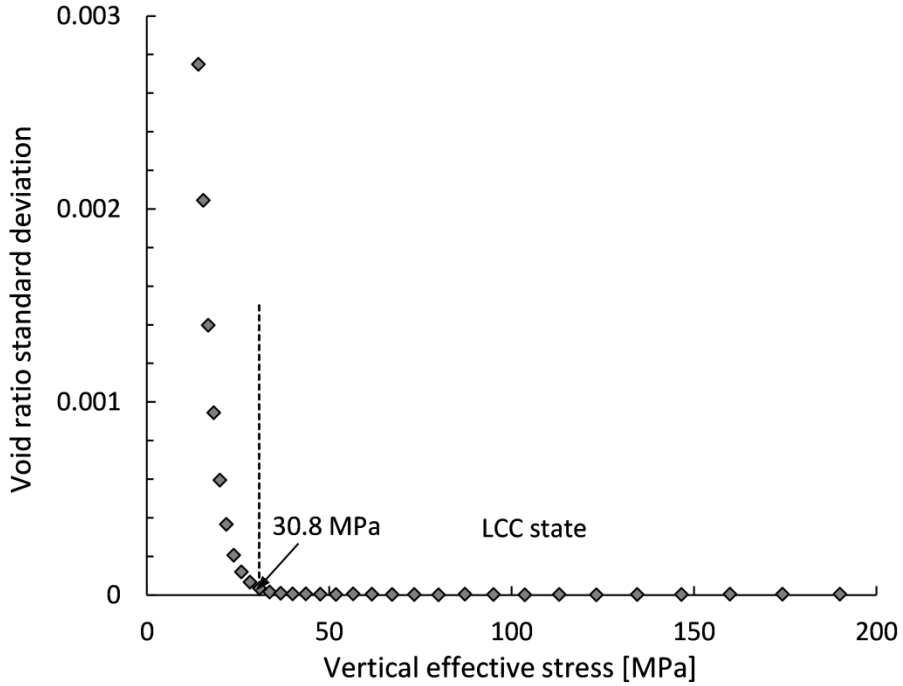


Fig. 4.16 LCC determination for the SI soil type.

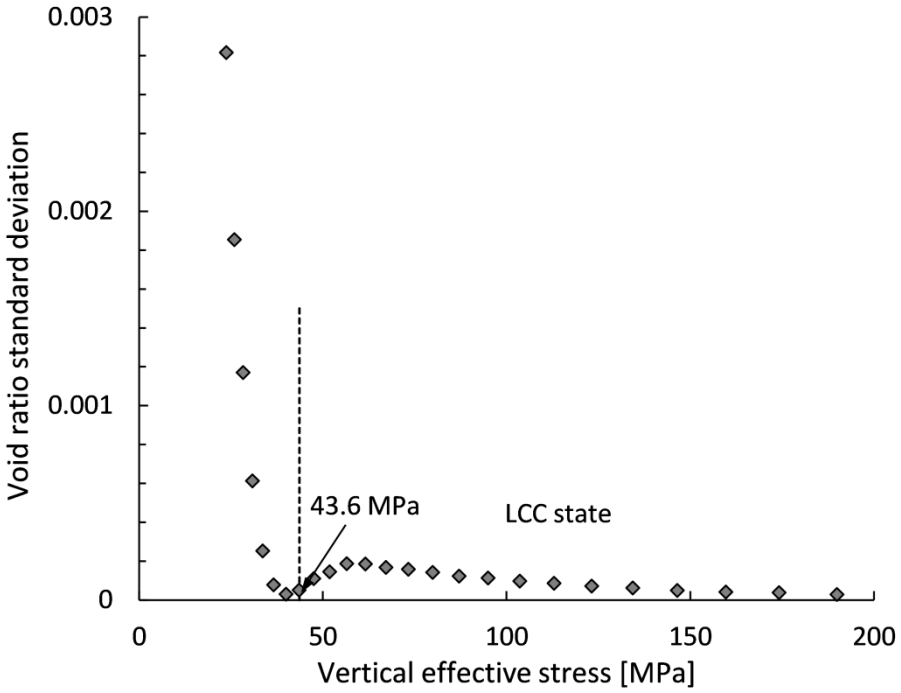


Fig. 4.17 LCC determination for the RI soil type.

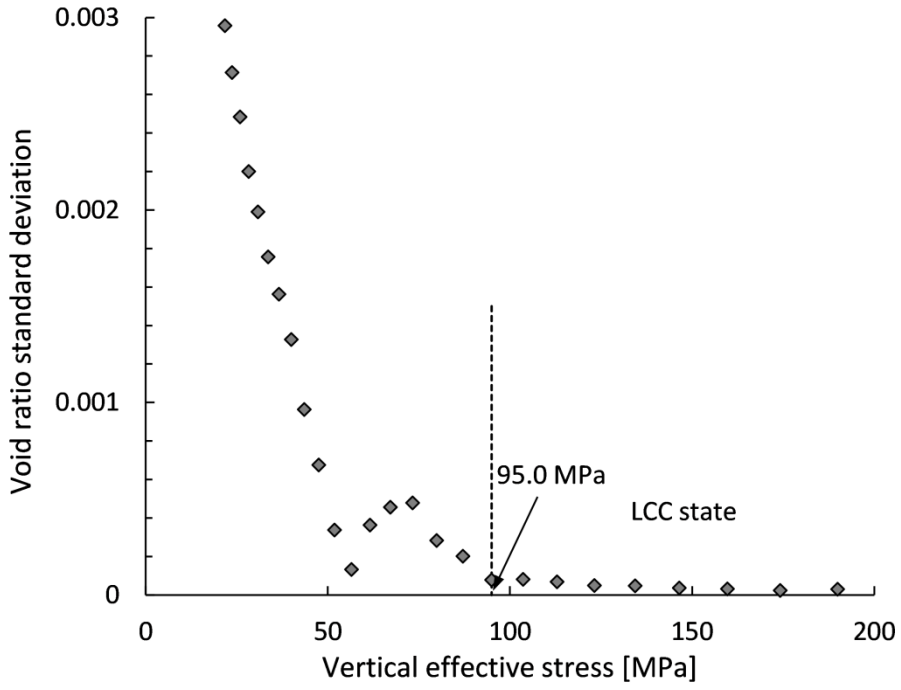


Fig. 4.18 LCC determination for the BI soil type.

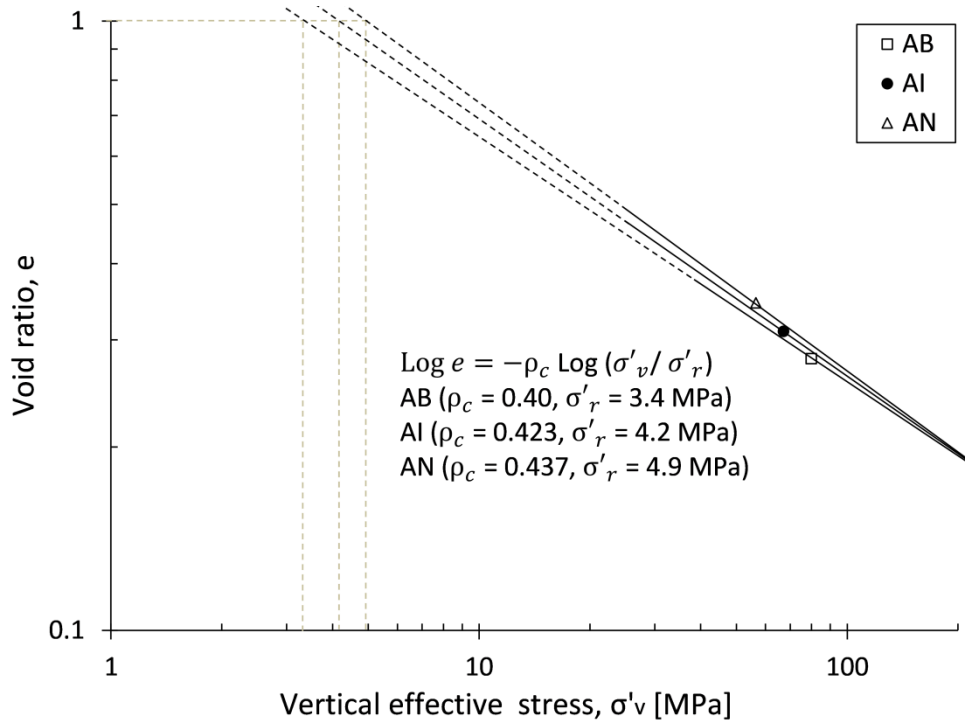


Fig. 4.19 Limiting compression curves of the angular soil types.

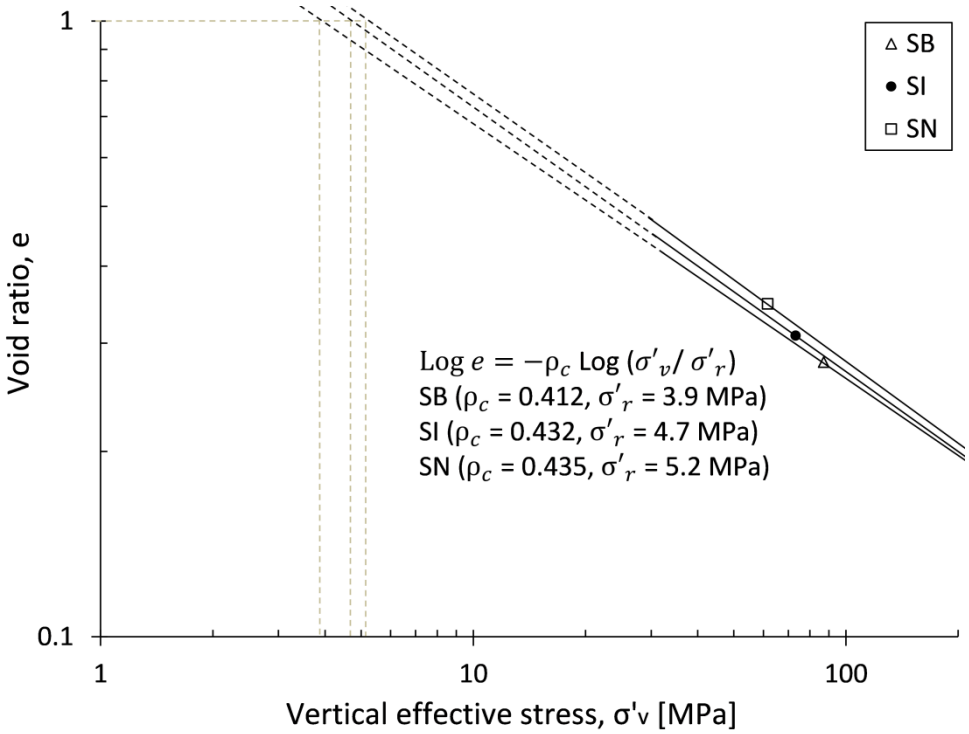


Fig. 4.20 Limiting compression curves of the sub-angular soil types.

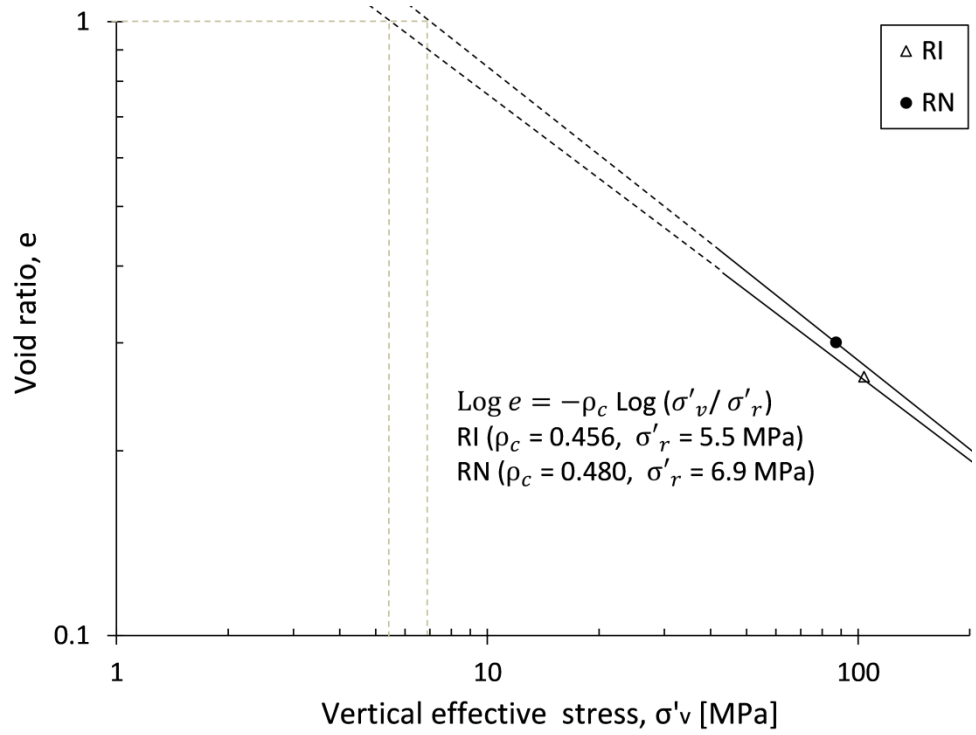


Fig. 4.21 Limiting compression curves of the rounded soil types.

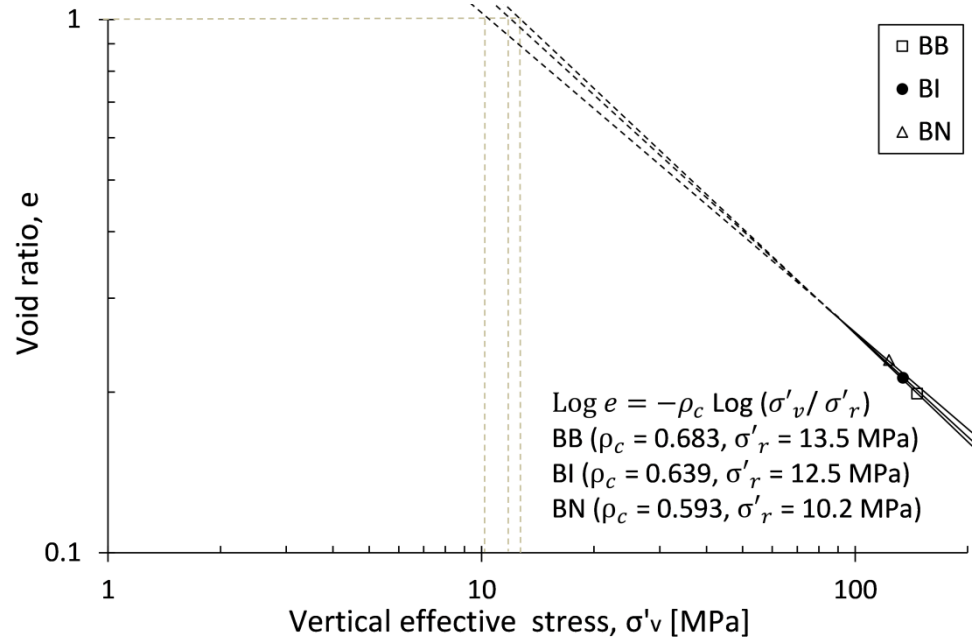


Fig. 4.22 Limiting compression curves of the beads soil types.

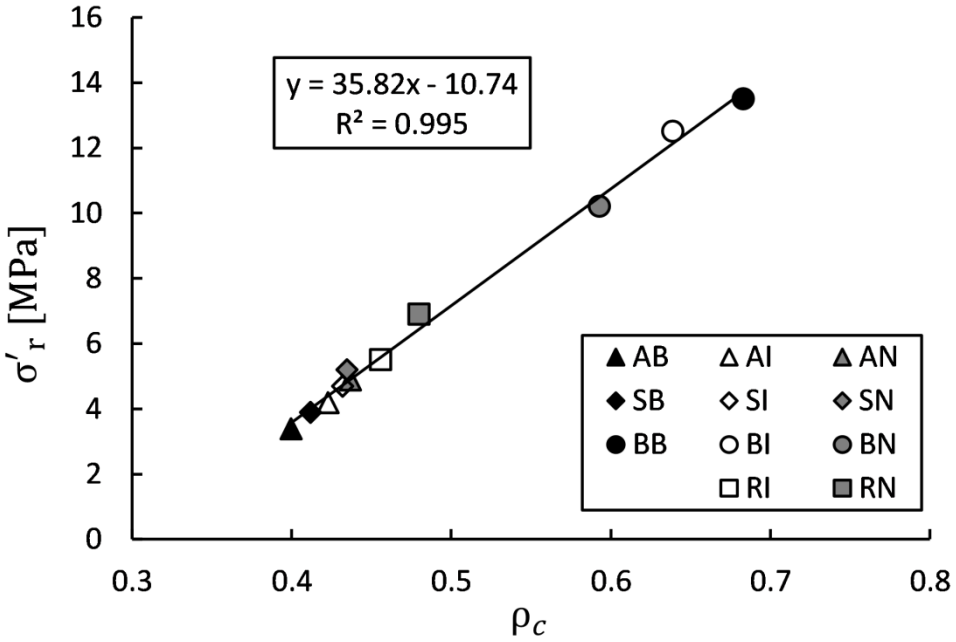


Fig. 4.23 Relationship between the LCC parameters.

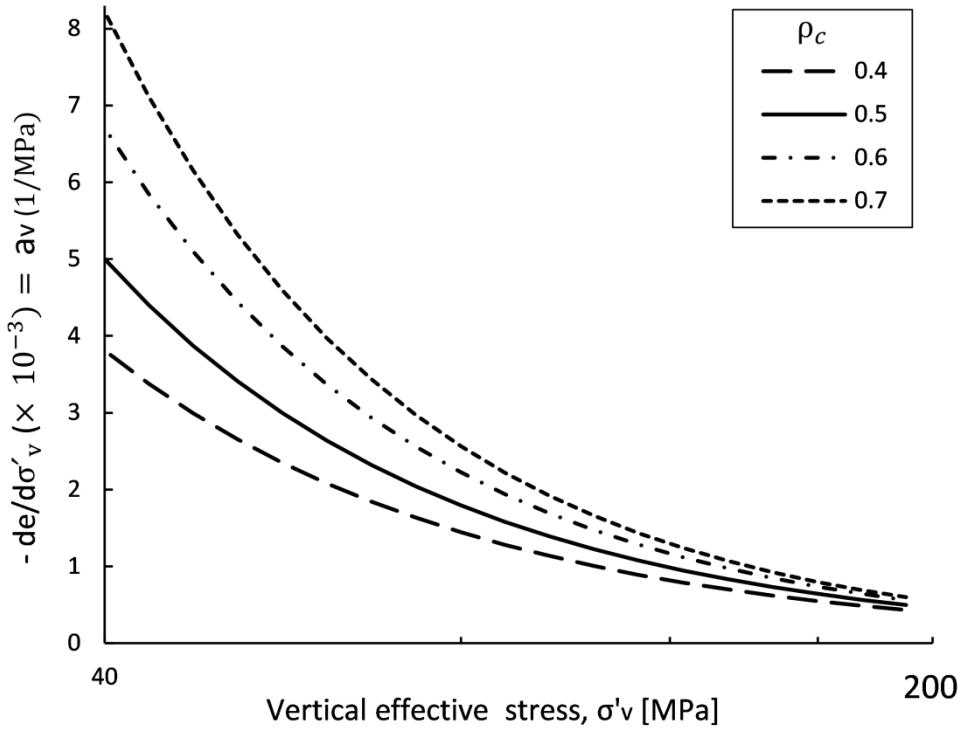


Fig. 4.24 Relationship between the LCC and compressibility.

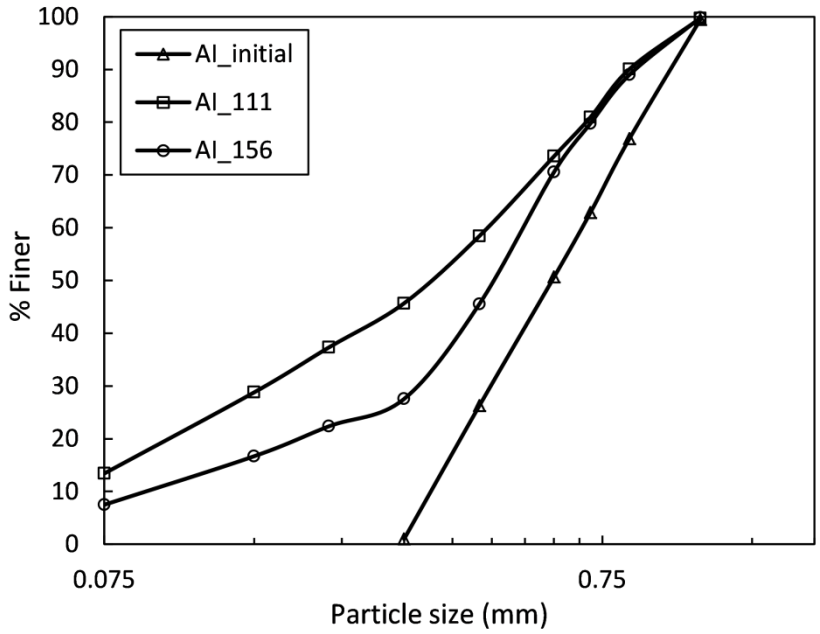


Fig. 4.25 Pre and post-compression PSD curves of the AI soil type.

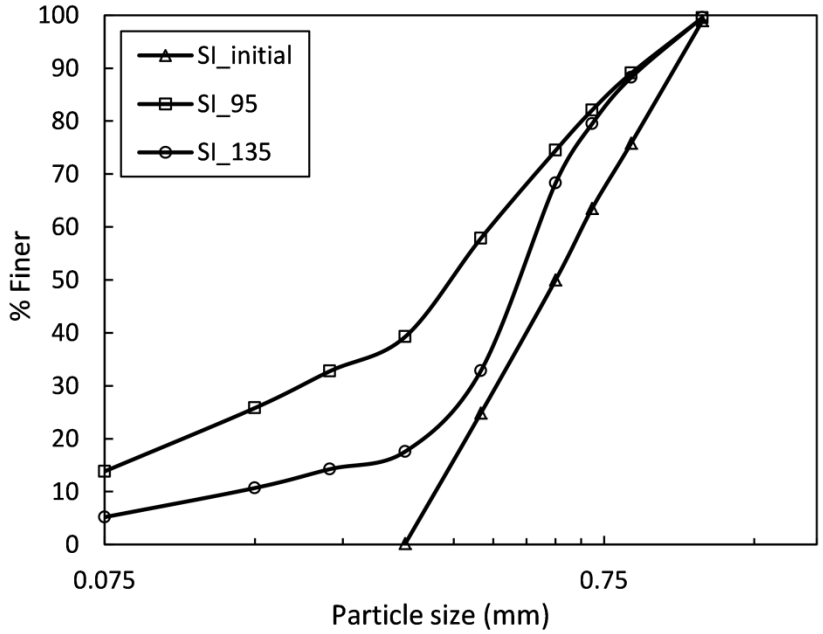


Fig. 4.26 Pre and post-compression PSD curves of the SI soil type.

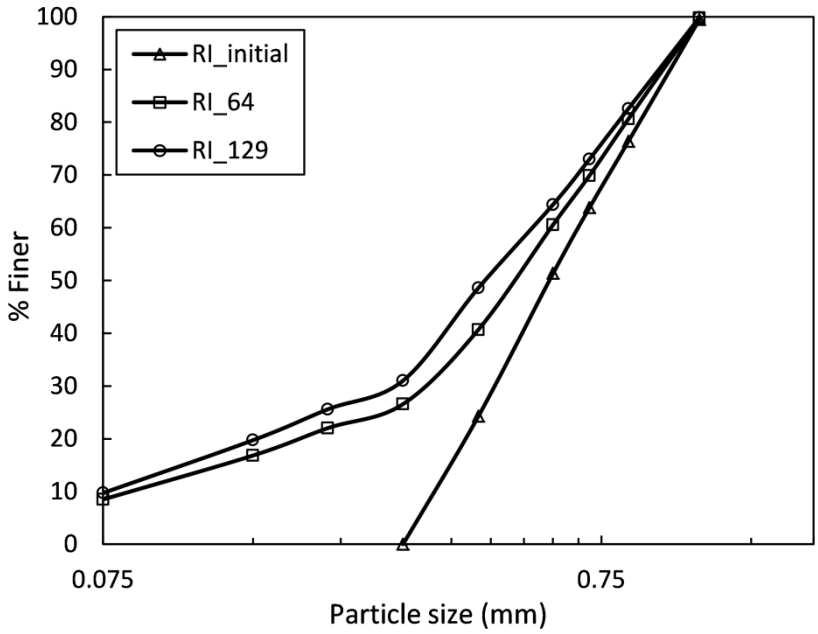


Fig. 4.27 Pre and post-compression PSD curves of the RI soil type.

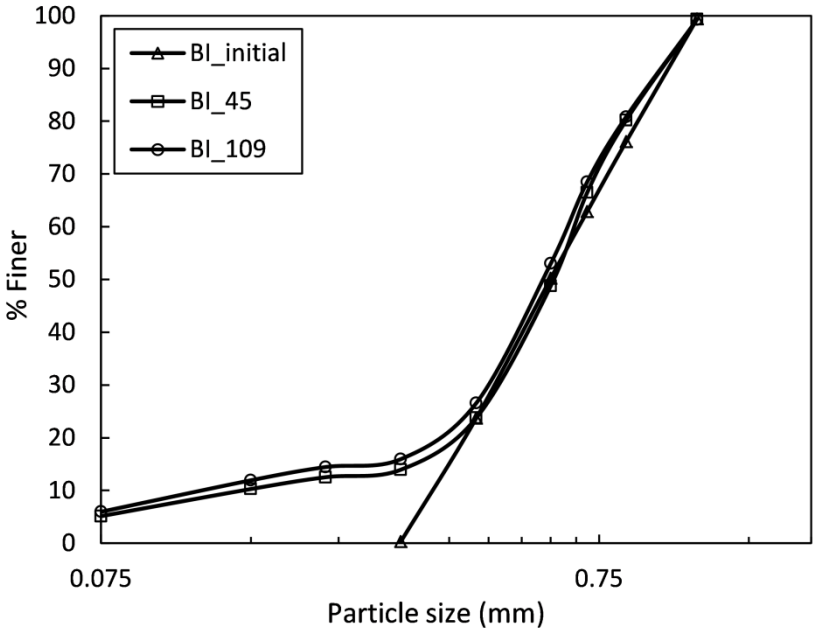


Fig. 4.28 Pre and post-compression PSD curves of the BI soil type.

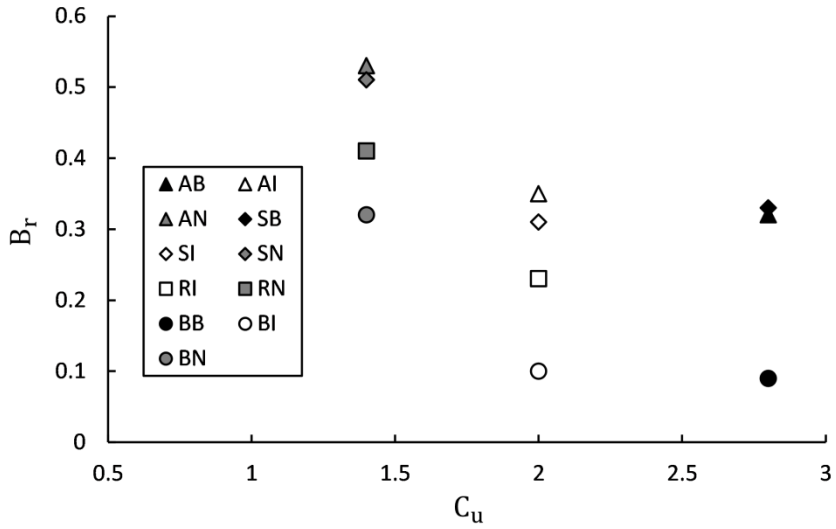


Fig. 4.29 Effect of PSD on particle breakage.

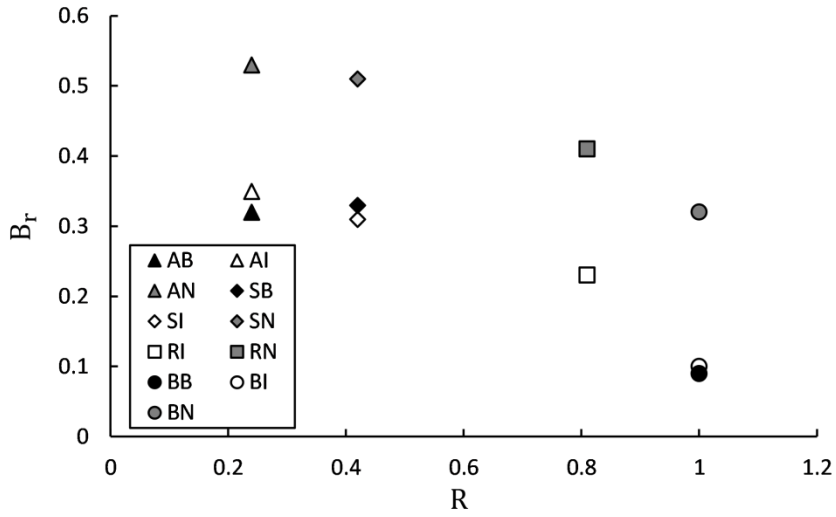


Fig. 4.30 Effect of particles roundness on particle breakage.

Table 4.1 1-D confined compression testing program summary.

S/N	Specimen identifier	Particle shape	PSD type	Set-up void ratio (*e* before loading)	*e* @10 MPa	Relative density, D_r (%) @10 MPa	Final *e* @190 MPa	Lateral expansion (mm) @190 MPa	Max. lateral expansion of mould (%)
1	AB_164	Angular	Broad	0.64	0.52	164	0.19	unreliable	not available
2	AB_150			0.66	0.54	150	0.20	0.007	0.02
3	AB_121			0.88	0.58	121	0.19	not measured	not available
4	AB_114			0.88	0.59	114	0.20	not measured	not available
5	AB_114			0.85	0.59	114	0.21	not measured	not available
6	AI_156		Inter	0.73	0.58	156	0.20	0.004	0.01
7	AI_161			0.70	0.57	161	0.20	0.002	0.01
8	AI_111			0.95	0.66	111	0.20	not measured	not available
9	AI_111			0.95	0.66	111	0.20	not measured	not available
10	AI_111			0.96	0.66	111	0.20	not measured	not available
11	AN_156		Narrow	0.80	0.64	156	0.20	0.005	0.02
12	AN_163			0.77	0.63	163	0.20	0.008	0.03
13	AN_113			1.01	0.71	113	0.20	not measured	not available
14	AN_106			1.02	0.72	106	0.21	not measured	not available
15	AN_119			1.01	0.7	119	0.20	not measured	not available
16	SB_141	Sub	Broad	0.64	0.52	141	0.20	unreliable	not available
17	SB_147			0.62	0.51	147	0.20	0.003	0.01

S/N	Specimen identifier	Particle shape	PSD type	Set-up void ratio (*e* before loading)	*e* @10 MPa	Relative density, D_r (%) @10 MPa	Final *e* @190 MPa	Lateral expansion (mm) @190 MPa	Max. lateral expansion of mould (%)
18	SB_94	Sub	Broad	0.86	0.6	94	0.21	0.004	0.01
19	SB_106			0.84	0.58	106	0.19	unreliable	not available
20	SI_135		Inter	0.69	0.57	135	0.20	0.01	0.03
21	SI_140			0.67	0.56	140	0.20	0.003	0.01
22	SI_95			0.95	0.65	95	0.20	0.003	0.01
23	SI_100			0.94	0.64	100	0.20	0.008	0.03
24	SN_143		Narrow	0.75	0.61	143	0.20	0.011	0.03
25	SN_138			0.76	0.62	138	0.21	unreliable	not available
26	SN_100			1.01	0.7	100	0.21	unreliable	not available
27	SN_95			1.02	0.71	95	0.22	unreliable	not available
28	RI_129	Round	Inter	0.55	0.47	129	0.20	0.007	0.02
29	RI_129			0.55	0.47	129	0.20	0.005	0.02
30	RI_64			0.72	0.56	64	0.20	0.014	0.04
31	RI_57			0.72	0.57	57	0.19	0.022	0.07
32	RN_121		Narrow	0.59	0.5	121	0.21	0.005	0.02
33	RN_121			0.58	0.5	121	0.21	unreliable	not available
34	RN_36			0.77	0.62	36	0.20	0.015	0.05
35	RN_29			0.77	0.63	29	0.20	unreliable	not available
36	BB_122			0.56	0.42	122	0.16	unreliable	not available

S/N	Specimen identifier	Particle shape	PSD type	Set-up void ratio (*e* before loading)	*e* @10 MPa	Relative density, D_r (%) @10 MPa	Final *e* @190 MPa	Lateral expansion (mm) @190 MPa	Max. lateral expansion of mould (%)
37	BB_122	Beads	Broad	0.57	0.42	122	0.17	0.004	0.01
38	BB_56			0.64	0.48	56	0.17	not measured	not available
39	BB_44		Broad	0.64	0.49	44	0.18	not measured	not available
40	BB_44			0.64	0.49	44	0.18	not measured	not available
41	BI_109		Inter	0.65	0.5	109	0.18	0.005	0.02
42	BI_118			0.64	0.49	118	0.17	unreliable	not available
43	BI_45			0.73	0.57	45	0.17	not measured	not available
44	BI_64			0.73	0.55	64	0.17	not measured	not available
45	BI_55			0.73	0.56	55	0.17	not measured	not available
46	BN_127		Narrow	0.70	0.54	127	0.18	0.018	0.06
47	BN_127			0.69	0.54	127	0.18	0.011	0.03
48	BN_45			0.80	0.63	45	0.18	not measured	not available
49	BN_36			0.79	0.64	36	0.19	not measured	not available
50	BN_45			0.79	0.63	45	0.18	not measured	not available

Table 4.2 The LCC and particle breakage characteristics of the tested soil types.

Soil type	ρ_c	σ'_r [MPa]	$\sigma'_{v@LCC}$ [MPa]	Relative breakage, B_r	C_u	R	e_{max}	e_{min}
AB	0.40	3.4	40.0	0.32	2.8	0.24	0.75	0.61
AI	0.423	4.2	25.9	0.35	2.0	0.24	0.86	0.68
AN	0.437	4.9	23.8	0.53	1.4	0.24	0.89	0.73
SB	0.412	3.9	33.6	0.33	2.8	0.42	0.76	0.59
SI	0.432	4.7	30.8	0.31	2.0	0.42	0.84	0.64
SN	0.435	5.2	30.8	0.51	1.4	0.42	0.91	0.70
RI	0.456	5.5	43.6	0.23	2.0	0.78	0.65	0.51
RN	0.480	6.9	43.6	0.41	1.4	0.78	0.67	0.53
BB	0.683	13.5	95.0	0.09	2.8	1	0.53	0.44
BI	0.639	12.5	95.0	0.1	2.0	1	0.62	0.51
BN	0.593	10.2	87.1	0.32	1.4	1	0.68	0.57

5 CORRELATION BETWEEN THE LCC PARAMETERS AND PSD, PARTICLE SHAPE AND LIMIT VOID RATIOS

5.1 Introduction

The experimental results presented in previous chapters (as summarized in Table 4.2) are discussed in this chapter. This is done to investigate the correlations between the LCC parameters and PSD, particle shape and limit void ratios (e_{max} and e_{min}).

5.2 Correlation between the LCC parameters and PSD

In order to investigate the relationship between the LCC and PSD, C_u is plotted against ρ_c and σ'_r (Table 4.2) in Fig. 5.1 and Fig. 5.2 respectively. It can be seen from the figures that the values of both ρ_c and σ'_r decrease approximately linearly with increase in C_u for all the granular materials tested except for the beads samples where the opposite is the case. The reason for the atypical behaviour of the beads samples might be because of the idealized geometry of their particles, which permits easy sliding and rolling of the particles under compression. As a result of less friction generated among the particles (as they rearrange their orientation), they were able to form a tighter packing fabric. Consequently, the effect of initial formation densities was eliminated, which results in the emergence of the LCCs with a lesser particle breakage (Table 4.2) when compared with the samples of the natural sands of the same PSD. For instance, the B_r value of the BI soil type is 0.1 which is lower than 0.23, 0.31 and 0.35 for the RI, SI and AI soil types, respectively. Although one would expect the

beads to have the highest B_r because they have the lowest particle hardness (Table 3.2) of the four different sources of granular materials tested.

However, Figs. 5.1 and 5.2 show (for the natural sands) that the more uniform the PSD, the steeper the LCC, which means the more compressible is the sample (Fig. 4.24). This observation is in agreement with the results of previous investigators such as Altuhafi and Coop (2011), Roberts and De Souza (1958) and Roberts (1964). It is also consistent with the result presented in Fig. 4.10 - Fig. 4.13 which showed that compressibility increases with PSD's uniformity, for soil types of a given particle shape. This observed trend implies that, at the LCC state, compressibility of non-plastic sands increases with PSD's uniformity.

5.3 Correlation between the LCC parameters and Particle shape

Fig. 5.3 and Fig. 5.4 depict the influence of particle shape on the LCC. In the figures particle roundness are plotted against ρ_c (Fig. 5.3) and σ'_r (Fig. 5.4) for all the tested soil types. It can be seen from the figures that there is a systematic non-linear relationship between the LCC parameters and particle shape. Both ρ'_c and σ'_r increase with particle roundness for a given PSD of the tested granular materials. This observation signifies that the LCC becomes steeper (ρ'_c increases) with increase in particle roundness, which is in agreement with the result of Cavarretta et al. (2010). Accordingly, although the compressibility of the angular soils is greater than the compressibility of rounded soils at $\sigma'_v < 47$ MPa (e.g. Fig. 4.14a), this trend is reversed when the soils reach the LCC (Fig. 5.3).

5.4 Correlation between the LCC parameters and the e_{max} and e_{min}

The correlation between the LCC and the reference void ratios is explored in Fig. 5.5 through Fig. 5.8. In Fig. 5.5 and Fig. 5.6, ρ_c is plotted against e_{max} and e_{min} respectively, while Fig. 5.7 and Fig. 5.8 present the same plots for σ'_r. The figures show that, there is a relative weak positive correlation between the LCC parameters and e_{max} and e_{min} for each of the natural sands, while the beads on the other hand suggest the opposite. Nonetheless, the result is insightful; it may be interpreted in terms of compressibility at the LCC state that, for samples of a given natural sand, the higher the e_{max} and e_{min} of a sample, the more compressible it is.

5.5 Figures

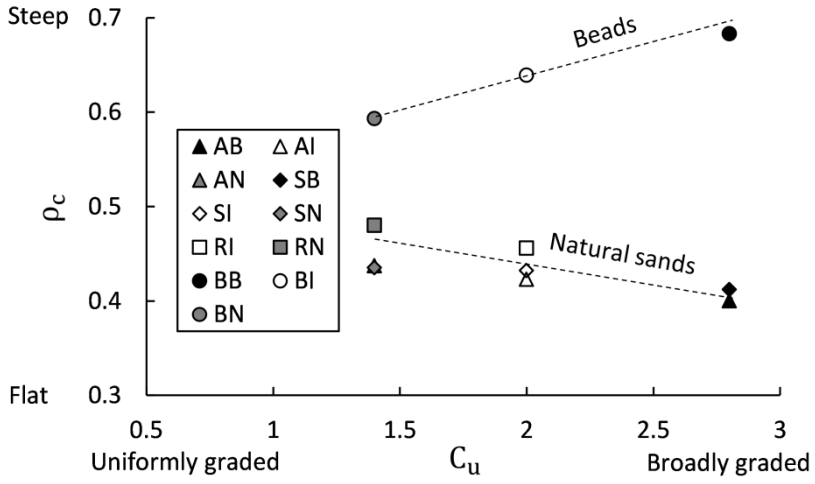


Fig. 5.1 Relationship between ρ_c and C_u.

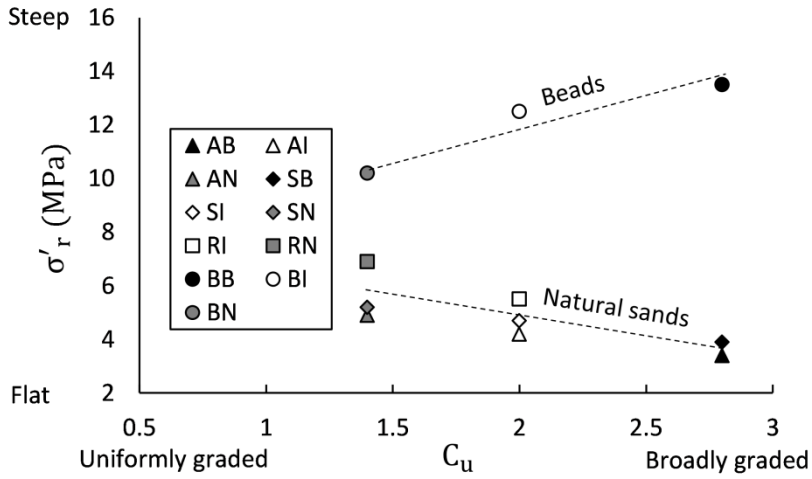


Fig. 5.2 Relationship between σ'_r and C_u.

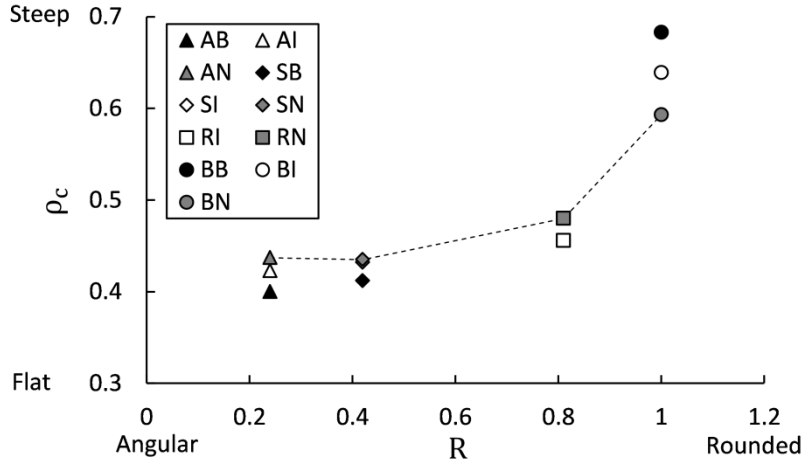


Fig. 5.3 Relationship between ρ_c and particle roundness.

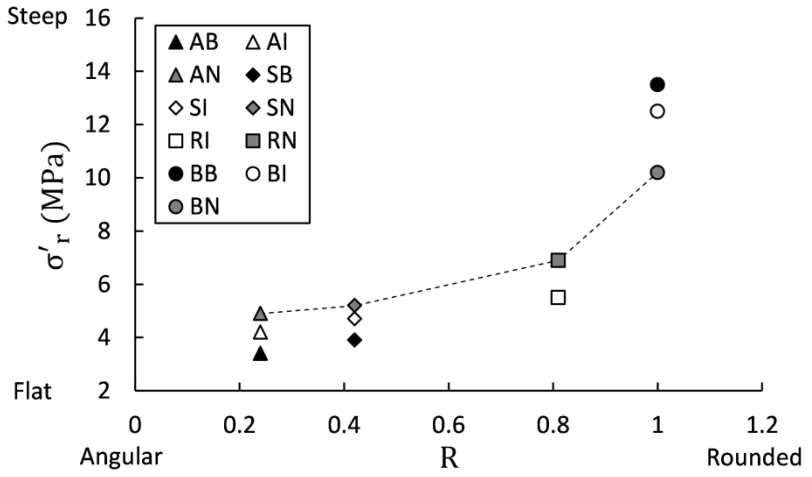


Fig. 5.4 Relationship between σ'_r and particle roundness.

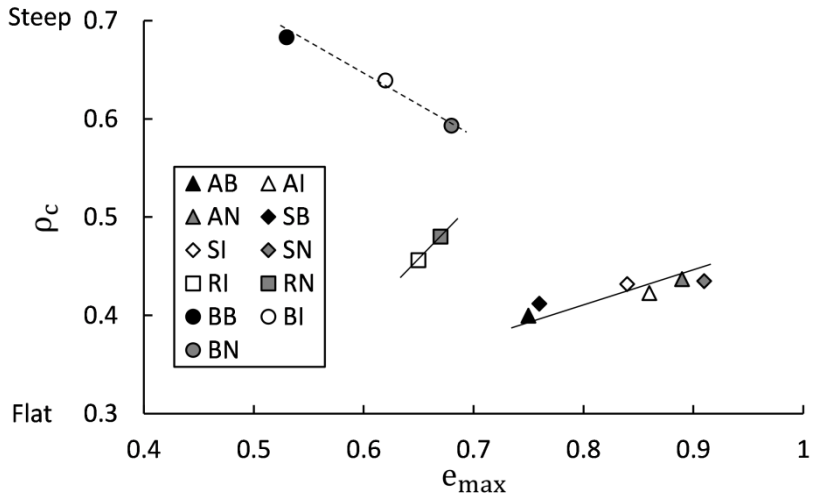


Fig. 5.5 Relationship between ρ_c and $e_{max.}$

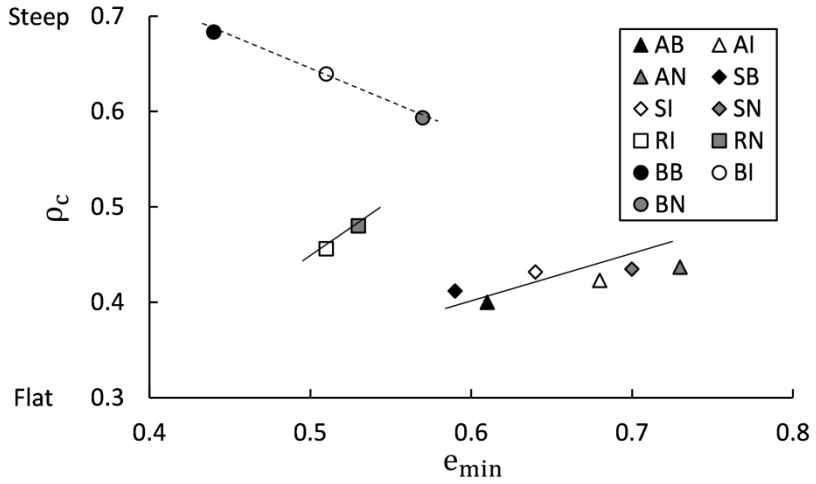


Fig. 5.6 Relationship between ρ_c and $e_{min.}$

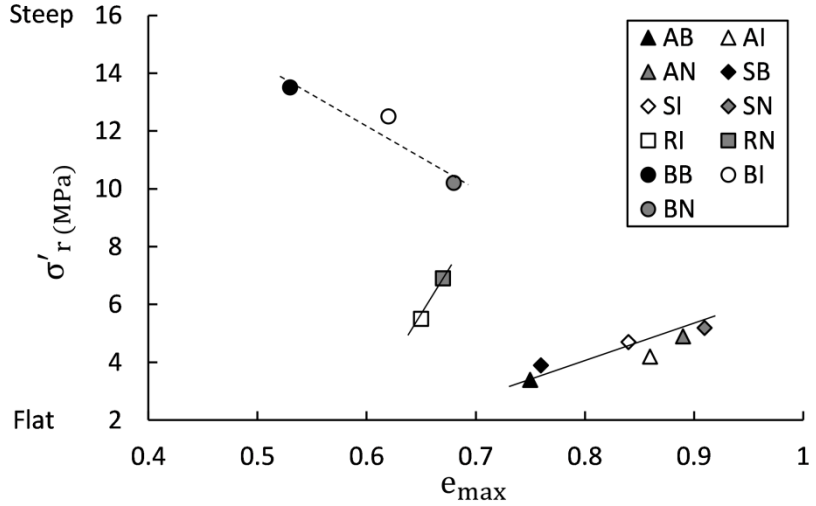


Fig. 5.7 Relationship between σ'_r and $e_{max.}$

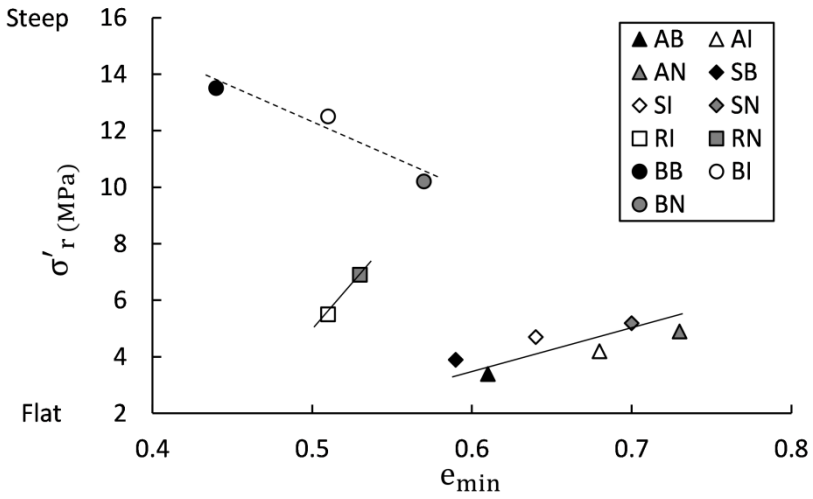


Fig. 5.8 Relationship between σ'_r and $e_{min.}$

6 CONCLUSION AND RECOMMENDATIONS

6.1 Conclusion

With the aim of better understanding of how PSD and particle shape affect the LCC, a series of high pressure 1-DCC tests was conducted on eleven non-plastic soil types. Three different PSDs, with C_u equal to 1.4, 2.0 and 2.8 were considered. In order to eliminate the effect of variation in D_{50}, the three PSDs had a common D_{50} of 0.6 mm (Fig. 3.8). Four different particle shapes were considered, ranging from angular to spherical beads (Fig. 3.9). The predominant mineralogy of all the tested soils was quartz (Table 3.2). Specimens of different initial formation densities (presented by void ratio) were tested for each of the eleven soil types. The range of vertical effective stresses considered was from 10 MPa to 190 MPa.

The following conclusions can be drawn:

1. When the LCC is modelled in a doubly logarithmic compression plane, there is a strong linear positive correlation between its slope (ρ_c) and the reference vertical effective stress at a unit void ratio (σ'_r) (Fig. 4.23, Equation 4.2).
2. Given the direct correlation between ρ_c and σ'_r identified herein (Fig. 4.23, Equation 4.2), there is a direct correlation between ρ_c and the coefficient of compressibility a_v at the LCC state (Section 4.3.1, Fig. 4.24).
3. At the LCC, the compressibility of natural sands is positively correlated to the initial uniformity of the PSD, whereas for spherical glass beads the

compressibility was negatively correlated to the initial uniformity of the PSD (Fig. 5.1).

4. Compressibility of non-plastic soils increases with particle roundness at the LCC state (Fig. 5.3).
5. There is a weak positive correlation between the LCC parameters (ρ_c and σ'_r) and the limit void ratios (e_{max} and e_{min}) of natural sands (Fig. 5.5 - Fig. 5.8).

6.2 Recommendations for Future studies

Based on the limitations of the foregoing study and to build on, or validate its findings, the following are the recommendations for future studies on non-plastic soils to better understand their LCC.

1. Because only quarzitic sands are investigated herein, future studies should test sands of different mineralogy such as carbonate and gypsum sands.
2. Because only one D_{50} is considered, future investigations should test PSDs of different D_{50}s to check whether the correlation between ρ_c and σ'_r identified herein depends on D_{50}.
3. Because only poorly graded soil types are tested (Cu < 6, Unified soil classification system), future investigations should test more broadly graded sands.
4. Future studies should investigate the reason for the atypical behaviour of the beads soil type observed herein, since it is commonly used to model natural sands for research purposes.

5. Future study should also consider the use of elastic finite element analysis to estimate the lateral strains of soil samples during compression from the radial strains measured at the outside edge of the compression mould.

7 REFERENCES

ALTUHAFI, F., O'SULLIVAN, C. & CAVARRETTA, I. 2012. Analysis of an image-based method to quantify the size and shape of sand particles. *Journal of Geotechnical and Geoenvironmental Engineering,* 139**,** 1290-1307.

ALTUHAFI, F. N. & COOP, M. R. 2011. Changes to particle characteristics associated with the compression of sands. *Géotechnique,* 61**,** 459-471.

ASTM D854-04 *Standard test methods for specific gravity of soil solids by water pycnometer.* ASTM International, West Conshohocken, PA.

ASTM D2435-04. *Standard test method for one-dimensional consolidation properties of soils using incremental loading.* ASTM International, West Conshohocken, PA.

ASTM D4186–06. *Standard test method for one-dimensional consolidation properties of saturated cohesive soils using controlled-strain loading.* ASTM International, West Conshohocken, PA.

ASTM D4254-00. *Standard test methods for mimimum index density and unit weight of soils and calculation of relative density.* ASTM International, West Conshohocken, PA.

BARRETT, P. J. 1980. The shape of rock particles, a critical review. *Sedimentology,* 27**,** 291-303.

BIAREZ, J. & HICHER, P.-Y. 1994. *Elementary mechanics of soil behaviour: saturated remoulded soils*, AA Balkema.

CAVARRETTA, I., COOP, M. & O'SULLIVAN, C. 2010. The influence of particle characteristics on the behaviour of coarse grained soils.

CHO, G.-C., DODDS, J. & SANTAMARINA, J. C. 2006. Particle Shape Effects on Packing Density, Stiffness, and Strength: Natural and Crushed Sands. *Journal of geotechnical and geoenvironmental engineering,* 132**,** 591-602.

CLAYTON, C. R. I., ABBIREDDY, C. O. R. & SCHIEBEL, R. 2009. A method of estimating the form of coarse particulates. *Geotechnique,* 59**,** 493-501.

COOP, M. R. & LEE, I. K. 1993. *The behaviour of granular soils at elevated stresses*, Thomas Telford London, UK.

COOP, M. R., SORENSEN, K. K., BODAS FREITAS, T. & GEORGOUTSOS, G. 2004. Particle breakage during shearing of a carbonate sand. *Géotechnique,* 54**,** 157-163.

CUBRINOVSKI, M. & ISHIHARA, K. 2002. Maximum and minimum void ratio characteristics of sands. *Soils and foundations,* 42**,** 65-78.

DONALD, W. T. 1948. Fundamentals of soil mechanics. Wiley, New York/Chapman & Hall, London.

HAGERTY, M. M., HITE, D. R., ULLRICH, C. R. & HAGERTY, D. J. 1993. One-dimensional high-pressure compression of granular media. *Journal of Geotechnical Engineering,* 119**,** 1-18.

HARDIN, B. O. 1985. Crushing of soil particles. *Journal of Geotechnical Engineering,* 111**,** 1177-1192.

HENDRON, J., ALFRED J. 1963. *The Behavior of Sand in One-Dimensional Compression.* PhD, University of Illinois.

KRUMBEIN, W. C. & SLOSS, L. L. 1963. *Stratigraphy and sedimentation,* San Francisco, Freeman and Company.

LADE, P. V., YAMAMURO, J. A. & BOPP, P. A. 1996. Significance of particle crushing in granular materials. *Journal of Geotechnical Engineering,* 122**,** 309-316.

LAMBE, T. W. & WHITMAN, R. V. 1969. Soil mechanics. Massachusetts institute of technology. John Wiley and Sons, New York.

LEUNG, C. F., LEE, F. H. & YET, N. S. 1997. The role of particle breakage in pile creep in sand. *Canadian Geotechnical Journal,* 33**,** 888-898.

LIESKER, K. R. The relationship between the grading of a silica sand and the applied stress. 8th South Africa Young Getechnical Engineers Conference, 2014 Stellenbosch, Western Cape, South Africa. 85-95.

MACROBERT, C. J. & TORRES-CRUZ, L. A. Evaluation of methods to determine reference void ratios. First Southern African Geotechnical Conference, 2016 Sun City, South Africa. Taylor & Francis Group, London, 255-260.

MCDOWELL, G. R. 2002. On the yielding and plastic compression of sand. *Soils and foundations,* 42**,** 139-145.

MCDOWELL, G. R. 2005. A physical justification for log e–log σ based on fractal crushing and particle kinematics. *Géotechnique,* 55**,** 697-698.

MESRI, G. & VARDHANABHUTI, B. 2009. Compression of granular materials. *Canadian Geotechnical Journal,* 46**,** 369-392.

MINH, N. H. & CHENG, Y. P. 2013. A DEM investigation of the effect of particle-size distribution on one-dimensional compression. *Géotechnique,* 63**,** 44.

MOHAMMADZADEH, D., BAZAZ, J. B. & ALAVI, A. H. 2014. An evolutionary computational approach for formulation of compression index of fine-grained soils. *Engineering Applications of Artificial Intelligence,* 33**,** 58-68.

NAKATA, Y., KATO, Y., HYODO, M., HYDE, A. F. & MURATA, H. 2001. One-dimensional compression behaviour of uniformly graded sand related to single particle crushing strength. *Soils and Foundations,* 41**,** 39-51.

PESTANA, J. M. & WHITTLE, A. J. 1995. Compression model for cohesionless soils. *Géotechnique,* 45**,** 611-632.

ROBERTS, J. E. 1964. *Sand compression as a factor in oil field subsidence.* PhD thesis, Massachusetts Institute of Technology.

ROBERTS, J. E. 1969. Sand compression as a factor in oil field subsidence. *Proc. Tokyo Symp. on Land Subsidence***,** 368-376.

ROBERTS, J. E. & DE SOUZA, J. M. 1958. *The compressibility of sands*, Massachusetts Institute of Technology.

SALAZAR, S. E. 2013. *One-dimensional compressibility of intermediate non-plastic soil mixtures.* Honors Thesis, The University of Arkansas.

SCHOFIELD, A. & WROTH, P. 1968. *Critical state soil mechanics*, McGraw-Hill London.

SHIPTON, B. & COOP, M. R. 2012. On the compression behaviour of reconstituted soils. *Soils and Foundations,* 52**,** 668-681.

SINGH, A. & NOOR, S. 2012. Soil compression index prediction model for fine grained soils. *Int. J. Innov. Eng. Technol.(IJIET),* 1**,** 34-37.

SUKUMARAN, B. & ASHMAWY, A. K. 2001. Quantitative characterisation of the geometry of discret particles. *Geotechnique,* 51**,** 619-627.

TERZAGHI, K. & PECK, R. B. 1948. Soil Mechanics in Engineering Practice. New York, N.Y.: John Wiley & Sons, INC.

TIWARI, B. & AJMERA, B. 2012. New correlation equations for compression index of remolded clays. *Journal of Geotechnical and Geoenvironmental Engineering,* 138**,** 757-762.

UYGAR, E. & DOVEN, A. G. 2006. Monotonic and cyclic oedometer tests on sand at high stress levels. *Granular Matter,* 8**,** 19-26.

VESIC, A. S. & CLOUGH, G. W. 1968. Behavior of granular materials under high stresses. *Journal of Soil Mechanics & Foundations Div*.

YAMAMURO, J. A., BOPP, P. A. & LADE, P. V. 1996. One-dimensional compression of sands at high pressures. *Journal of geotechnical engineering,* 122**,** 147-154.

8 APPENDICES

8.1 Appendix A 1-D Compression Curves

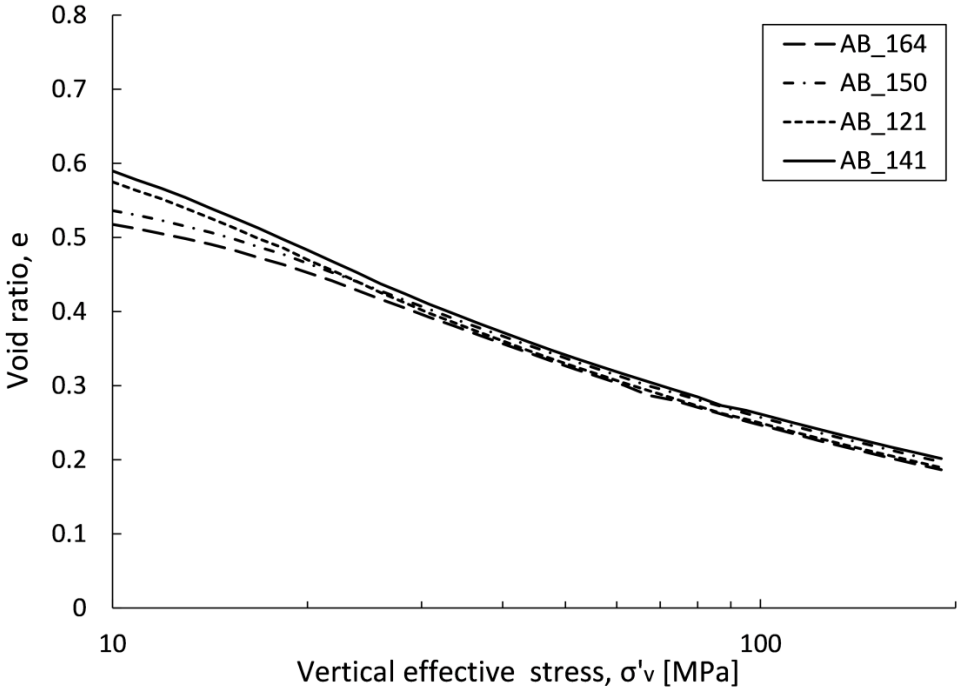


Fig. A.1 Angular broad soil type 1-D compression curves.

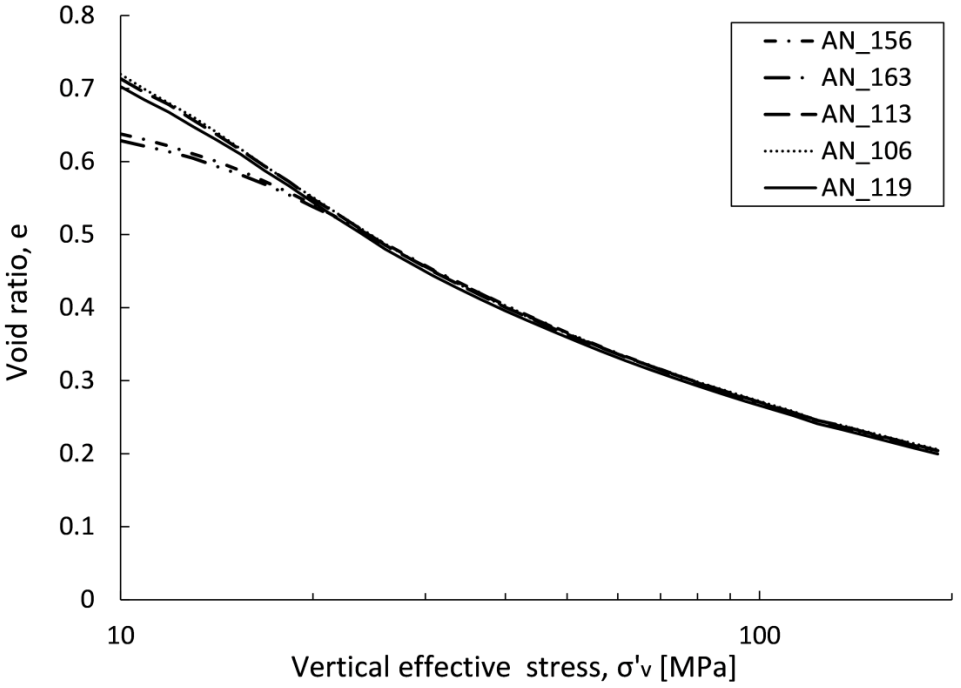


Fig. A.2 Angular narrow soil type 1-D compression curves.

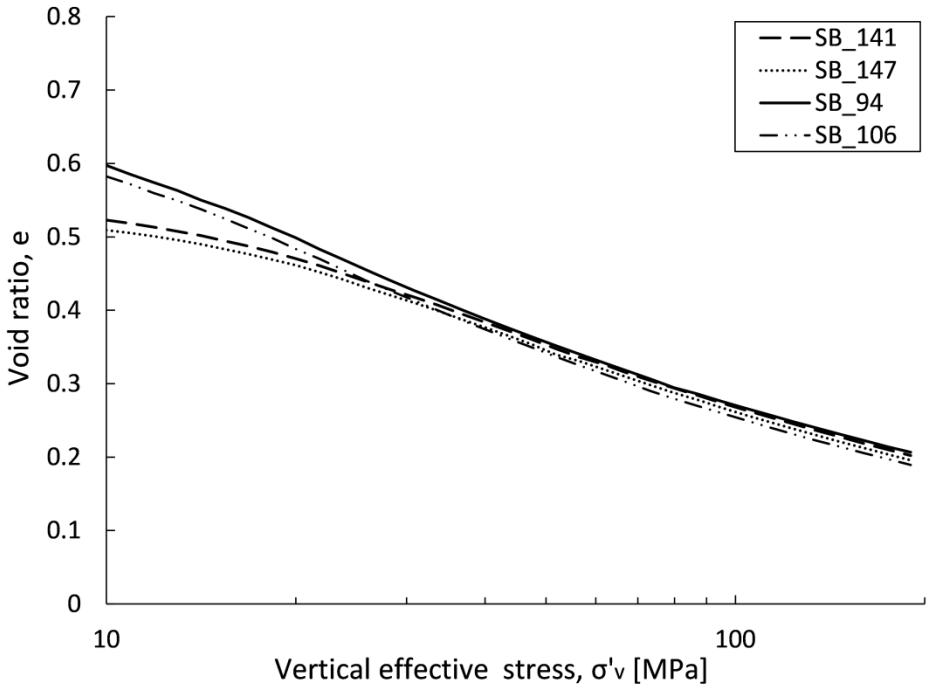


Fig. A.3 Sub-angular broad soil type 1-D compression curves.

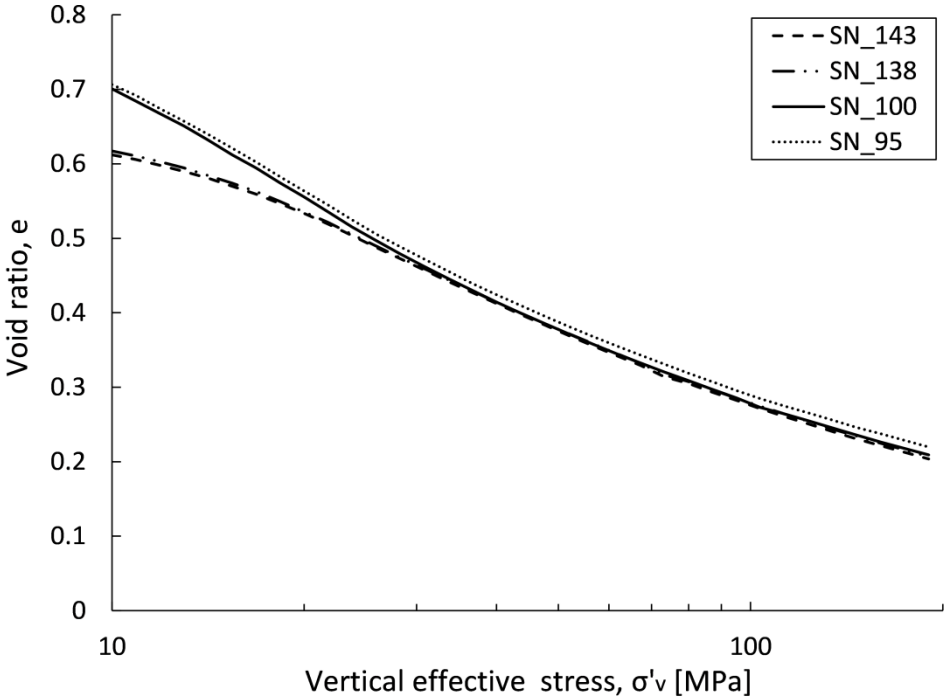


Fig. A.4 Sub-angular narrow soil type 1-D compression curves.

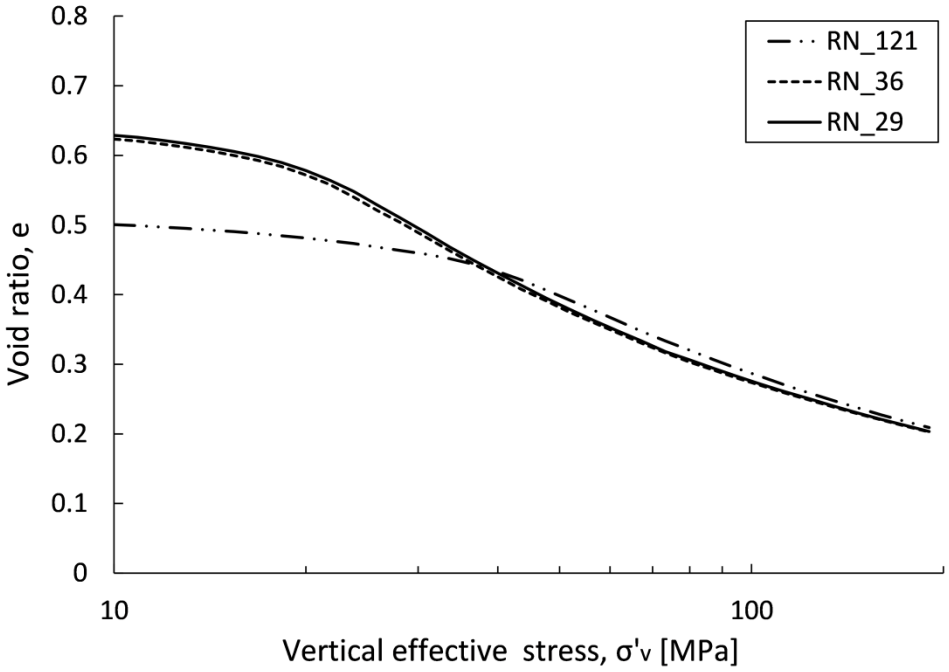


Fig. A.5 Rounded narrow soil type 1-D compression curves.

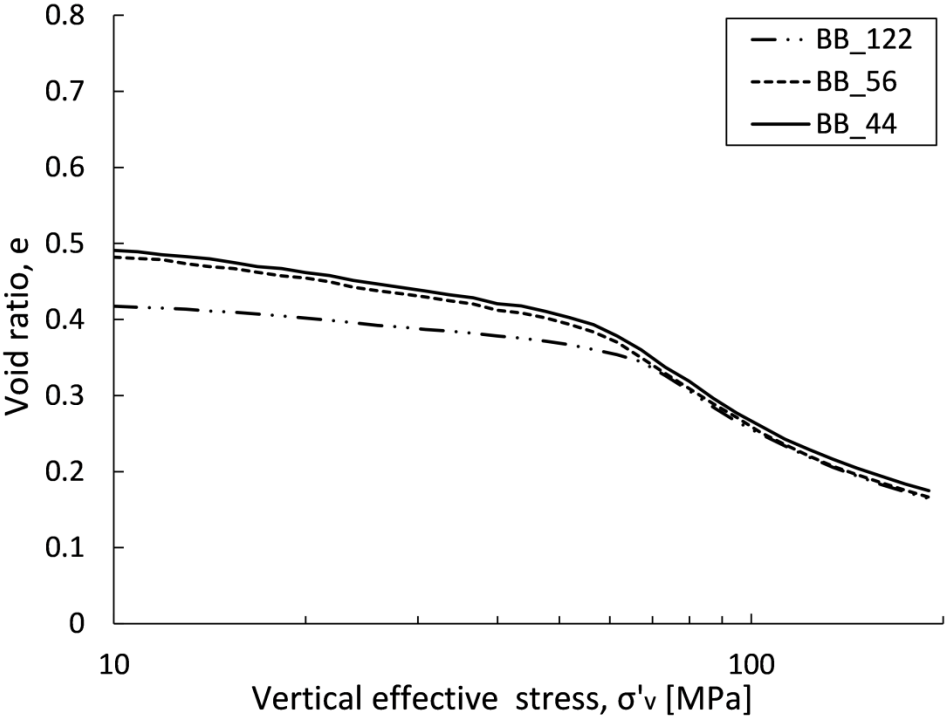


Fig. A.6 Beads broad soil type 1-D compression curves.

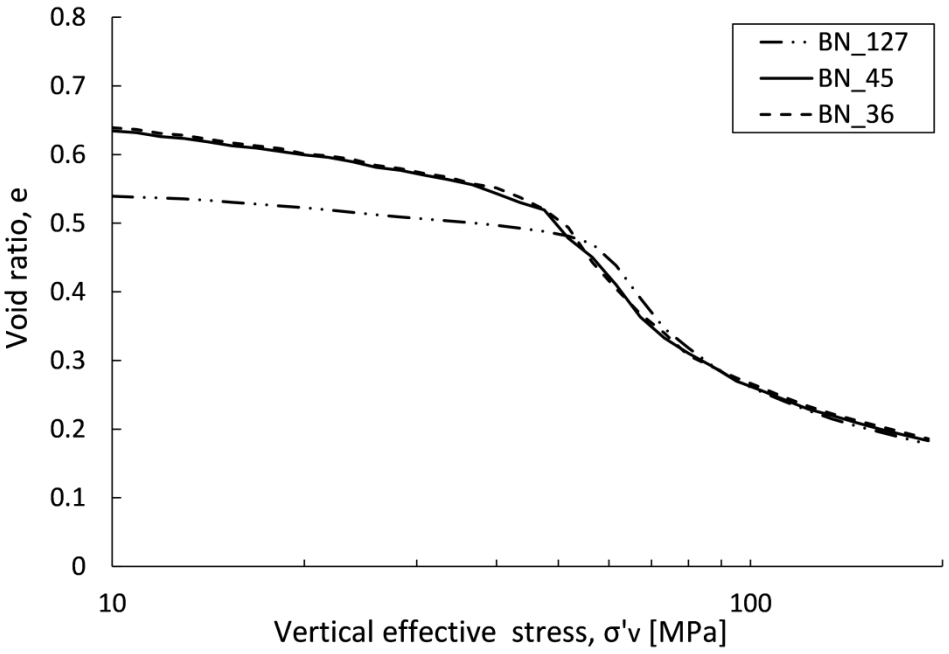


Fig. A.7 Beads narrow soil type 1-D compression curves.

8.2 Appendix B LCC Determination Plots

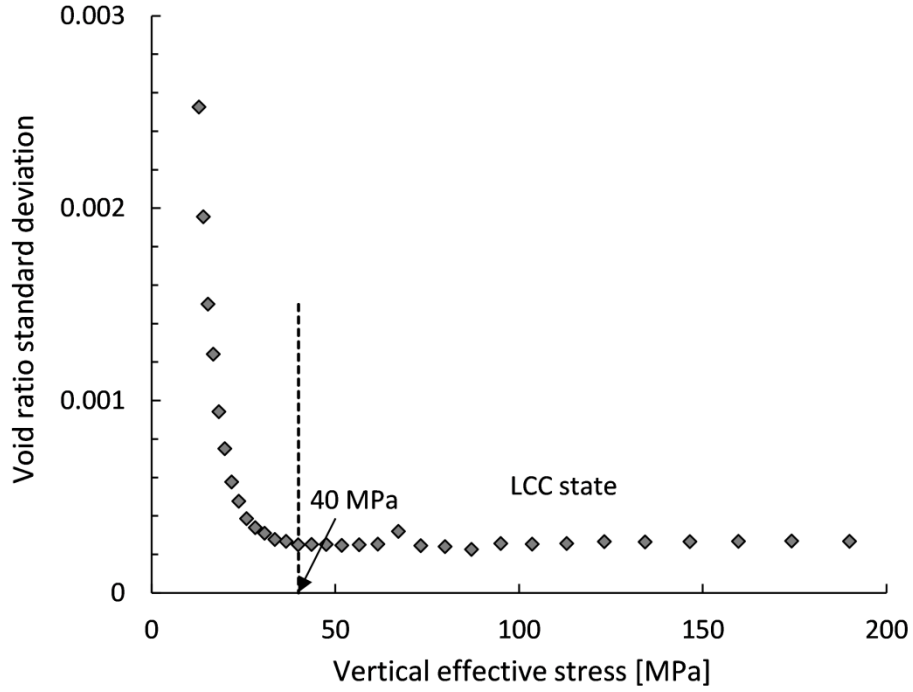


Fig. B.1 LCC determination for the AB soil type.

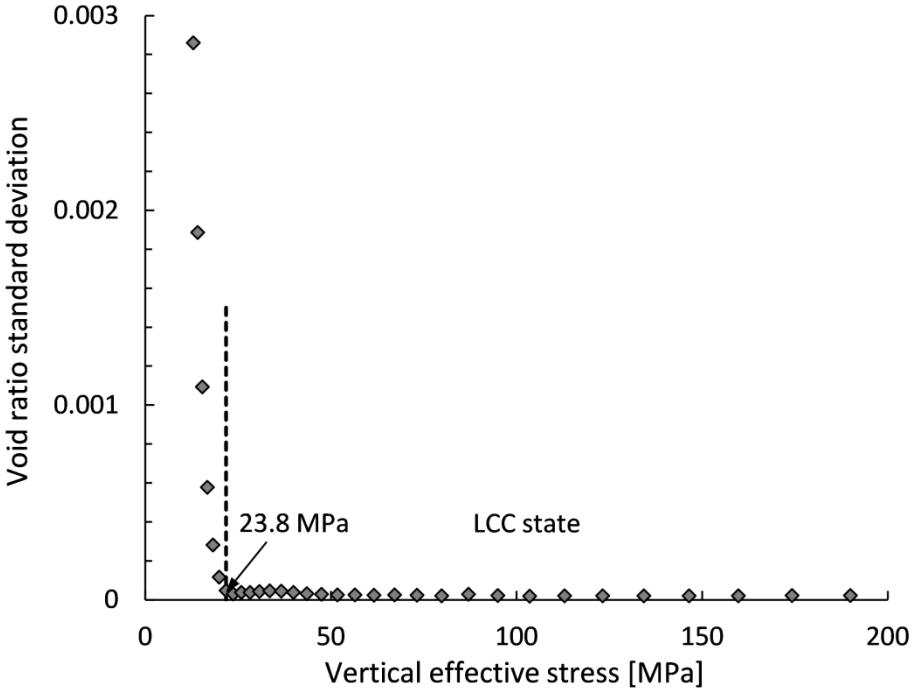


Fig. B.2 LCC determination for the AN soil type.

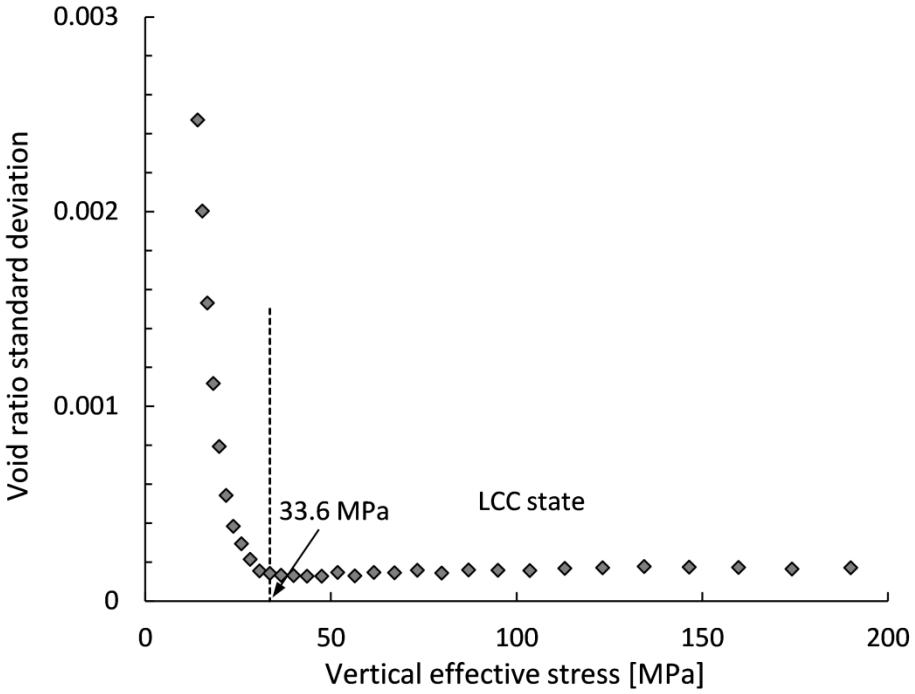


Fig. B.3 LCC determination for the SB soil type.

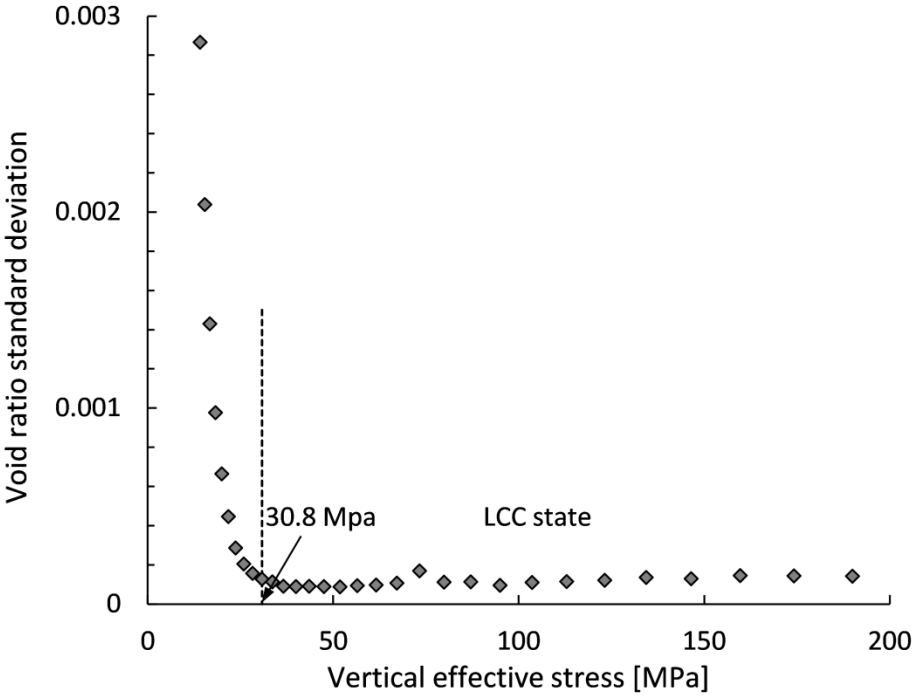


Fig. B.4 LCC determination for the SN soil type.

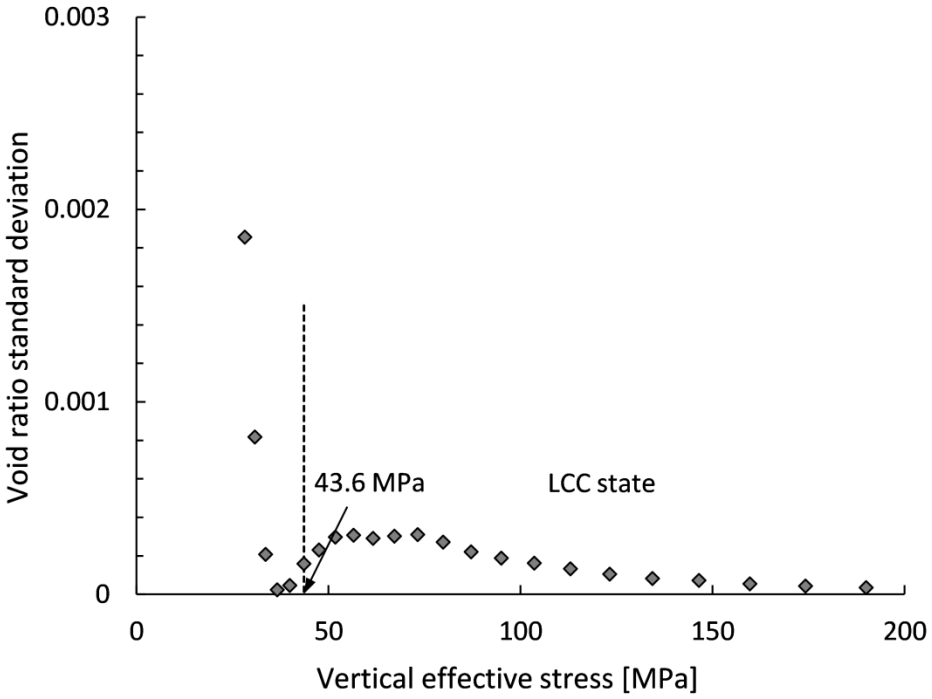


Fig. B.5 LCC determination for the RN soil type.

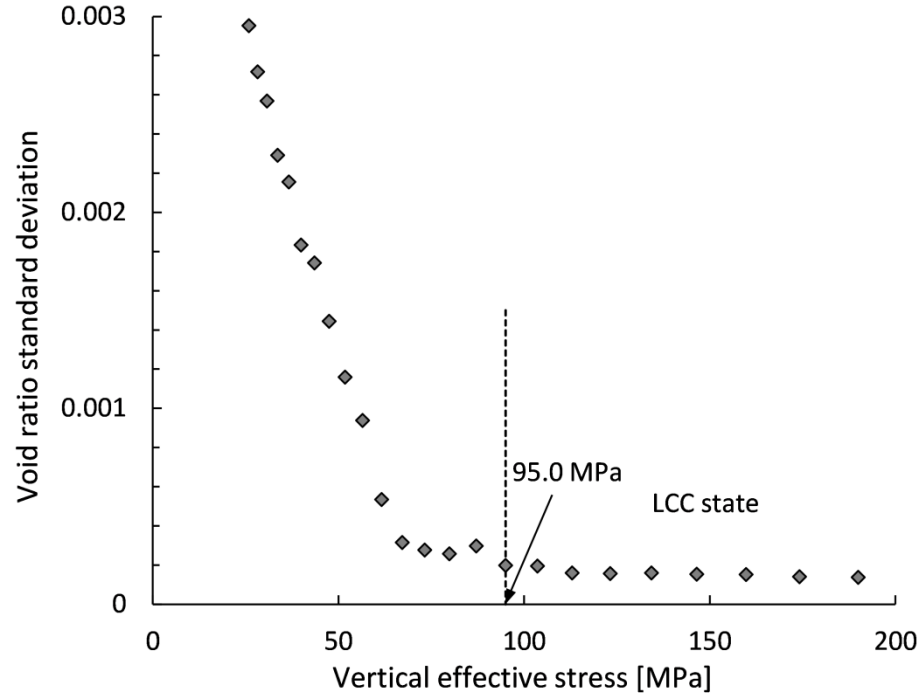


Fig. B.6 LCC determination for the BB soil type.

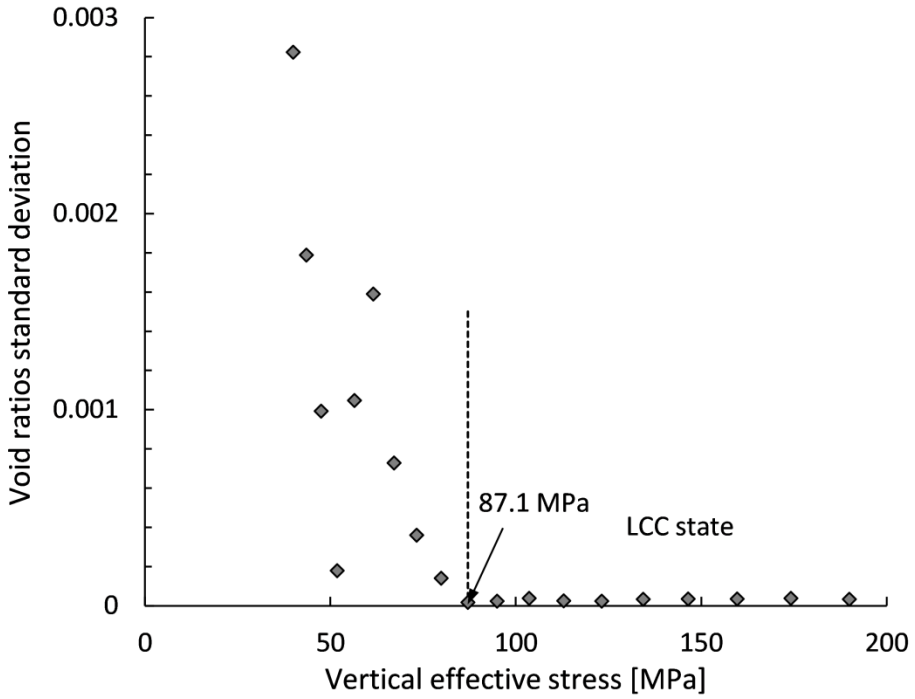


Fig. B.7 LCC determination for the BN soil type.

8.3 Appendix C Post-compression Sieve Analysis Results

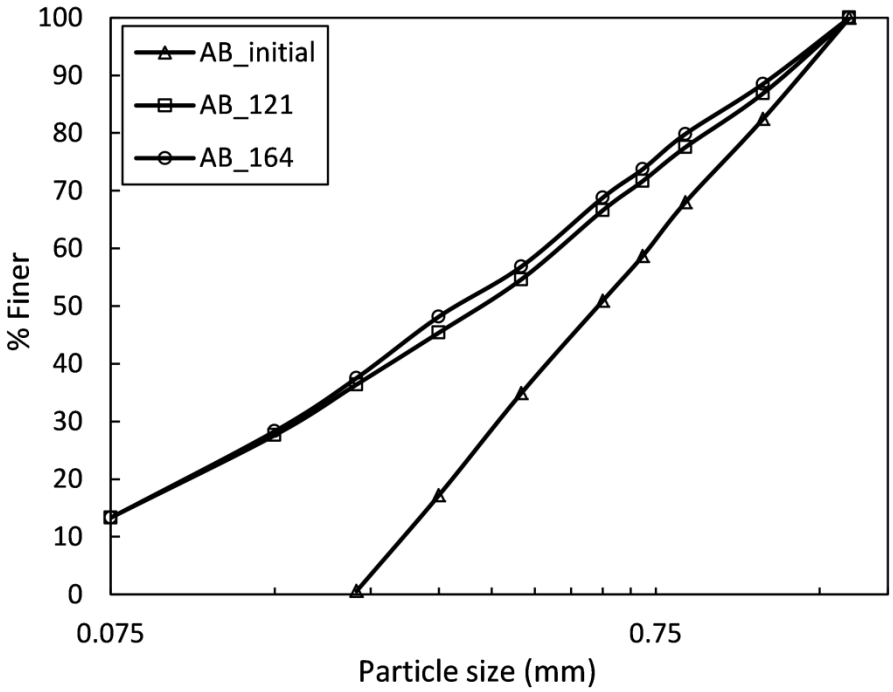


Fig. C.1 Pre and post-compression PSD curves of the AB soil type.

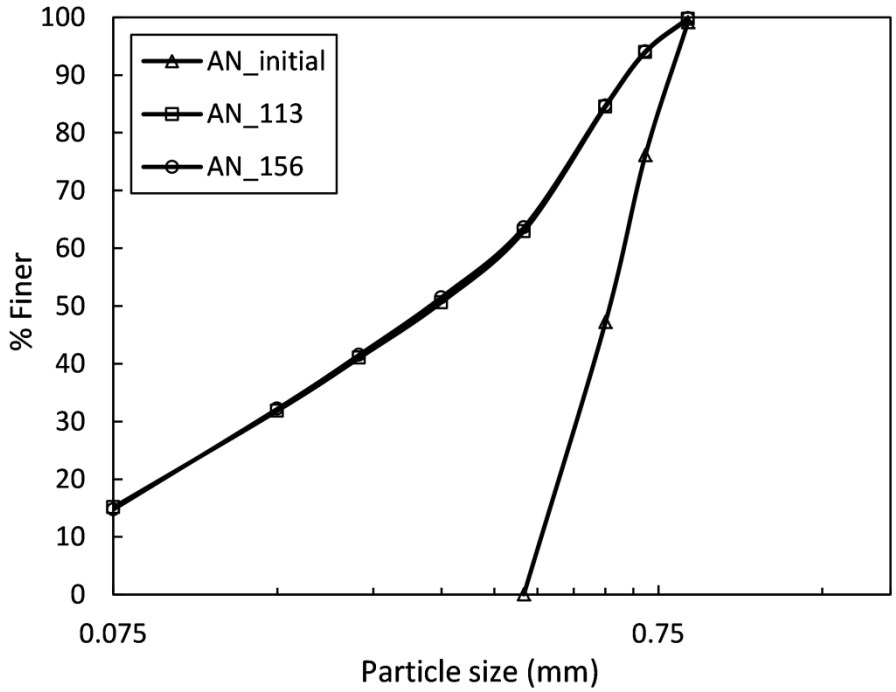


Fig. C.2 Pre and post-compression PSD curves of the AN soil type.

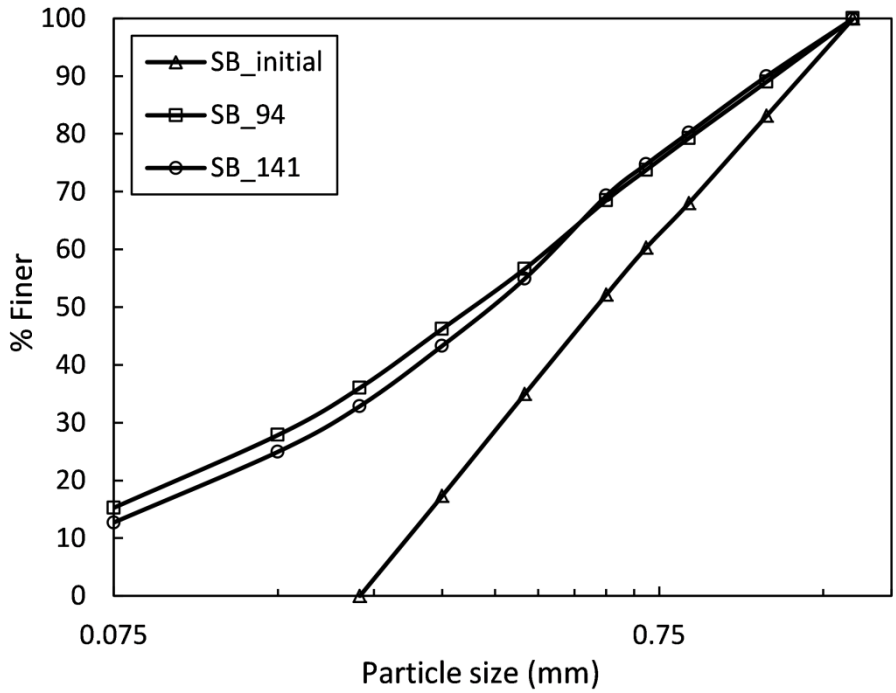


Fig. C.3 Pre and post-compression PSD curves of the SB soil type.

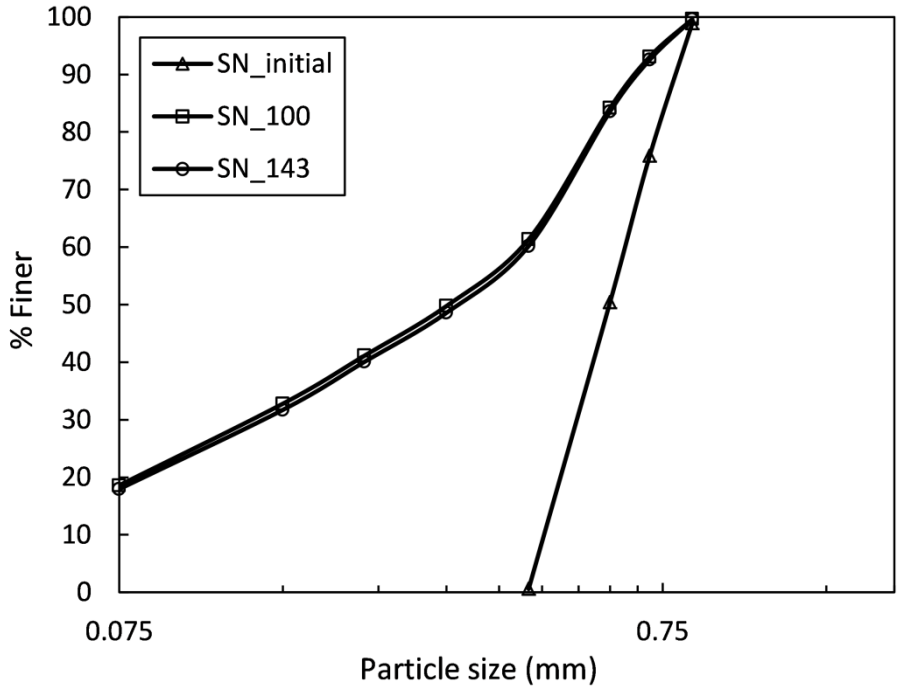


Fig. C.4 Pre and post-compression PSD curves of the SN soil type.

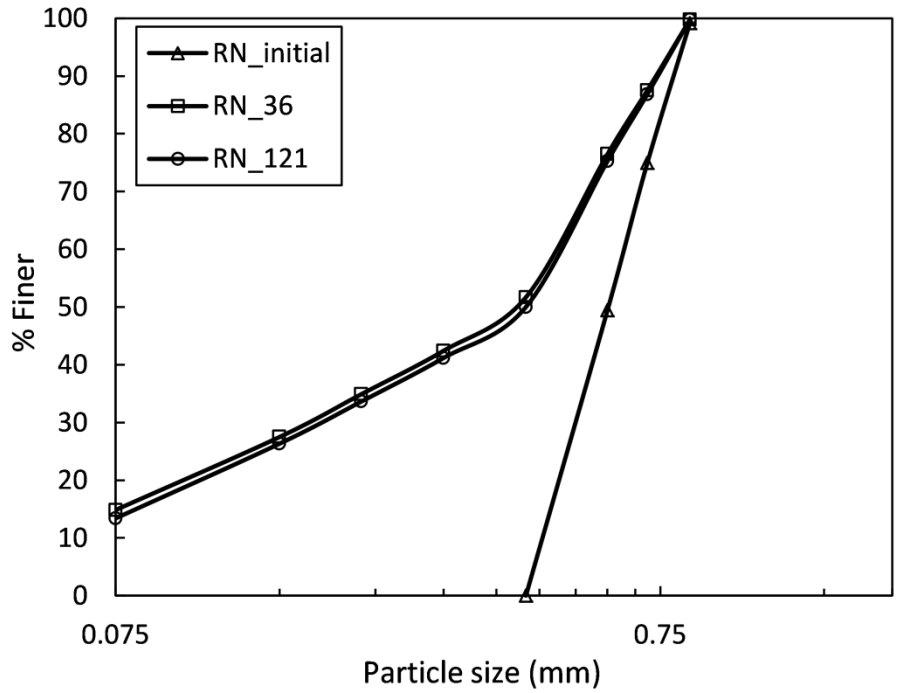


Fig. C.5 Pre and post-compression PSD curves of the RN soil type.

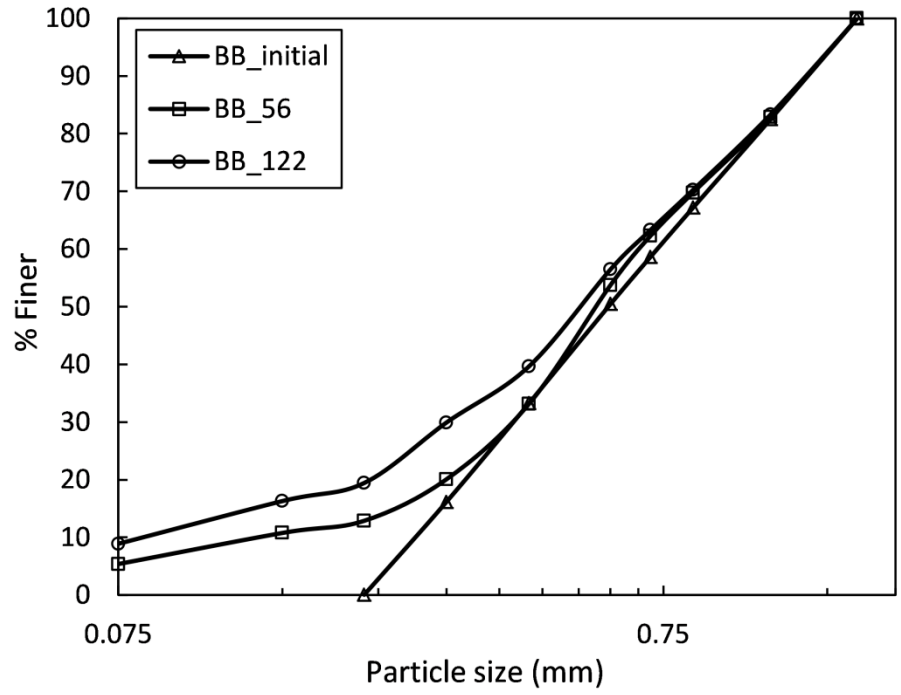


Fig. C.6 Pre and post-compression PSD curves of the BB soil type.

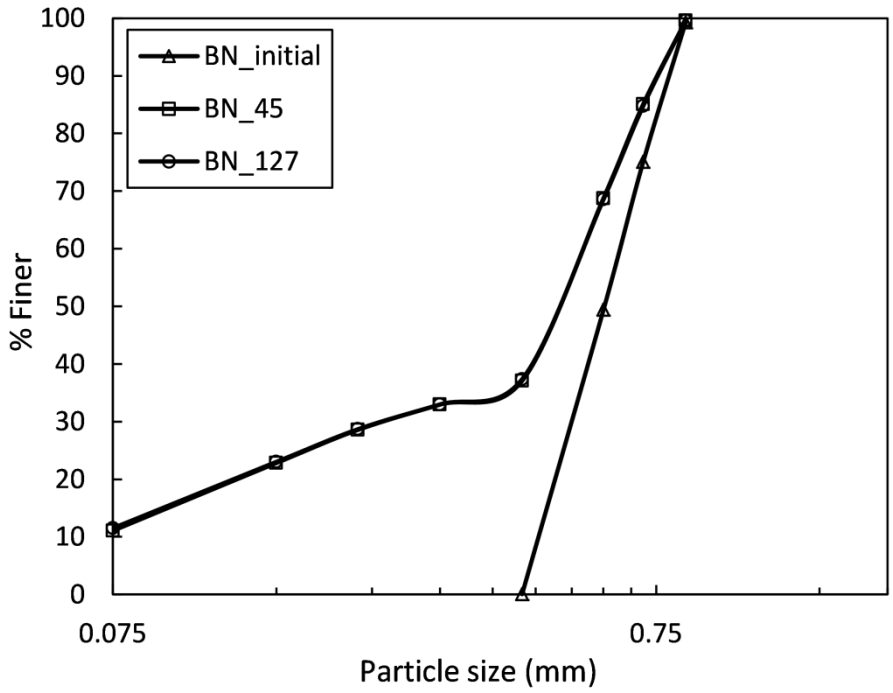


Fig. C.7 Pre and post-compression PSD curves of the BN soil type.